The molecular mechanism of multi-ion conduction in K^+ channels

Vom Fachbereich Physik
der Universität Duisburg-Essen
zur Erlangung des akademischen Grades eines
Doktors der Naturwissenschaften
genehmigte Dissertation

von

Jean-Fang Gwan

aus

Taipeh, Taiwan

Referent: Priv.-Doz. Dr. Artur Baumgärtner
Korreferent: Prof. Dr. Peter Entel
Tag der mündlichen Prüfung: 19 Januar 2007

Abstract

Steered molecular dynamics (SMD) simulation method is applied to a fully solvated membrane-channel model for studying the ion permeation process in potassium channels. The channel model is based on the crystallographic structure of a prokaryotic K^+ channel– the *KcsA* channel, which is a representative of most known eukaryotic K^+ channels. It has long been proposed that the ion transportation in a conventional K^+-channel follows a multi-ion fashion: permeating ions line in a queue in the channel pore and move in a single file through the channel. The conventional view of multi-ion transportation is that the electrostatic repulsion between ions helps to overcome the attraction between ions and the channel pore. In this study, we proposed two SMD simulation schemes, referred to '*the single-ion SMD*' simulations and '*the multi-ion SMD*' simulations. Concerted movements of a K-W-K sequence in the selectivity filter were observed in the single-ion SMD simulations. The analysis of the concerted movement reveals the molecular mechanism of the multi-ion transportation. It shows that, rather than the long range electrostatic interaction, the short range polar interaction is a more dominant factor in the multi-ion transportation. The polar groups which play a role in the concerted transportation are the water molecules and the backbone carbonyl groups of the selectivity filter. The polar interaction is sensitive to the relative orientation of the polar groups. By changing the orientation of a polar group, the interaction may switch from attractive to repulsive or vice versa. By this means, the energy barrier between binding sites in the selectivity filter can be switched on and off, and therefore the K^+ may be able to move to the neighboring binding site without an external driving force. The concerted transportation in the selectivity filter requires a delicate cooperation between K^+, waters, and the backbone carbonyl groups. To accomplish a concerted transportation, the occupancy state of the selectivity filter must be an alternative sequence of K^+ and water molecules, i.e., a K-W-K-W or a W-K-W-K sequence.

Contents

1. Introduction

A cell membrane is constituted by a continuous sheet of lipid bilayer. A lipid bilayer is composed of various phospholipids, with the hydrophobic fatty acid chains buried inside, and the polar head groups facing outside. The hydrophobic interior of the lipid bilayer is highly impermeable to charged substances, including various ions like Na^+, K^+, Ca^{2+}, and Cl^-. The transportation of ions through cell membrane relies on membrane proteins called ion channels. An ion channel is composed of an integral protein surrounding an aqueous pore. By this means a hydrophilic environment is created in the membrane, so that ions are able to move through it. The influx and efflux of ions regulate the exciting state of a cell, which is essential in the formation and propagation of neuronal signals and many other physiological processes.

Most ion channels allow only particular types of ions to move through them. This property is known as the selectivity of ion channels. For instance, K^+ channels, the main subject of this study, are ion channels selectively permeable to K^+. K^+ channels are known for their high K^+ permeation rate. For a typical potassium channel, the throughput rate of K^+ is close to its diffusion limit in water, which implies that the energy barrier in a permeation process is only on the order of thermal fluctuation. Meanwhile, they are highly selective between K^+ and Na^+. In most K^+ channels, K^+ is 100$\sim$1000 times more permeable than Na^+, implying that the channel protein has a much higher affinity to K^+. The high throughput rate and strong affinity to K^+ seem to be contradict to each other. How they compromise with each other energetically is not understood yet. To answer this question, one has to examine the K^+ permeation process in a K^+ channel.

In the 1950s, A. Hodgkin and collaborators conducted a series of experiments on K^+ channels. In their measurements of K^+ flux across the squid giant axon membrane, they observed that the current-voltage ratio was higher than predicted by the theory of independent movement of ions [1, 2]. Instead, there seemed to be some kind of coupling of the K^+ movements. To explain their experimental results, they suggested that the ions must move through the channel pore in a multi-ion fashion: permeating ions line up in a single file in the channel pore; when an ion enters the channel from one end, it induces a concerted movement of the lining ions, and knocks out the ion at another end. This is known as the multi-ion mechanism [2], and has been observed a common picture of K^+ transportation in K^+ channels. We believe that the multi-ion mechanism may account for the high permeation rate of K^+ channels. This theory has been proposed for decades, but its molecular mechanism remains unclear. To understand the molecular mechanism of the multi-ion permeation, we need a K^+ channel model with all atomic

details.

However, ion channels are membrane proteins, which are known particularly difficult to handle and crystallize because of their amphipathic nature. In 1998, a breakthrough was achieved by the experimental group of R. MacKinnon. They successfully crystallized the KcsA channel– a small prokaryotic K^+ channel– and resolved its atomic structure by X-ray diffraction analysis [3, 4]. The KcsA channel is an ideal model for K^+ channel studies. The sequence homology analysis shows that the KcsA structure is highly similar to the core part of most known eukaryotic potassium channels; moreover, various single-ion measurements show that it contains all conduction properties of conventional K^+ channels. The crystallographic data shows that the channel pore has a wide water cavity in the middle, and a narrow extracellular entryway called the selectivity filter, with several K^+ captured in it. The selectivity filter, as told by its name, is the structural area responsible for the ion selection. The structure of KcsA provides great insight about ion transportation mechanism in K^+ channels. Because of this remarkable contribution, R. MacKinnon won the Nobel prize of chemistry five years later in 2003.

Based on the KcsA structure, we have built up an atomic model and performed several molecular dynamics simulations to study the ion permeation process in a K^+ channel. Molecular dynamics have long been applied to studies of biomolecules [5, 38, 7]. Experimental measurements usually provide a more static picture of a macromolecule, while the dynamics of the molecule in many systems are of the same importance for understanding its biological function. Computer simulations offer a possibility to bridge this gap. It can provide a more dynamical picture and details of the motion of a biomolecule. The fast development of computing capability makes it possible nowadays to simulate a larger system of higher complexity in a longer time scale. Currently the simulation of a model up to 10^5 atoms including macromolecule, lipid membrane, and explicit solvent in the length of 10 nanoseconds on parallel machines takes only weeks [7, 8].

Molecular dynamics simulation methods have been applied to the studies of various channel systems, e.g. the gramicidin channel [9, 10, 11], the giant OmpF porin [12, 13], and the KcsA channel [14, 15, 16]. However, the throughput rate of a KcsA channel is about 10^8 ions per second, that means, it takes about tens nanoseconds for one potassium ion to permeate the channel, which makes it a rare event during the simulation. To increase the probability of the occurrence of a permeation event in a simulation, we applied a manipulated MD simulation method — the steered molecular dynamics simulation method — to study the ion permeation process in the KcsA channel. We proposed two simulation schemes, referred to the single-ion and the multi-ion steered MD simulations. The simulation results reveal the molecular mechanism of a multi-ion conduction, and provide important implications to the answer of the high K^+ permeation rate.

2. Experimental facts of the KcsA channels

The KcsA channel is a small prokaryotic potassium channel from the Gram-positive soil bacterium *Streptomyces lividans*. It was first identified by Schremp *et al.* in 1995 [17]. The homology analysis of the KcsA protein sequence shows high structural similarity to the core part of most known eukaryotic K^+ channels; moreover, it contains all conduction properties of conventional K^+ channels. Its high oligomeric stability in various solvent, high expression levels in *Escherichia coli*, and ease of purification make it an ideal candidate for high-resolution structure studies [17, 18, 19]. In 1998, R. MacKinnon and collaborators have successfully crystallized KcsA and resolved the crystallographic structure by X-ray diffraction analysis [3]. It was the first K^+ channel to have its crystallographic structure resolved. Our knowledge about K^+ channel functions increased remarkably since then. This great achievement brought R. MacKinnon the Nobel prize of chemistry five years later in 2003.

Our studies about the ion permeation process in K^+ channels are mainly based on the model of the KcsA channel. In this chapter I am going to introduce the experimental facts about the KcsA channel, including its conduction properties, its molecular structure, and the experimental observation about the gating mechanism.

2.1. The conduction properties of KcsA

The KcsA channel has all typical conduction properties of eukaryotic K^+ channels [20, 21]. In laboratories, KcsA is purified and reconstituted into planar lipid bilayer for the measurement of its electrophysiologial properties. Studies of the activities of KcsA have been carried out at the single-channel level by using the patch clamp technique. It was found that the conductance of KcsA at physiological K^+ concentration is in the same range measured for other eukaryotic potassium channels like *Shaker*,[1]

[1]The first cloned K^+ channel– *Shaker*– is a mutant K^+ channel from Drosophila (fruit fly). The name *Shaker* comes from that flies with the *Shaker* mutation are hyperactive– they shake their legs under anesthesia.

K_{ir},[2] and BK [3] channels [21]. Measurements of the K^+ current in symmetrical ion concentration show that KcsA channels are slightly outward rectifiered for K^+: the chord conductance for 200 mV is 56 pS, whereas for -200 mV it is 31 pS [22, 21]. For other permeant ions, KcsA is slightly outward rectifiered as well [21].

K^+ channels are highly discriminating between K^+ and Na^+. The selectivity ratio of K^+ to Na^+ in eukaryotic K^+ channels ranges from 100 to 1000 [20, 23]. The ion selectivity sequence of the KcsA channel determined in symmetrical solution is $K^+ > Rb^+$, NH_4^+, $Tl^+ \gg Na^+$, Li^+, Cs^+ [24, 25, 21], same as all known K^+ channels [20]. Actually, the permeability of Na^+ is not detectable in a general physiological condition. Measurements of the K^+-dominated reversal potential under bi-ionic conditions (100 mM K^+ internal/20 mM K^+ and 100 mM Na^+ external) with techniques of higher precision determine that K^+ is at least 150-fold more permeant than Na^+ [21]. KcsA exhibits block by Na^+, Ba^{2+}, and Cs^+, which are common behaviors of eukaryotic K^+ channels.

Intracellular Na^+ block is a general property of K^+ channels [26, 27, 23]. For KcsA, the internal Na^+ is a strong voltage-dependent blocker at low voltage (below 200 mV) [22, 28]. It has been suggested that the blocking site of Na^+ is located at the inner entryway of the selectivity filter [28]. In contrast, the external Na^+ has no effect on the K^+ conductance. The Na^+ blocking asymmetry can be applied to the determination of the orientation of the KcsA channel in experiments [22].

Mutation in the K^+-channel signature sequence 'TVGYG' of KcsA dramatically alter its permeation behaviors: the channel turns nonselective between monovalent cations, that is, it turns a CNG-like channel (cyclic nucleotide-gated cation channel) [24, 25]. It implies that the amino sequence of the selectivity filter is critical for the ion selection in the KcsA channel.

2.2. The molecular architecture of KcsA

The KcsA channel protein is a tetramer composed of four identical monomers encoded by 160 amino acids. The protein sequence of KcsA is given in Fig. 2.1. Each monomer contains two transmembrane α-helices, denoted by TM1 and TM2, connected by a pore region, which contains a P-helix and the K^+ channel signature sequence 'TVGYG', which is highly conserved among K^+ channels. TM1 is connected to the N-terminal and TM2 to the C-terminal of the monomer. According to various investigations of the orientation of the channel when inserted in the lipid bilayer, both N- and C-terminus should be in the cytoplasmic side [22, 29]. The sequence alignment shows high homology to channels belonging to the voltage-gated ion channel (VIC) superfamily, which includes voltage-

[2] K_{ir} is the abbreviation of the 'inward rectifier K^+ channels'. They act as a valve, and allow only inward K^+ current.

[3] BK is the abbreviation of the 'big K^+ channels. They are Ca^{2+} dependent K^+ channels, and are known by their long and large unitary currents.

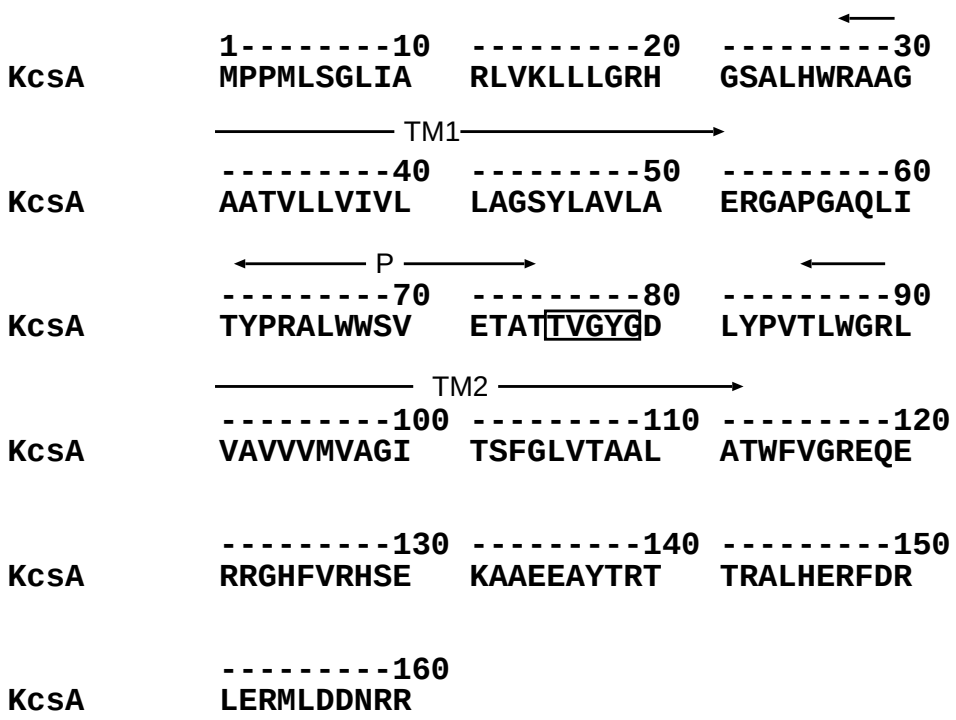

Figure 2.1.: The protein sequence of KcsA. The three α-helices TM1 (27–51), P (62–74), and TM2 (86–112) are marked out. The rectangular box involves the K^+-channel signature sequence 'TVGYG' (residue 75-79) of the selectivity filter.

gated K^+ channels, inward rectifier K^+ channels, Ca^{2+}-activated K^+ channels, and cyclic nucleotide-gated cation channels (CNG channels) [3].

The crystallographic structure of KcsA was resolved by the X-ray diffraction analysis at the resolution of 3.2 Å by Doyle *et al.* in 1998 (PDB file 1BL8) [3], and later an improved structure at the resolution of 2.0 Å in 2001 (PDB file 1K4C) [4]. Residues 126 to 160 on the carboxyl terminus of the channel were cleaved in the preparation process. From the remaining sequence, only the structure of the membrane part (residues 23 to 119) was determined by the X-ray analysis. The four monomers are assembled symmetrically surrounding a central pore through the membrane. They are arranged in the way that the transmembrane helices TM2 are inside facing the channel pore and TM1 are outside facing the membrane, as shown in Fig. 2.2. The four TM2 are bound like an inverted teepee and form a central cavity of 10 Å in diameter located in the middle of the membrane and a 18 Å long tunnel at the intracellular entryway. The p-loop connecting the two transmembrane helices is in the upper part of the channel close to the extracellular side. The P-helix is inserted to the membrane by about 45° to the membrane plane with its C-terminal pointing towards the center of the cavity. Both the central cavity and the P-helices play certain functional roles on ion conduction.

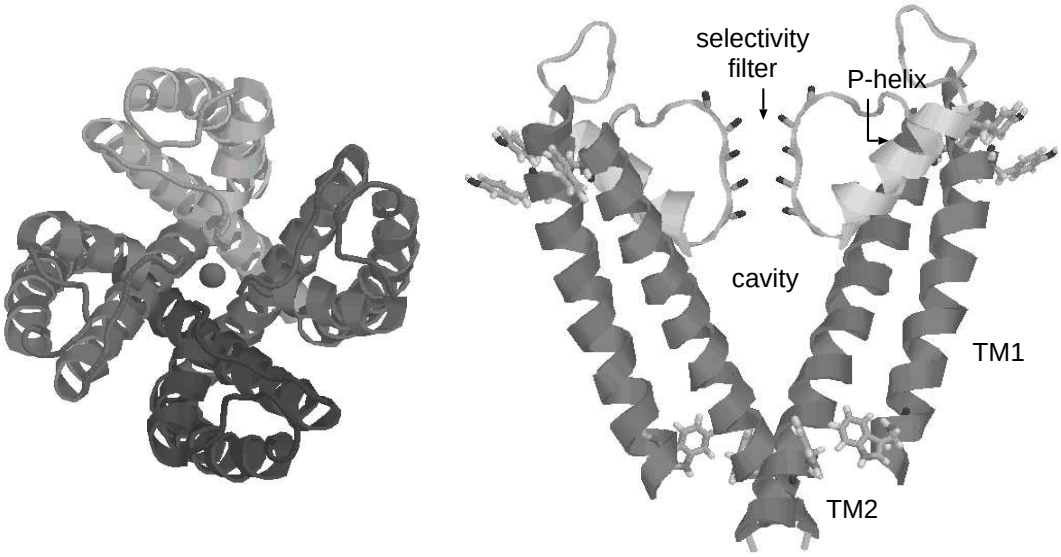

Figure 2.2.: The structure of the KcsA channel viewed from the top (left) and from the side (right). Only two opposite ones of the tetramer are shown in the side view. From the top view one can see that the channel is composed of four monomers surrounding a central pore. The pink ball is a K^+ located in the selectivity filter. And in the side view, the transmembrane helices TM1, TM2 and the P-helices are shown. The pore is lined by the p-loop at the upper part, and by TM2 at the lower part of the channel. The aromatic residues showed here lie on the membrane surface (Trp^{26} and Trp^{113} at the intracellular and Tyr^{45},Tyr^{66}, and Trp^{87} at the extracellular sides) when inserted in the membrane.

First, the size of the cavity is large enough to contain about 50 water molecules in it, and the P-helices pointing towards the cavity center impose a negative electrostatic field at the cavity center. These two features effectively reduce the dielectric barrier for an ion to move across the membrane [3, 30, 31]. The rest of the loop constructed the narrowest part of the channel pore– the selectivity filter. The selectivity filter is about 12 Å long, lined by the backbone of the K^+-channel signature sequence 'TVGYG'. It is the most important functional component of the channel; the high throughput rate and the high selectivity are mainly controlled by this area. Therefore, maintaining the stability of the selectivity filter structure is important to the function of the channel. The crystallographic structure reveals that the structure of the selectivity filter is sustained by a complicated hydrogen-bonded network in this area [3, 4, 14].

Some aromatic residues are found at both ends of the channel protein. When inserted in the membrane, those aromatic side chains lie on the membrane surface and bond with the surrounding lipid heads noncovalently [32]. The molecular architecture of the cytoplasmic domains of KcsA have been determined using site-directed spin-labeling methods (SDSL) and electron paramagnetic resonance (EPR) spectroscopy. It was found that the N-terminus of KcsA also serves to stabilize the channel protein in the membrane– it

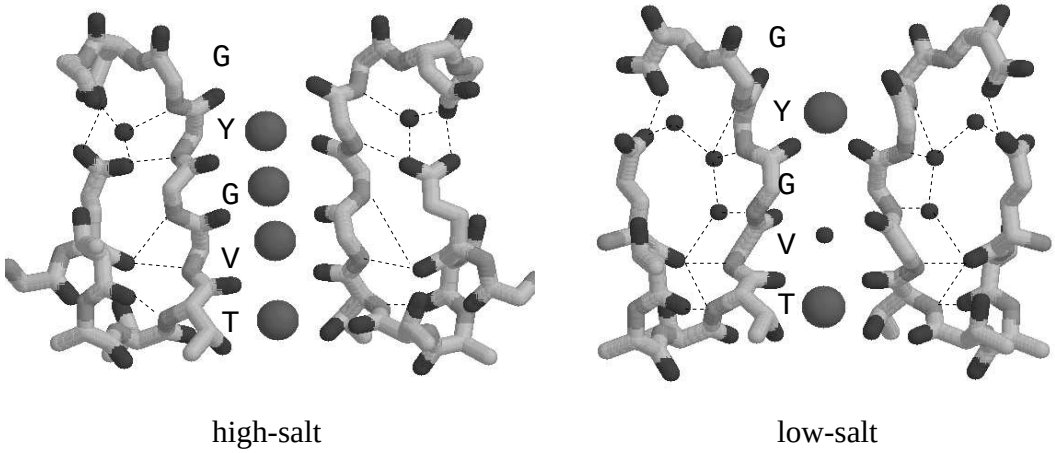

Figure 2.3.: The structure of the selectivity filter in high-salt (left) and low-salt (right) condition. The potassium ions are shown in magenta, and the red balls are water molecules. The probable hydrogen bondings are shown in black dashed lines.

forms an α-helix anchored at the membrane surface [33].

2.3. The selectivity filter

The selectivity filter is the key structural component responsible for the selective permeation of ions. The 12 Å long, narrow pore is composed of the backbone carbonyl groups of the K^+-channel signature sequence 'TVGYG'. The backbone carbonyl groups point towards the pore axis, and form four and a half binding sites. When a K^+ sits in one of the binding sites, it is stably coordinated by eight carbonyl oxygens. Indeed in the crystallographic structures, several K^+ have been resolved located at these binding sites. The filter structure is sustained by a delicate hydrogen-bonded network, as shown in Fig. 2.3(a).

The structure of the binding sites at the two entryways are different from other binding sites inside the selectivity filter. The binding site at the extracellular mouth is composed of the carbonyl groups from Tyr^{78} below and Gly^{79} above. Instead of pointing towards the pore axis, the carbonyl oxygens of Gly^{79} point upward into the extracellular solution and surround the entryway of the selectivity filter in a ring. In the crystallographic structure of KcsA channels, a water ring at the extracellular mouth has been observed [4]. The K^+ entering this binding site will be coordinated by the carbonyl oxygens of Tyr^{78} and the water ring; thus, the K^+ can be halfly hydrated. The binding site at the inner entryway is composed of the backbone carbonyl groups and the side chain hydroxyl groups from the same residue Thr^{75}. The hydroxyl groups of the side chains are polar

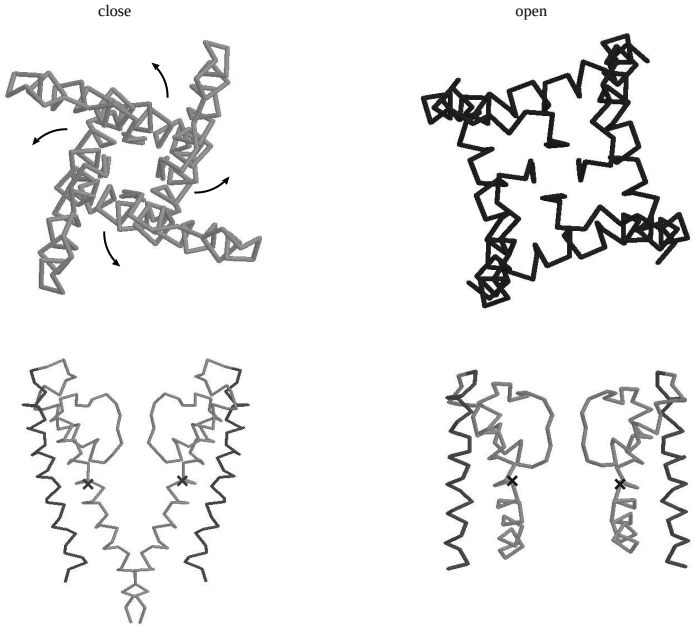

Figure 2.4.: Open and close conformations of K^+ channels viewed from top and side. In the top-viewed pictures, only the backbone of the selectivity filter and inner helices are shown, and in the side-viewed pictures, only two opposite monomers are shown. Arrows indicate the direction of the movement of the inner helices from close to opene. The red crosses mark the hinge points on the inner helices. The closed conformation is from the KcsA channel [3, 4] and the open one from the MthK channel [37].

groups; therefore, they are attractive to water molecules and can serve in the hydration and dehydration of a K^+ at the inner entryway of the selectivity filter.

It has been observed that the structure of the selectivity filter is coupled to the ion concentration environment. Except a structure in high K^+ concentration, a crystallographic structure of KcsA in low K^+ concentration was also resolved by Zhou *et al.* [4]. The two structures are referred to 'the high-salt' (PDB code 1K4C) and 'the low-salt' (PDB code 1K4D) structures. The low-salt structure is as shown in Fig. 2.3(b). Instead of pointing towards the pore axis, the carbonyl turns to bond to a water molecule outside the pore, which makes the backbone of Val^{76}–Gly^{77} twisted. The twisting backbone makes the filter an hourglass appearance. Two K^+, one at the outer and the other at the inner entryway of the filter, and in between one water molecule was resolved in the X-ray analysis. More leaking water were observed in the protein core of the filter region, comparing with the high-salt structure.

2.4. The gating of KcsA

The actual gating mechanism of KcsA is still unclear. It has been observed that the gating of KcsA represents a pH-dependent behavior: the channel is mostly closed at neutral pH, and detected open at pH < 5.0 [35, 36, 29]. It is believed that the protonated sites which are responsible for the proton activated gating of KcsA are located on the C-terminus, and they can be identified by measuring the open probability with specific cytoplasmic deletions. The Rb^+ influx in the channel of the deletion of residue 140–160 at both pH 7.0 and pH 4.0 remains the same as the full-length KcsA. In the structure with the deletion of residue 125–160, the Rb^+ influx at pH 7.0 is not affected, whereas at pH 4.0 the close probability of the channel is 50% of control, indicating that the region between residue 125 and 140 of the C-terminus is responsible for the proton activated gating of KcsA [36].

Although the gating of KcsA is coupled to the pH environment significantly, it is not identified as a pH-gated channel, because various experimental evidence shows that the C-terminus of KcsA is at the intracellular side [22]. Since *Streptomyces lividans*, like most bacteria, tightly regulates its cytoplasmic pH at neutral, it is unlikely that the channel is gated directly by interior protons [22]. Except for the pH-dependent activation, the gating of the channel is also found weak voltage-dependent [22]. To resolve the actual gating mechanism of KcsA, more knowledges of its physiological role are required.

The KcsA crystallographic structure which has been resolved is considered as the prototype for the closed conformation of K^+ channels. Then, how does the open conformation of K^+ channels look like? In 2002, a Ca^{2+}-dependent K^+ channel from *Methanobacterium thermoautrophicum*, known as the MthK, has its crystallographic structure resolved in the open state (PDB file 1LNQ) [37]. A comparison between these two structures reveals the conformational changes during gating. As shown in Fig. 2.4, the structure at the selectivity filter region is similar between these two conformations. While in MthK, the intracellular vestibule lined by the inner helices is widely opened. The inner helices are bent at a hinge point and splay out. The hinge point corresponds to a glycine, which usually serves as a flexible point in a peptide chain. The gating hinge glycine is found highly conserved in K^+ channels, which implies that there may exist a common mechanics for K^+ channels to switch between open and closed conformations. The calculation of the electrostatic potential by solving the Poisson equation shows that in a open pore, the water cavity is at the same potential as the intracellular solution, indicating that ions only have to move through the 12 Å long filter in an open pore [37].

3. Molecular dynamics simulation methods

Molecular dynamics simulation methods have long been applied to studies of biomolecules [5, 38, 7]. The first MD simulation of a biomolecule was carried out by A. McCammon *et al.* in 1976 [39]. The system was a bovine pancreatic trypsin inhibitor (BPTI) molecule in vacuum, which contains less than 500 atoms, and the simulation lasted only for 9.2 ps. A simulation for a short period like this wouldn't give much implication to its biological function. However, it shows the possibility to apply molecular dynamics methods in the study of biophysical systems. Since then, the computing power has been growing exponentially, and the force field and simulation methods have been greatly improved. The molecular dynamics methods have been applied to the study of various biophysical systems involving proteins, ligands, membranes, DNA, etc. with explicit solvent. Nowadays, the simulation of such a complex system of $10^5 \sim 10^6$ atoms for tens nanoseconds would take only weeks to a few months [7, 8].

Although the capability of molecular dynamics methods nowadays have increased significantly, still the time scale of 10∼100 ns is much shorter than the typical time scale of a biophysical reaction, which is usually of microseconds to milliseconds. Therefore, biased MD methods have been developed to overcome the time-scale limitation [40, 41]. The basic idea of biased MD methods is that based on the conventional MD methods, a kind of perturbation is applied to the target in the system to speed up the reaction. One of the biased MD methods– the steered MD method– is to apply a harmonic force to the target and make it move along a specific pathway. This method has been used mostly in the studies of the unbinding process of a ligand-protein complex. The permeation of ions through an ion channel can be considered as unbinding processes of a ligand-protein complex as well. Therefore, we have applied the steered MD methods to study the permeation process in KcsA channels in this study.

In this chapter, I will introduce the basic molecular dynamics simulation methods and the steered molecular dynamics methods. Our simulations were performed by using the AMBER programs [42]. A brief introduction of the AMBER force field will be presented in this chapter as well.

3.1. Finite difference methods of integrating the equation of motion

The equations of motion of a classical N-particle system in the Lagrangian form is

$$\frac{d}{dt}(\partial L/\partial \dot{q_k}) - (\partial L/\partial q_k) = 0, \tag{3.1}$$

where L is the Lagrangian of the system defined as the difference between the kinetic and potential energies $K - V$, and q_k is the generalized coordinates of particle k. For simplicity, we restrict ourselves to the Cartesian coordinates. For Cartesian coordinates, the generalized coordinates q_k are represented by $m_i\mathbf{r_i}$, and Eq. (3.1) becomes the familiar Newton's equation

$$m_i\ddot{\mathbf{r}}_\mathbf{i} = \mathbf{F_i}. \tag{3.2}$$

Basically, molecular dynamics is to solve the equations of motion of the N-particle system to obtain trajectories and other dynamics information of the system.

The equations of motion can be solved numerically by finite difference integration algorithm. A good integration algorithm should be accurate and efficient. Meanwhile, the conservation laws for energy and momentum must be satisfied [43]. The most widely used integration algorithms in molecular dynamics simulations are the Verlet algorithm and its variations [44, 45, 46].

The Verlet algorithm is derived as follows: for a continuous trajectory, the position of a particle at time $t + \Delta t$ can be extrapolated by Taylor expansion at time t:

$$\mathbf{r}(t + \Delta t) = \mathbf{r}(t) + \Delta t\dot{\mathbf{r}}(t) + \frac{1}{2}\Delta t^2\ddot{\mathbf{r}}(t) + \ldots \tag{3.3}$$

For Cartesian coordinates, the $\dot{\mathbf{r}}$ and $\ddot{\mathbf{r}}$ can be represented by the velocity $\mathbf{v}$ and the acceleration $\mathbf{a}$. The Taylor expansion of $\mathbf{r}$ at $t = t \pm \Delta t$ is

$$\mathbf{r}(t + \Delta t) = \mathbf{r}(t) + \Delta t\mathbf{v}(t) + \frac{1}{2}\Delta t^2\mathbf{a}(t) + \ldots \tag{3.4}$$

$$\mathbf{r}(t - \Delta t) = \mathbf{r}(t) - \Delta t\mathbf{v}(t) + \frac{1}{2}\Delta t^2\mathbf{a}(t) + \ldots \tag{3.5}$$

By adding Eq. (3.4) and Eq. (3.5), the velocity term is eliminated:

$$\mathbf{r}(t + \Delta t) = 2\mathbf{r}(t) - \mathbf{r}(t - \Delta t) + \Delta t^2\mathbf{a}(t) + \mathcal{O}(\Delta t^4). \tag{3.6}$$

The velocity at time t is needed for the kinetic energy estimation. It can be calculated using this formula:

$$\mathbf{v}(t) = \frac{\mathbf{r}(t + \Delta t) - \mathbf{r}(t - \Delta t)}{2\Delta t} + \mathcal{O}(\Delta t^3). \tag{3.7}$$

The accumulated error in Eq. (3.6) after a long integration period is of order $\mathcal{O}(\Delta t^2)$ [47]. Therefore the higher order terms in the position and velocity formulas are ignored, and the position and velocity formulas written as

$$\mathbf{r}(t+\Delta t) = 2\mathbf{r}(t) - \mathbf{r}(t-\Delta t) + \Delta t^2 \mathbf{a}(t) \tag{3.8}$$

$$\mathbf{a}(t+\Delta t) = -\frac{1}{m}\nabla V(\mathbf{r}(t+\Delta t)) \tag{3.9}$$

$$\mathbf{v}(t) = \frac{\mathbf{r}(t+\Delta t) - \mathbf{r}(t-\Delta t)}{2\Delta t}. \tag{3.10}$$

In the Verlet algorithm, to evolve the position from time t to $t+\Delta t$, only the position at time t and $t-\Delta t$, and the acceleration at time t are needed. The acceleration $\mathbf{a}(t)$ can be obtained by calculating the force. Using this formula, only storage space of $9N$ words are needed in each time step, which is rather compact for computer programming.

The Verlet algorithm has a couple of variations. One of the variations is called "the leap-frog" scheme [45], which advances the velocity a half step forward in each step:

$$\mathbf{v}(t+\frac{1}{2}\Delta t) = \mathbf{v}(t-\frac{1}{2}\Delta t) + \Delta t \mathbf{a}(t) \tag{3.11}$$

$$\mathbf{r}(t+\Delta t) = \mathbf{r}(t) + \Delta t \mathbf{v}(t+\frac{1}{2}\Delta t) \tag{3.12}$$

$$\mathbf{a}(t+\Delta t) = -\frac{1}{m}\nabla V(\mathbf{r}(t+\Delta t)). \tag{3.13}$$

In this scheme, the velocity at $t+\frac{1}{2}\Delta t$ is calculated first, and then it is used to evolve the position to $t+\Delta t$. The new position is used in the evaluation of $\mathbf{a}(t+\Delta t)$, which can be used in the calculation of $\mathbf{v}(t+\frac{1}{2}\Delta t)$. The strategy of advancement is like the leap of a frog, so comes the name "leap-frog". The leap-frog scheme avoids adding a small term $\mathcal{O}(\Delta t^2)$ to a large term $\mathcal{O}(\Delta t)$ in the original Verlet, which usually introduces numerical imprecision. For the energy calculation, it is necessary to have the position and velocity at the same time t. The velocity is usually calculated by

$$\mathbf{v}(t) = \frac{1}{2}(\mathbf{v}(t+\frac{1}{2}\Delta t) + \mathbf{v}(t-\frac{1}{2}\Delta t)). \tag{3.14}$$

Another useful variation is called the "velocity Verlet" scheme [46], which advances the position and velocity by the following formulas:

$$\mathbf{r}(t+\Delta t) = \mathbf{r}(t) + \Delta t \mathbf{v}(t) + \frac{1}{2}\Delta t^2 \mathbf{a}(t) \tag{3.15}$$

$$\mathbf{v}(t+\frac{1}{2}\Delta t) = \mathbf{v}(t) + \frac{1}{2}\Delta t \mathbf{a}(t) \tag{3.16}$$

$$\mathbf{a}(t+\Delta t) = -\frac{1}{m}\nabla V(\mathbf{r}(t+\Delta t)) \tag{3.17}$$

$$\mathbf{v}(t+\Delta t) = \mathbf{v}(t+\frac{1}{2}\Delta t) + \frac{1}{2}\Delta t \mathbf{a}(t+\Delta t). \tag{3.18}$$

The velocity Verlet scheme has the best evaluation of velocities among the three Verlet schemes. It is currently the most popular integration method in MD simulations.

The above two variations need no more than $9N$ words of storage in each time step, same as the original Verlet algorithm. The Verlet algorithm and its variations are time-reversible. This property assures no drift in the total energy for a long period. Another remarkable property of Verlet algorithm is that it is symplectic. A symplectic integrator will conserve the volume enclosed by its conjugated variables $(q_k, \dot{q}_k)$ in phase space as it evolves. This property can assure the deviation of the energy staying bounded during the simulation [47].

3.2. Constraint dynamics

The speed of a molecular dynamics simulation is restricted by the integration time step. To increase the speed of a molecular dynamics simulation, one way is to use a larger time step to integrate the equations of motion. However, the choice of the integration time step is limited by the period of the highest frequency motion in the system, which is usually associated to the vibration of covalent bonds. If the bond vibration degrees of freedom are frozen by imposing correspondent constraints, it becomes possible to use a larger integration time step.

The equations of constraint dynamics are usually solved by using the Lagrange multipliers method. For a system of N particles with M constraint, one has to solve an $M \times M$ matrix in each time step. This is applicable for a small, simple system, but less practical for a large system with polyatomic molecules. An efficient algorithm has been devised by Ryckaert *et al.* [48, 49]. This algorithm, known as SHAKE, calculates the position of each particle iteratively till the constraint equations are satisfied within a given precision, instead of exactly solving the tangled equations of motion. The SHAKE method has the advatange that it can be included in the Verlet integrator directly, and therefore is the most commonly used method in constraint molecular dymaics simulations.

Generally, the SHAKE algorithm can be applied to any constraints. Although one can use even a larger time step if other motions like the bond angle and dihedral angle are also constrained, this is usually not recommended, because it is observed that they may have significant structural effect [50]. Besides, the programs with these constraint are inefficient in that the gain from using larger time step may not compensate the extra cost from the calculation of these constraints.

In many MD simulations, the SHAKE is applied to the bond streching motion involving hydrogen atoms, which has the highest vibration frequency among all covalent bonds. With this constraint the integration time step can be increased from 1 fs to 2 fs.

3.3. Simulation with constant temperature

The simulation methods introduced in the former sections described a system at constant energy. While in experiments, it is more often to have a system at constant temperature. To mimic the experimental situation in a MD simulation, several methods have henceforth been developed to control the system temperature. In experiments, the temperature of the system is usually regulated by connecting to an external heat bath. The particles from the system and the heat bath keep colliding with the wall between them to exchange energy, and the system temperature can be maintained by this means.

Most of temperature regulation schemes in molecular dynamics simulations are based on the above idea. In a simulation, the system temperature is calculated from the kinetic energy by

$$\sum_{i=1}^{N} \frac{1}{2} m_i v_i^2 = \frac{3(N-1)}{2} k_B T. \tag{3.19}$$

That means, by modifying the velocity distribution during the simulation, one can regulate the temperature of the system. Here I introduce three commonly used schemes [43, 47]:

- **Stochastic scheme**
  H. C. Andersen first proposed a stochastic temperature regulation scheme: at random times, a randomly selected particle is assigned a new velocity drawn from a Maxwell-Boltzmann distribution corresponding to the desired temperature, which imitates the collision with an imaginary particle from the heat bath [51]. The idea of this method is intuitive and simple. While it is not as simple to determine the collision rate. If the collision rate is too low, the equilibration process is inefficient. On the other hand, if the collision rate is too high, the long-time behavior of the velocity autocorrelation function may be destroyed. Andersen has suggested that the collision rate λ_c can be derived by

  $$\lambda_c = \frac{\kappa}{\rho^{1/3} N^{2/3}}, \tag{3.20}$$

  where κ is the thermal conductivity and ρ is the particle density.

- **Weak coupling scheme**
  Berendsen *et al.* proposed a weak coupling scheme on the temperature regulation [52]. In this scheme, the coupling to the heat bath is represented by the Langevin equation

  $$m_i \dot{v}_i = F_i - m_i \gamma v_i + \xi(t), \tag{3.21}$$

  where γ is the friction parameter, and $\xi(t)$ is the Gaussian white noise. They proposed that at each time step, the velocity can be scaled by

  $$\lambda_v = [1 + \frac{\Delta t}{\tau_T}(\frac{T_0}{T} - 1)]^{1/2}, \tag{3.22}$$

where Δt is the time step, τ_T is a preset time constant, T_0 is the desired temperature, and T is the current temperature. With this friction form, the system temperature will decay to the desired temperature exponentially at the rate of τ_T. This method is efficient and simple, but has the disadvantage that the statistical ensemble corresponding to the weak coupling thermostat is unknown. It has been analytically proved that at the limit of $\tau_T = 0$, the weak coupling samples the canonical ensemble; whereas at the limit of $\tau_T = 1$, it sample the microcanonical ensemble [53].

- **Extended system scheme**
  In this scheme, the system and the heat bath together are considered as an 'extended system' by including an additional degree of freedom s to represent the heat bath. The heat bath carries a certain 'thermal inertia' represented by the thermal inertia parameter Q. The corresponding kinetic energy is

$$K_s = \frac{1}{2} Q \dot{s}^2, \tag{3.23}$$

  and the corresponding potential energy is

$$V_s = (f+1) k_B T \ln s. \tag{3.24}$$

  The Lagrangian of the extended system is

$$L = (K - V) + (K_s - V_s). \tag{3.25}$$

  The extended system method was first proposed by Nosé [54], but usually implemented using the Hoover's formulas [55]:

$$\dot{\mathbf{r}}_i = \mathbf{p}_i / m, \tag{3.26}$$
$$\dot{\mathbf{p}}_i = \mathbf{F}_i - \xi \mathbf{p}_i. \tag{3.27}$$

  The ξ is the friction coefficient, given by

$$\dot{\xi} = \frac{f}{Q}(k_B T - k_B T_0), \tag{3.28}$$

  where f is the number of degrees of freedom.

  The Nosé-Hoover thermostat is the only one which generates the true canonical ensemble. The thermal inertia parameter Q in this method has to be determined in advance. If Q is too high, the energy flow between the system and the heat bath is slow. On the other hand, if Q is too low, the system is equilibrated slowly. The choice of Q has to be done by trial and error.

3.4. Simulation with constant pressure

In experiments, not only the temperature is kept constant, but the pressure as well. The coupling to a constant pressure follows the same principle of the temperature regulation, only here the pressure tensor is regulated instead of the kinetic energy. The system box usually has to change its volume accordingly during the pressure regulation. Three popular schemes of pressure regulation are introduced as follows [43, 56]:

- **Extended system scheme**
  This method, originally proposed by Andersen [51], is similar to the extended system scheme in temperature coupling. An additional degree of freedom corresponding to the volume of the box is included. This degree of freedom acts as a 'piston' and is given a 'mass' Q. The equations of motion for this extended system are

$$\dot{\mathbf{r}}_i = \mathbf{p}_i/m + \frac{1}{3}\frac{\dot{V}}{V}\mathbf{r}_i, \tag{3.29}$$

$$\dot{\mathbf{p}}_i = \mathbf{F}_i - \frac{1}{3}\frac{\dot{V}}{V}\mathbf{p}_i, \tag{3.30}$$

$$\ddot{V} = \frac{1}{Q}[P - P_0]. \tag{3.31}$$

  where V is the volume, $P(t)$ is the current pressure, and P_0 is the desired pressure. Andersen proved that the solution of these equations generates trajectories in the isobaric-isoenthalpic ensemble, where the pressure and enthalpy of the system are constant.

  The choice of the piston mass Q determines the decay time of the volume fluctuations. Andersen suggested that the time scale for volume fluctuations should be about the same as the as the time required for a sound wave to travel through the box [51].

- **Weak coupling scheme**
  A particularly simple pressure coupling method was developed by Berendsen *et al.*

$$\dot{\mathbf{r}}_i = \mathbf{p}_i/m + \frac{1}{3}\frac{\dot{V}}{V}\mathbf{r}_i, \tag{3.32}$$

$$\dot{\mathbf{p}}_i = \mathbf{F}_i, \tag{3.33}$$

$$\dot{V} = \frac{\chi}{\tau_P}[P - P_0]V, \tag{3.34}$$

  where χ is the isothermal compressibility and τ_P is the pressure coupling time. Different from the extended system scheme, here the equation of volume is first order. τ_P is a preset parameter, which determines the decay time of volume fluctuations. The disadvantage of this scheme is, same as in the temperature coupling

scheme, that the trajectories generated by it corresponds to an unknown ensemble. Its simplicity for programming makes it the most popular scheme.

- **Langevin piston scheme**
  This scheme was proposed by Feller *et al.* [56] to resolve the difficulties of the previous two methods. The motion of piston in the weak coupling scheme can be considered to be overdamped, while in the extended system scheme it is undamped. In the Langevin piston scheme, the piston is allowed to move with partial damping represented by applying the Langevin equation on the volume term:

$$\dot{\mathbf{r}}_i = \mathbf{p}_i/m + \frac{1}{3}\frac{\dot{V}}{V}\mathbf{r}_i, \tag{3.35}$$

$$\dot{\mathbf{p}}_i = \mathbf{F}_i - \frac{1}{3}\frac{\dot{V}}{V}\mathbf{p}_i, \tag{3.36}$$

$$\ddot{V} = \frac{1}{Q}[P - P_0] - \gamma\dot{v} + \xi(t), \tag{3.37}$$

  where γ is the collision frequency and $\xi(t)$ is the Gaussian white noise.

  This scheme can produce trajectories in the real NPT ensemble. While the exchange of thermal energy is slow in this scheme, combination of other more efficient temperature regulation schemes, such as the Nosé-hoover thermostat, may be required when carrying out simulations in the NPT ensemble.

3.5. The long-range interaction

A pair interaction which decreases slower than r^{-d}, where r is the pair distance and d is the dimensionality of the system, is defined as a long-range interaction, such as the electrostatic interaction ($\sim r^{-2}$) and the dipole interaction ($\sim r^{-3}$) are considered long ranged. In order to obtain correct results, basically all interaction pairs should be taken into account in the computation of long-range interactions. That means the computation of long-range interactions is a $\mathcal{O}(N^2)$ problem, which makes it very expensive for the simulations of large systems. Especially when employing the periodic boundary conditions, where there are infinite number of unit cells, the number of interaction pairs is infinite as well.

A lot of effort has been spent on finding efficient and precise methods on the calculation of long-range interactions. In periodic boundary conditons, a commonly used method is called the "*Ewald summation method*" [57]. The method was originally developed for the energy calculation in an ionic crystal, which is a natural periodic system. The Coulomb potential U in a periodic system of N particles is the sum of all interaction pairs in the unit cell as well as the image cells

$$U = \frac{1}{2}{\sum_{\mathbf{n}}}' \sum_{i=1}^{N}\sum_{j=1}^{N} q_i q_j |\mathbf{r_{ij}} + \mathbf{n}L|^{-1}, \tag{3.38}$$

where L is the length of the unit box (assumed to be cubic here), $\mathbf{n}$ represents the integer set (n_x, n_y, n_z) and the prime on the sum means that $i \neq j$ for $|\mathbf{n}| = 0$. For simplicity, the factor $1/4\pi\epsilon_0$ is omitted. Eq. (3.38) is conditionally convergent, i.e. the convergence of the interaction depends on the order of summation. Ewald introduced a *convergence factor* $e^{-s|\mathbf{n}|^2}$ here. By multiplying this factor to the right hand side of Eq. (3.38), one obtains

$$U = \frac{1}{2}\sum_{\mathbf{n}}{}' e^{-s|\mathbf{n}|^2}\sum_{i=1}^{N}\sum_{j=1}^{N} q_i q_j |\mathbf{r_{ij}} + \mathbf{n}L|^{-1}, \tag{3.39}$$

which becomes absolutely and uniformly convergent when $s > 0$. At the limit as $s \to 0$, Eq. (3.39) is equal to the original form. In the condition of charge neutrality, Eq. (3.39) can then be shuffled and transform into different converging terms [57, 58]

$$\begin{aligned} U &= \frac{1}{2}\sum_{\mathbf{n}}{}'\sum_{i=1}^{N}\sum_{j=1}^{N} q_i q_j \frac{\mathrm{erfc}(\alpha|\mathbf{r_{ij}} + \mathbf{n}L|)}{|\mathbf{r_{ij}} + \mathbf{n}L|} \\ &\quad + \frac{2\pi}{L^3}\sum_{\mathbf{k}\neq 0}\sum_{i=1}^{N}\sum_{j=1}^{N} q_i q_j \frac{e^{-|\mathbf{k}|^2/4\alpha^2}}{|\mathbf{k}|^2} e^{i\mathbf{k}\mathbf{r}_{ij}} \\ &\quad - \frac{\alpha}{\sqrt{\pi}}\sum_{i=1}^{N} q_i^2 + \frac{2\pi}{3L^3}|\sum_{i=1}^{N} q_i \mathbf{r}_i|^2. \end{aligned} \tag{3.40}$$

$\mathrm{erfc}(x)$ is the complementary error function, and α is a chosen parameter for the Gaussian distribution function introduced into the equation during the transformation. The first term of Eq. (3.40) is short-ranged if α is chosen to be large enough. In this case, only the sum in the unit cell (i.e. $\mathbf{n} = 0$) has to be taken into account. The second term converges rapidly as well in the reciprocal Fourier space because of the $exp(-|\mathbf{k}|^2/4\alpha^2)$ term.

The physical meaning of this summation method is described as the following: in order to make the Coulomb potential for a point charge in the system converge fast, a charge distribution of the opposite sign is placed at the position of the point charge. The counter charge distribution is usually chosen to be a Gaussian distribution. It is like the point charge is screened by the counter charge in the system, which results in the short-range Debye-Huckel potential. Then the effect of the added counter charge has to be taken into account, which is the long-range part of the summation. This part is then summed up in the Fourier space, which makes it converge fast.

Eq. (3.40) is an exact transformation of Eq. (3.38). It resolves the problem of summing up infinite terms in a periodic system. But still the complexity of the sum is $\mathcal{O}(N^2)$. For more efficient computation of the long-range forces, one usually combines the Ewald sum with the *particle-particle* (PP) and *particle-mesh* (PM) algorithm [59]. The particle-particle algorithm is only a direct sum of the pair interactions, used to treat the short-range part of the Ewald sum. And the long-range part is treated by the particle-mesh

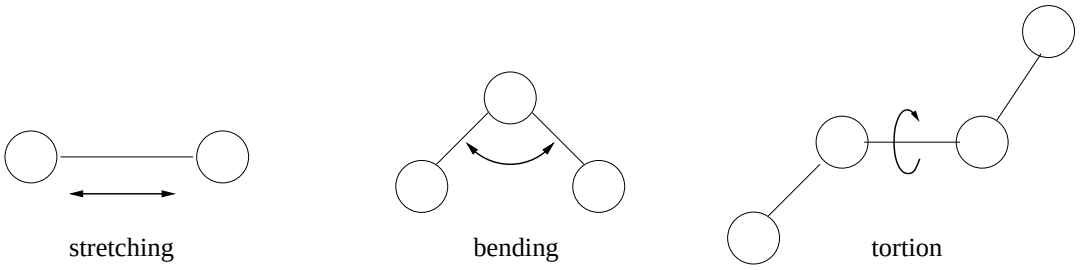

Figure 3.1.: The bonded terms in the force field: bond stretching (left), bond angle bending (middle), and dihedral angle rotation (right).

method. In the PM method, a cubic grid is superimposed to the system. The point charges of the system are then "meshed up" to the four neighboring grid points. The potential is then calculated by solving Poisson's equation on the grid. By applying the fast Fourier transform technique to solve Poisson's equation, the complexity of the calculation can be reduced to $\mathcal{O}(N\ln N)$ [59].

3.6. The force field

One of the important steps for biomolecule modeling is to determine the interaction form between atoms, or the so called *force field*. Generally, a biomolecule modelling force field contains two parts: bonded terms and nonbonded terms. The bonded terms include the bond stretching, bond angle bending, and dihedral angle rotation terms, as illustrated in Fig. 3.1). The non-bonded term usually include the van der Waals and electrostatic interactions. Different force fields may include some additional terms. Currently, the most widely used programs on biomolecule modelling are AMBER, CHARM/NAMD, and GROMOS. The main difference of the force field among these programs is the charge fitting philosophy.

We mainly use the AMBER programs [42] in our study. The first generation force field of AMBER developed by Weiner *et al.* has the following form [60]

$$\begin{aligned} U_{\text{total}} &= \sum_{\text{bonds}} K_r(r-r_{eq})^2 + \sum_{\text{angles}} K_\theta(\theta-\theta_{eq})^2 + \sum_{\text{dihedrals}} \frac{V_n}{2}[1+\cos(n\phi-\gamma)] \\ &\quad + \sum_{i<j}\left[\frac{A_{ij}}{R_{ij}^{12}} - \frac{B_{ij}}{R_{ij}^{6}} + \frac{q_iq_j}{\epsilon R_{ij}}\right] + \sum_{\text{H-bonds}}\left[\frac{C_{ij}}{R_{ij}^{12}} - \frac{D_{ij}}{R_{ij}^{10}}\right]. \end{aligned} \tag{3.41}$$

The first three terms are the bond stretching, bond angle bending, and dihedral angle rotation terms, respectively. The nonbonded terms include the electrostatic interaction, the 6-12 van der Waals interaction for non-hydrogen bond, and the 10-12 function for hydrogen bonded terms. The 10-12 hydrogen bonded term is an empirical function. It

is mainly to prevent the occurrence of unrealistic short hydrogen bonds and to fine-tune the hydrogen-bond distance [60]. In the second generation force field of AMBER developed by Cornell *et al.*, the 10-12 H-bond terms are omitted [62]. The AMBER force field parameters are developed by the following steps: first a set of initial parameters are determined; then simulations on various model systems like proteins and nucleic acids are carried out using AMBER programs. The simulation results are then compared with the experimental data to adjust the parameter set. The quality of parameter set obtained from this method is limited by the number of available systems in experiments, and the parameter set is optimized only to these test systems. Since the experimental data of various macromolecules is accumulating, the reliability of the parameter set is improved with time.

The force field parameters development in AMBER is briefly introduced in the following:

Atom types The first step in parameter development is the choice of atom types. In the case of a quantum mechanical calculation, only a single atom type is need for each atom; that means, only the number of electron is relevant. In AMBER, except the explicit atom model, the carbons with implicit inclusion of hydrogens can be treated as a united atom. The development of united-atom parameters is to save the computing time. Currently it is still used in some model system, such as the long hydrocarbon chains of lipid molecules.

Bonded parameters The equilibrium parameters for bond length r_{eq}, bond angle θ_{eq}, and the torsion angle γ are usually taken from microwave and X-ray data on appropriate compounds. Most of K_r and K_θ are obtained from the normal-mode calculations, in which the K_r is determined by the best fit to experimental frequencies of the test molecules. The development of torsion parameters V_n basically followed the same line; only more modification was required during the test case, because the torsion terms and the nonbonded terms are highly coupled.

VDW parameters The 6-12 van der Waals parameters can be derived from the interatomic distance R^* at the van der Waals minimum and the van der Waals well depth ϵ^*. The parameters R^* and ϵ^* can be derived from a fit of the lattice energy and crystal structures [60]. The van der Waals radii are dominated by the number of electrons in an atom and are not very sensitive to the chemical environment. Thus, to derive the van der Waals parameters for a new atom type, the first step is to find analogy from the pre-existing parameters. For organic compounds, the parameters may be found by analogy based on element and bond order alone. The 6-12 van der Waals parameters can be derived from the atomic radius R^* and the potential well depth ϵ^*. For those of which no available analogy could be found, such as metals, the atomic radii R^* can be derived from experimental measurements, like neutron or X-ray diffraction data. The parameter ϵ^* is usually derived from the solvation free energy. The parameters thus derived depends on

the solvent type. In AMBER, the most common solvent type is the TIP water model [64]. Most van der Waals parameters in AMBER are adapted to the TIP water model.

The parameters of the 10-12 hydrogen-bonded term use the geometric mean of the parameters of H and the H-bond acceptor atom.

Electrostatic parameters The most difficult part of the derivation of the force field parameters is to determine atomic charges. The first generation Weiner *et al.* force field uses quantum mechanical calculations to derive electrostatic potentials (ESP) fit the atomic charges. The electrostatic potential at each grid point is calculated from the quantum mechanical wave function. The charges thus derived depend on the choice of the basis set. The Weiner *et al.* force field used the STO-3G basis set for the charge derivation. The derived charges reproduce interaction energies well, but it is not well balanced with the TIP water models, which have empirically derived higher charges. The second generation Cornell *et al.* force field uses a modified ESP fit– the RESP (restrained ESP) fit charge model to derive atomic charges [65, 63, 62]. The basis set of choice is the 6-31G* basis set, which is bigger and better than the STO-3G. The basic idea of RESP is that besides the original ESP fit, additional restraints are applied to the charges on non-hydrogen atoms. These restraints serve to reduce the charges which can be reduced without affecting the fit. This algorithm has a better determination on the charges of buried atoms. The RESP charge model shows good reproduction of the interaction energies and the solvation free energies. When a 1-4 scaling of electrostatic interaction (the electrostatic interaction between atoms separated by exactly three bonds) is applied, the charge model produces good conformational energies for many systems of test.

3.7. The steered molecular dynamics simulation method

The time scale which a molecular dynamics simulation can reach is still much shorter than the time scale of most biological reactions. To overcome this time-scale limitation, various biased molecular dynamics methods have therefore been developed. In this section, I am going to introduce one of the biased methods– the steered molecular dynamics simulation method, which is employed in our study of the ion channel conduction.

The steered molecular synamics (SMD) simulation method is innovated by the atomic force microscopy (AFM) technique, which has been applied to the study of the unbinding processes of ligand-protein complexes. In AFM experiments, an elastic cantilever tip is attached to a linker molecule of the ligand-protein complex. Retracting the cantilever induces a dissociation of the ligand from its binding pocket. The applied force is monitored during the process, and the peak of the data is labeled as the rupture force along the unbinding pathway [66, 67].

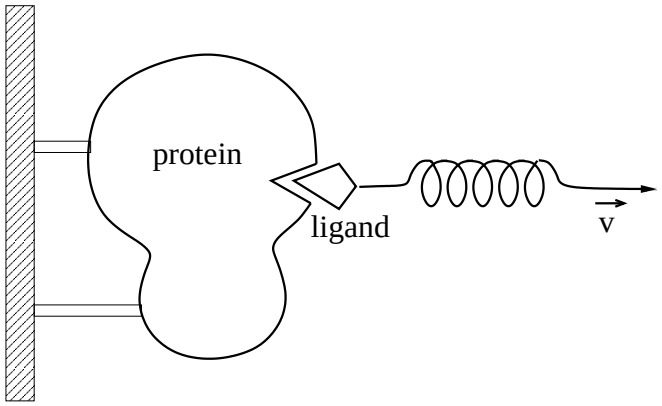

Figure 3.2.: A schematic picture of the steered molecular dynamics simulation method.

Inspired by AFM experiments, in the SMD simulation method an external force is applied to the target ligand by attaching it to a symbolic "spring", as shown in Fig 3.2. By this means, the ligand is connected to a harmonic potential

$$U = k_0(x - x_0)^2/2, \tag{3.42}$$

where k_0 is the spring constant, x is the coordinate of the linker molecule, and x_0 is the initial position of the end point of the spring. The "spring" is shifted along a specific reaction coordinate subsequently with a constant velocity v, as in the AFM experiments, and the force exerted on the ligand is

$$F = k_0(x_0 + vt - x). \tag{3.43}$$

By this manipulation, the ligand is able to explore a larger configuration space, and a dissociation process of the ligand-protein complex can be induced [68, 69, 70, 71].

A general problem of applying steered MD simulation method is to select a proper reaction pathway. In some cases a straight line path is sufficient, e.g. in avidin-biotin unbinding, extraction of lipids from membrane, actin phosphate release, etc. [68, 72, 70, **?**]. In other biomolecule systems, more complicated methods to decide the reaction pathway are required. The direction of the pulling force may have to be changed during the simulation to avoid deformation of the protein structure. It can be chosen randomly or based on the structure information. The direction can be decided by various weighting schemes, which is problem specific [69, 73]. The permeation problem of ion channels is relatively simple in this respect. Ion permeation through the narrow selectivity filter of a KcsA channel is a quasi-one-dimensional process. Therefore it is natural to choose the pore axis as the reaction coordinate in steered MD simulations of KcsA channels. In steered MD simulation, not only the pathway, but also the direction of the reaction is assigned, which is advantageous in the ion permeation study.

4. Steered molecular dynamics simulations of KcsA channels

To explore the ion permeation mechanism in a K^+ channel, we have applied the molecular dynamics simulation methods to a model K^+ channel embedded in a lipid membrane. The K^+-channel model is based on the crystallographic structure of the KcsA channel [3, 4, 34]. Two MD trajectories were generated for reference, and six steered molecular dynamics simulations with two simulation schemes were proceeded. The two steered MD schemes are referred to the single-ion SMD and the multi-ion SMD simulation. In this chapter, I will present the construction of the model system and the simulation protocols. The analysis of the structural properties of the channel protein are given in this chapter as well. The dynamical part of the simulation result will be discussed in the next chapter.

4.1. Constructing the channel-membrane model

An atomic model of the KcsA channel embedded in the lipid bilayer has been constructed for the molecular dynamics simulations. The atomic coordinates of the KcsA channel were taken from its crystallographic structure in file 1BL8 in the Protein Data bank (PDB) [74]. The structure is resolved by Doyle et al. with the X-ray diffraction method at the resolution of 3.2 Å [3]. Details of the KcsA channel structure have been introduced in Chapter 2. The four monomers of the KcsA channel were denoted by M1, M2, M3, and M4 in our model. The coordinates of the side-chains of residue Arg^{27}, Ile^{60}, Arg^{64}, Glu^{71}, and Arg^{117} were not determined in the crystallographic data. They were added by the program LEaP [75].

In the selectivity filter, the backbone carbonyl oxygens of the filter residues form four and a half binding sites, referred to S_0 to S_4, as illustrated in Fig. 4.1(a). An extra site S_{ext} located outside the extracellular mouth was identified in the KcsA crystallographic structure of higher resolution. Three K^+ were placed in the selectivity filter at site S_1, S_3, and S_4, same as given in the crystallographic data, referred to K1, K2, and K3 respectively. One water molecule, denoted by W1, was placed in site S_2 of the selectivity filter between K1 and K2. The initial configuration of the selectivity filter is as shown in Fig. 4.1(b).

The pore of the KcsA channel forms a cavity of 10 Å in diameter located in the middle of the bilayer when embedded in the membrane [3]. The empty space in the cavity and

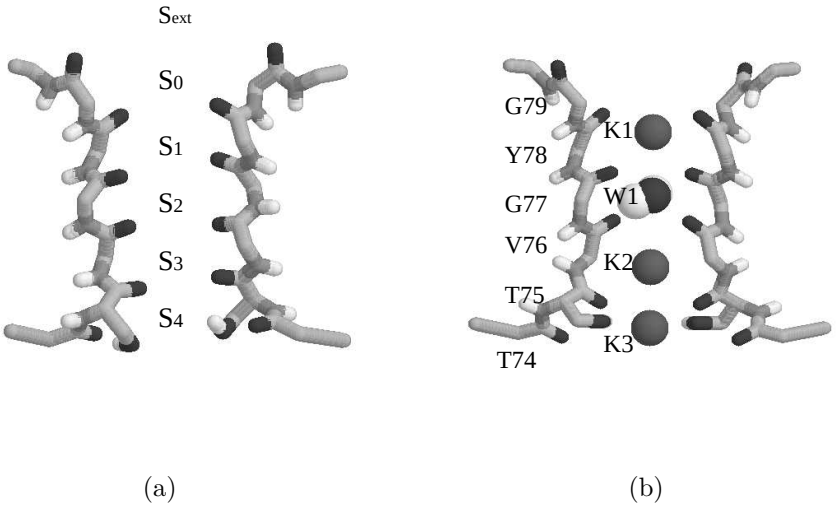

Figure 4.1.: (a) The definition of the binding sites in the selectivity filter. (b) The initial configuration of the selectivity filter.

the 18 Å long intra-vestibule of the channel was filled with TIP3P water molecules by programs. In the subsequent equilibration process by restraining the coordinates of the protein atoms and three K^+, the waters in close contact with the protein atoms were removed from the model. After that, 50 water molecules remained in the channel pore, among them ~ 40 were in the cavity region.

The channel protein was then inserted in a palmitoyloleoyl phosphatidylcholine (POPC) lipid bilayer. The initial configuration of the POPC bilayer, containing 200 lipid molecules solvated by TIP3P model waters, was provided by Dr. Heller [76]. The lipid-solvent system was pre-equilibrated in the former study [77]. To insert the KcsA channel into the bilayer, we first estimated the size of the channel protein, a hole of about this size was then created by removing the corresponding number of lipid molecules. Because of the asymmetric shape of KcsA, the number of removed lipid molecules were unequal in the upper and lower parts of the bilayer— 55 lipid molecules from the upper layer and 41 from the lower one have been removed. The protein was inserted parallel to the membrane norm with the C_α of Arg^{80} located around the average position of the phosphate group of the upper lipid layer. The membrane-protein system was then solvated by TIP3P model waters. Eleven Cl^- were added to keep the system neutral.

The resultant channel-membrane model contains 388 amino residues (97 residues in each monomer, 5908 atoms in total), 104 lipid molecules, with 45 in the upper and 59 in the lower layer, and 5822 water molecules, in total 28928 atoms. The solvated channel-membrane system is as shown in Fig. 4.2.

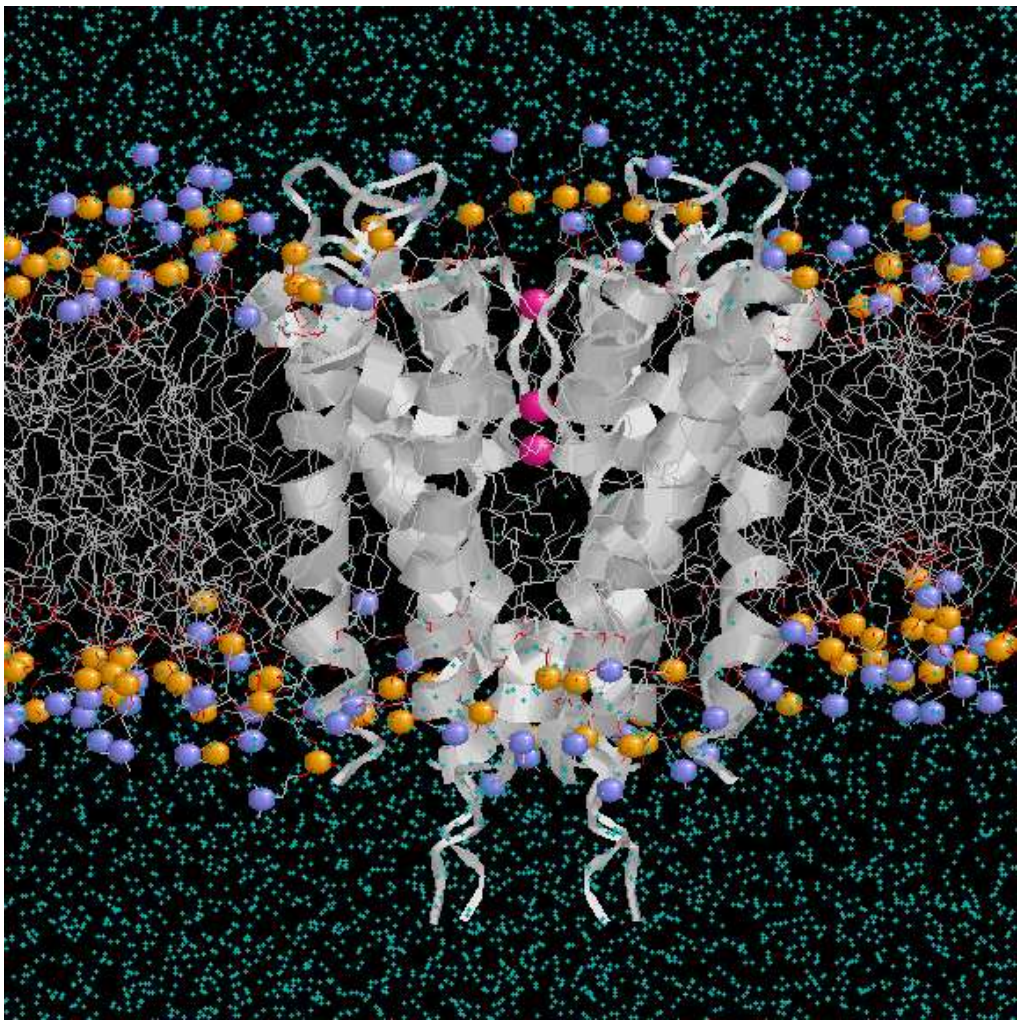

Figure 4.2.: The model of the KcsA channel embedded in POPC lipid bilayer solvated by TIP3P water molecules. The channel is represented with ribbons. Three K^+ (magenta) located in the selectivity filter of the channel were denoted by K1, K2, and K3 from upper to lower. Water molecule W1 (cyan) located between K1 and K2 is shown with spacefill. The nitrogen and phosphate atoms of the lipid head group are displayed with spacefill in blue and yellow respectively.

4.2. Protonation state of side-chain ionizable residues in the KcsA channel

The electrostatic interaction is the most dominant term in a biophysical system, and therefore it is important to determine the charge state of each atom in the system. Among the twenty amino acids, seven of them have ionizable side chains (see Table A.1). The ionization probabilities are represented by their pK_A values, which depend on several environmental parameters like temperature, ionic strength, and the microenvironment of the ionizable group [78]. Details of the definition and the calculation of pK_A values are described in Appendix A.

The pH environment of our simulations is set to 7. Forty amino residues (ten in each monomer) of the KcsA channel have ionizable side chains. They are His^{25}, Arg^{27}, Glu^{51}, Arg^{52}, Arg^{64}, Glu^{71}, Asp^{80}, Arg^{89}, Arg^{117}, and Glu^{118}. Among them the ionization states of Glu^{71} and Asp^{80}, which are close to the selectivity filter, directly influence the permeation process of the ion channel. It has been suggested by both experimental and theoretical studies that the Glu^{71}, which is buried inside the protein and hence has a lower probability to contact solvent environment, should be in a protonated (neutral) state, while the Asp^{80} which is exposed to the solvent is ionized [79, 80, 81]. The side chains of Glu^{71} and Asp^{80} are predicted to form a strong hydrogen bond which is essential for the stability of the selectivity filter structure [3, 81]. The pK_A value of histidine is about 6.0, implying that it is usually weakly charged in pH7 environment. Here we set His^{25} to its δ-form, which is a neutral state, in our model. The other side-chain ionizable groups of the protein are located mostly at a solvent exposed area and therefore are assigned to their ionized state.

4.3. Simulation protocol

The simulation was carried out with the program SANDER of AMBER5.0 [42] on supercomputer CRAY T3E in the Zentralinstitut für Angewandte Mathematik (ZAM) of Forschungszentrum Jülich. SANDER, the acronym of **S**imulated **A**nnealing with **N**MR-**D**erived **E**nergy **R**estraints, is the main program of AMBER for molecular dynamics simulations. The program has been parallelized under the Message Passing Interface (MPI) standard and been optimized according to the environment of different platforms. All parameters of atomic properties and interactions in the simulations were taken from the AMBER '91 parameter set, except the protonated glutamates, which were taken from the '94 parameter set. The carbons with their covalent hydrogen atoms in the hydrocarbon chain of the lipid molecules were treated as a united-atom. In SANDER, the equation of motion is integrated by using the Verlet leap-frog algorithm. Periodic boundary conditions were applied to all three dimensions of the system. The simulation was done under the NPT condition. The temperature was kept to 300 K by applying the Berendsen coupling algorithm on the temperature scaling [52]. The atoms of solute

and solvent were coupled to separate heat baths to prevent the "cold solute/hot solvent" problem [82]. The pressure was kept to 1.0 Bar by using the anisotropic scaling with the coupling constant equal to 0.1. The SHAKE constraint algorithm was employed to remove the stretching freedom of all bonds involving hydrogens. In SANDER, the Particle mesh Ewald (PME) summation method [83, 84] with B-spline interpolation and fast Fourier transforms (FFT) were used for calculating the electrostatic and Lennard-Jones interactions. The order of B-spline interpolation was set to 4, implying a cubic spline approximation, and the size of the charge grid was ~ 1 Å in each dimension. The direct sum tolerance of PME was 0.00001. The 1-4 van der Waals and the 1-4 electrostatic interactions (van der Waals/electrostatic interactions separated by only three covalent bonds) were both scaled by the factor 2.0 [60, 61]. The equation of motion was integrated with a time step of 2 fs. The atomic coordinates were saved every 1 ps and the velocity every 10 ps. One pico second calculation took 4–5 minutes on average on CRAY T3E using 32 nodes, so 1 ns simulation took about 150 computing hours.

We have carried out two sets of MD simulations, referred to 'KCM1' and 'KCM2' respectively, based on different crystallographic structures (PDB file 1BL8 and 1K4C). In simulation 'KCM1', the energy minimization was done for 100 cycles, in which the first 10 cycles was done by steepest descent method, then switched to conjugate gradient method in the rest of the minimization. The structure of the KcsA channel and the three K^+ and water molecule W1 were kept intact in the minimization and the first 50 ps of the simulation by turning on the belly option, by which the coordinates of the selected atoms were frozen to its original structure. The simulation time was reset to zero when the protein was released from the constrained forces. The system reached its equilibrated density after 150 ps, and in total a 2 ns MD trajectory was generated. The data from the first 50 ps constraint run are not included in the analysis shown in this chapter.

The structure of the KcsA channel in simulation KCM1 doesn't show a good stability, especially at the selectivity filter region. Some of the missing atoms in PDB file 1BL8 are indeed crucial for the maintainance of the structure, especially the side chains of Glu^{71} at the filter region, which lie in the core part of the protein. According to the study of protein folding problems, a folding process has to go through a glassy energy landscape to find its native state, implying that it may take an infinitely long time to achieve the folded state on computer. Therefore, we performed another simulation 'KCM2', started with a conformation more close to the correct channel structure. In simulation 'KCM2', the structure of the KcsA channel is based on the crystallographic data (PDB file 1K4C) obtained by Zhou et al. with 2.0 Å resolution in 2001 [4]. Except for the higher resolution, the new structure file contains the coordinates of the side-chain atoms which were missing in file 1BL8. However, in file 1K4C, only the coordinates of a single monomer are given. To construct a tetramer structure from it, we took the crystallographic structure in file 1BL8 as a template, and employed the "orthogonal transformation method" [85, 86] to generate the optimal superposition between the structure of the 1K4C monomer and each monomer in 1BL8. The initial conformation of the simulation KCM2 was taken from simulation KCM1 after the system reached its

equilibrium size. The channel protein, three K^+, and water molecule W1 were restrained to the reference structure by gradually increasing the restraint constant in the first 60 ps. The restraint forces exerted on the protein were then slowly released in another 90 ps. The atomic coordinates of the channel protein were relaxed for 210 ps with restrained K1, K2, K3, and W1. After then the system was completely released and the simulation was continued for another 1 ns.

4.4. Steered MD simulations of ion translocation processes in the KcsA channel

The permeation rate of a KcsA channel can reach 10^8 ions per second, that is, it takes ~ 10 ns for a K^+ to permeate through the channel. To reach this time scale for a system like our model using conventional MD simulation methods, it is about the limit of current computing power. Therefore, we proposed to apply the *steered molecular dynamics* to our system to increase the probability of the permeation event. To study the multi-ion conduction process, two simulation schemes were proposed by different manipulation protocol: in one scheme, the external force was exerted to one potassium ion, and in another scheme the external forces exerted to all three potassium ions simultaneously, standing for the single-ion and multi-ion permeation processes respectively.

4.4.1. Single ion steered MD simulation

The initial configuration of the single-ion SMD simulation is taken from the MD simulation KCM2 after equilibration. As shown in Fig. 4.3(a), potassium ion K1 and K2 remain in the selectivity filter at site S_1 and S_3, and K3 in the central cavity close to S_4. Water molecule W1 is located at S_2 between K1 and K2, and another water replaces K3 sitting at S_4, generating an occupancy state (K–W–K–W) in the selectivity filter. An external force F was applied to ion K1 by attaching it to a symbolic spring. The pore axis of the channel was considered as a natural reaction coordinate of the ion translocation process. The spring was shifted towards the extracellular mouth with velocity v along the pore axis, as illustrated in Fig. 4.3(a). The mechanical force exerted on K1 is given by

$$F = k_0(z_{K1}(t) - z_0(t)), \tag{4.1}$$

where k_0 is the spring constant, z_{K1} is the position of K1, and z_0 is the position of the end point of the spring.

The steered MD simulation was done by the modified SANDER of AMBER5.0 [42] on the supercomputer CRAY T3E in ZAM of Forschungszentrum Jülich. The model system and the simulation protocol were the same as in the previous MD simulations.

We have carried out three single-ion SMD simulations, referred to SMD1, SMD2, and SMD3, starting with three different initial conformations taken from the previous MD

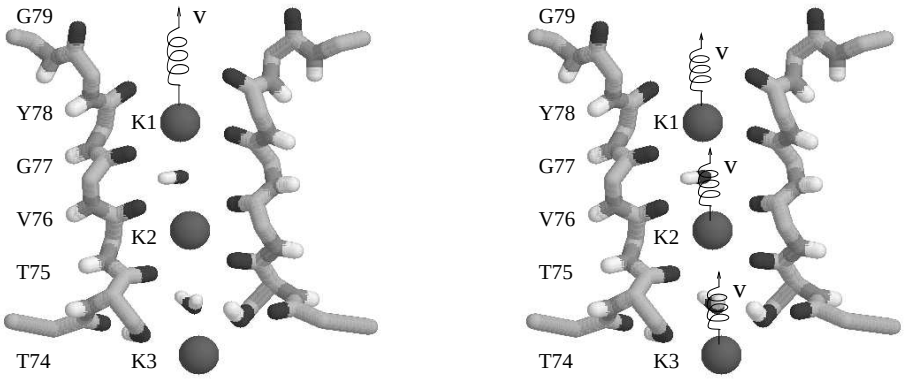

Figure 4.3.: The single-ion (a) and the multi-ion (b) steered MD simulation schemes.

simulation KCM2. The initial ion occupancy states of the selectivity filter were the same for all three simulations. A spring constant k_0 of 140 pN/Å was used in all simulations, and the spring was moved along the z-axis with a constant velocity $v = 0.015$ Å/ps. The thermal fluctuation of the constrained coordinate is $(k_BT/k_0)^{1/2} \approx 0.55$ Å, and the corresponding force fluctuation is $(k_BTk_0)^{1/2} \approx 76$ pN. The coordinates of the spring were updated every 1 ps. A 500 ps trajectory was generated for each simulation.

4.4.2. Multi-ion steered MD simulation

The multi-ion steered MD simulations were implemented by applying external forces to all three potassium ions K1, K2, and K3 simultaneously, to generate an artificial multi-ion permeation process. It corresponds to attaching three symbolic springs to the three potassium ions respectively and shifting the springs along the pore axis towards the extracellular mouth with the same velocity, as illustrated in Fig. 4.3(b). Three sets of simulations were conducted, denoted by SMD4, SMD5, and SMD6, starting with the same initial configurations as in the single-ion SMD simulations SMD1, SMD2, and SMD3 correspondingly. The rest of the simulation protocol is same as in the single-ion SMD simulations.

For the comparison with the single-ion SMD simulations, we use the same spring constant $k_0 = 140$ pN/Å and shifting velocity $v = 0.015$ Å/ps in all three potassium ions in the muti-ion SMD simulations. The thermal fluctuation of each constrained coordinate is ≈ 0.55 Å, and the corresponding force fluctuation is ≈ 76 pN, same as in single-ion SMD simulations. The coordinates of the spring were updated every 1 ps. A

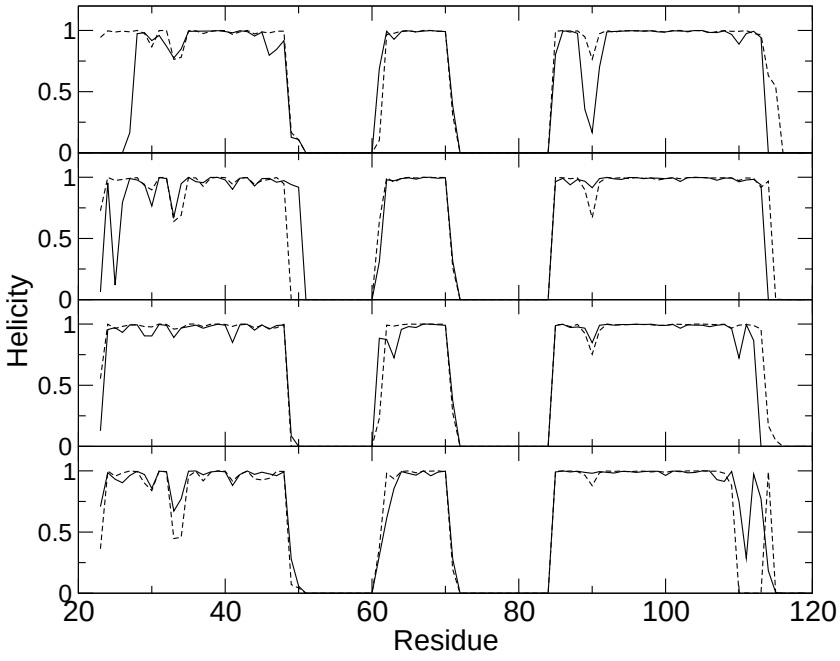

Figure 4.4.: The average helicity of each residue from simulation KCM1 (solid) and KCM2 (dashed) in monomer M1, M2, M3, and M4 (from top to bottom). The three humps correspond to the TM1, P, and TM2 helix (left to right).

500 ps trajectory was generated for simulation SMD4 and SMD5, and a 600 ps trajectory for SMD6.

4.5. Average structural properties of the KcsA channel in the simulations

4.5.1. The stability of the helical structure

The α-helix is one of the basic structural components of proteins. The conformation of a helix is like a twisting spiral with the backbone of the peptide lying inside and the side

	1BL8	KCM1	KCM2	SMD1	SMD2	SMD3
Helicity	0.69	0.62	0.64	0.65	0.65	0.64
				SMD4	SMD5	SMD6
Helicity				0.65	0.64	0.65

Table 4.1.: The average helicity of the channel protein in each simulation, comparing with the helicity of the crystallographic structure in PDB file 1BL8.

Structure elements	KCM1	KCM2	SMD1	SMD2	SMD3
Full structure	2.79	1.70	1.73	1.79	1.76
Filter (E^{71}-D^{80})	1.34	0.66	0.64	0.72	0.65
			SMD4	SMD5	SMD6
Full structure			1.83	1.79	1.81
Filter (E^{71}-D^{80})			0.65	0.62	0.64

Table 4.2.: Average C_α-RMSD relative to the initial structure in Å.

chains pointing outward. It is formed by hydrogen bonding between the carbonyl and amide groups along the peptide: the oxygen from the CO group of residue i is bonded to the hydrogen from the NH group of residue $(i + 4)$ along the peptide. The helical structure is then stabilized by these hydrogen bonds. In the KcsA channel, there are three α-helices in each monomer: two transmembrane helices from residue 24-51 and residue 86-118, denoted by TM1 and TM2 respectively, and in between a P-loop helix from residue 62-73 (see Fig. 2.1).

The stability of the helical structure in a biomolecular simulation is one of the indications of the reliability of the model and simulation programs. To verify the stability of the helical structure in our simulations, we have calculated the distance between the carbonyl oxygen of residue i and the amide hydrogen of residue $(i + 4)$ along each monomer. A cut-off radius of 2.5 Å was set as the upper limit of a hydrogen bond [78]. The "helicity" of a single residue is then defined by the time it is involved in a helical hydrogen bonding divided by the total simulation time. Figure. 4.4 shows the average helicity of each residue of the four monomers from simulation KCM1 and KCM2. The humps of the data correspond to the three α-helices TM1, P, and TM2. The figure shows that the helical structure is on average better preserved in KCM2. The terminus in the cytoplasmic side (N-terminus of TM1 and C-terminus of TM2), which have contact with solvent, are loosened. The P-helices, which have important functional role, are well preserved in all simulations, except in KCM1. The average helicity of the whole channel in simulation KCM1, KCM2, and SMD1–6 are given in Table 4.1. The helicity of the crystallographic structure in PDB file 1BL8 is equal to 0.69. The average helicity of the channel is higher in KCM2 than in KCM1. In simulations SMD1–6 they are about the same value as in KCM2.

4.5.2. The RMS deviation of the KcsA channel structure

The integral structural variation of the KcsA channel during the simulation can be presented by the root-mean-square deviation (RMSD) of the structure. The RMSD of the structure was calculated by employing the "orthogonal transformation method" [85, 86]. By using this method, a rotation matrix, which optimizes the superposition between a given structure and a referenced one, is obtained, and the RMSD is equal to

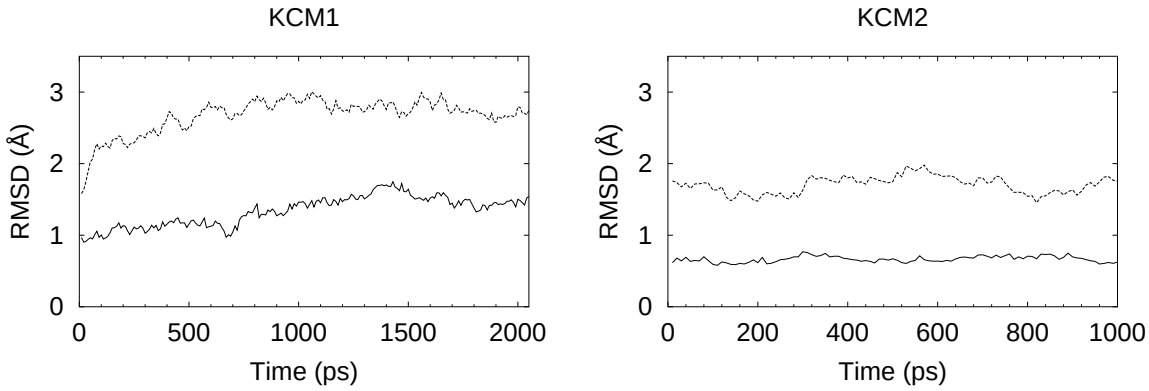

Figure 4.5.: Time variation of the C_α-RMSD of the selectivity filter from Glu^{71} to Asp^{80} (solid), and the whole KcsA channel (dashed) of simulation KCM1 and KCM2.

the minimum eigenvalue of this rotation matrix. Details of this method are described in Appendix B. The crystallographic structure in PDB file 1BL8 was taken as the reference structure for the RMSD calculation of simulation KCM1, and the structure in PDB file 1K4C as the reference structure of KCM2 and all SMD simulations. We have calculated the time average RMSD of C_α atoms from the full structure and from the selectivity filter (residue Glu^{71} to Asp^{80}) in each simulation, and the results are given in Table 4.2. The average C_α-RMSD of the full structure of KCM1 is equal to 2.79 Å, while in KCM2 is only 1.7 Å, which is 1 Å smaller than in KCM1. The difference of the average structure deviation in these two simulations is mainly from the selectivity filter segment. The average C_α-RMSD of the selectivity filter in KCM2 is only 0.66, whereas in KCM1 it goes up to 1.34. It has been suggested that the stability of the selectivity filter structure is crucial to the function of the channel [3, 87, 4]. From the results of this analysis we can say that the structure in simulation KCM2 still remained in a functioning state, whereas in KCM1 the filter structure was deformed during the simulation. The RMSD of the full structure and the filter region in SMD1–6 is about the same value as in KCM2, indicating that the application of external forces didn't induce large structural deviation. The full-structure RMSD in multi-ion SMD simulations (SMD4–6) is slightly higher than in single-ion SMD (SMD1–3), whereas the RMS deviation of the filter region is about the same value, except in SMD2. It indicates that the application of the extra external force has more disturbance on the other part of the channel rather than on the filter region. The larger RMSD of the filter structure in SMD2 comes from a twist of the filter backbone, and details about the structure deviation will be discussed in the next section.

Figure 4.5 shows the time variation of the C_α-RMSD of the full structure and the selectivity filter in simulation KCM1 and KCM2. In KCM1, the total C_α-RMSD rises to 1.50 Å after the first relaxation, and goes up to 2.3 Å before the system reaches the

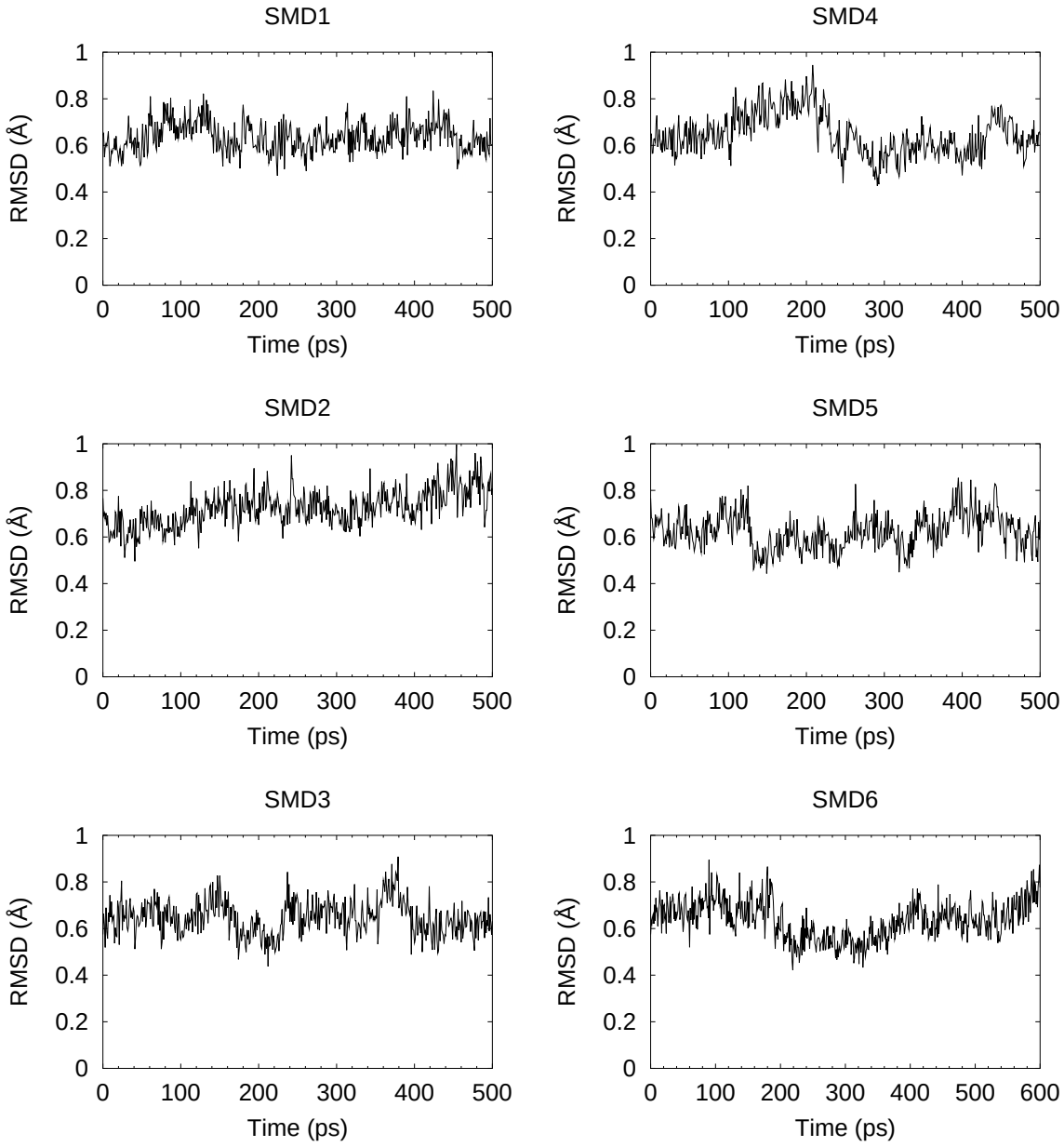

Figure 4.6.: Time variation of the C_α-RMSD of the selectivity filter structure (residues 71-80) in SMD simulations.

equilibrium density. It mainly comes from the adaptation between the channel structure and the membrane/solvent environment at the beginning of the simulation. The increase of the C_α-RMSD of the selectivity filter around $t = 700$ ps in KCM1 is caused by the movement of ion K2 from the selectivity filter into the central cavity. The C_α-RMSD of the filter structure rises from 1.0 Å to 1.2 Å after this movement. A peak of the C_α-RMSD of the selectivity filter appears around $t = 1400$ ps. It is due to water molecules flowing through the narrow filter around this moment.

The time variation of the C_α-RMSD of the selectivity filter in SMD simulations is shown in Fig. 4.6. The peaks of the RMSD in each simulation correspond mainly to the translocation of ions, revealing that the structure of the selectivity filter adjusts itself to various occupancy states during the translocation process. Details of the coupling between the fluctuation of the filter structure and ion movement will be explored by examining the complex hydrogen-bonded network of this region in the next section.

4.5.3. The RMS fluctuation of the KcsA channel structure

Details of the structure deviation are given by the root-mean-square fluctuation (RMSF) of the C_α atom of each residue. The C_α-RMSF in KCM1, 2 and SMD1–6 are shown in Fig. 4.7. The RMS fluctuation is calculated by the optimal transformation method as well. The RMS fluctuation analysis identifies the flexible regions of the channel protein. As expected, the solvent exposed area of the ion channel, which means both N- and C-terminus at the intracellular side, and residue Arg^{52} to Pro^{63} of the P-loop at the extracellular side of each monomer give rise to higher fluctuations in all simulations. And those regions with smaller fluctuations between each peak correspond to the TM1, P-, and the TM2 helices (see Fig. 2.1). In KCM1, only the lower part of the selectivity filter remains stable. The upper part of the filter deviates too much from the initial conformation. A particularly large fluctuation of the filter segment (residue Thr^{72} to Leu^{81}) appears in M4. It stands for a significant deformation of the selectivity filter of M4 induced by the movement of waters. Whereas in KCM2, the structure of the channel remains close to its reference conformation. The upper part of the whole channel, which is buried in the membrane, has a fluctuation less than 1 Å. A small peak appears between the P-helix and TM2 corresponding to the turn connecting these two structural elements. Note that this peak doesn't appear in M4 of KCM2. Instead, the fluctuation of the whole TM1 is larger than other monomers, implying that the motion of one structural element might suppress the movement of the other part of the protein. The average RMS fluctuation in both single-ion and multi-ion SMD simulations are similar as in KCM2, except that the P-loops have larger fluctuation. The application of external forces didn't cause significant structural deviation in the membrane part of the channel in SMD simulations.

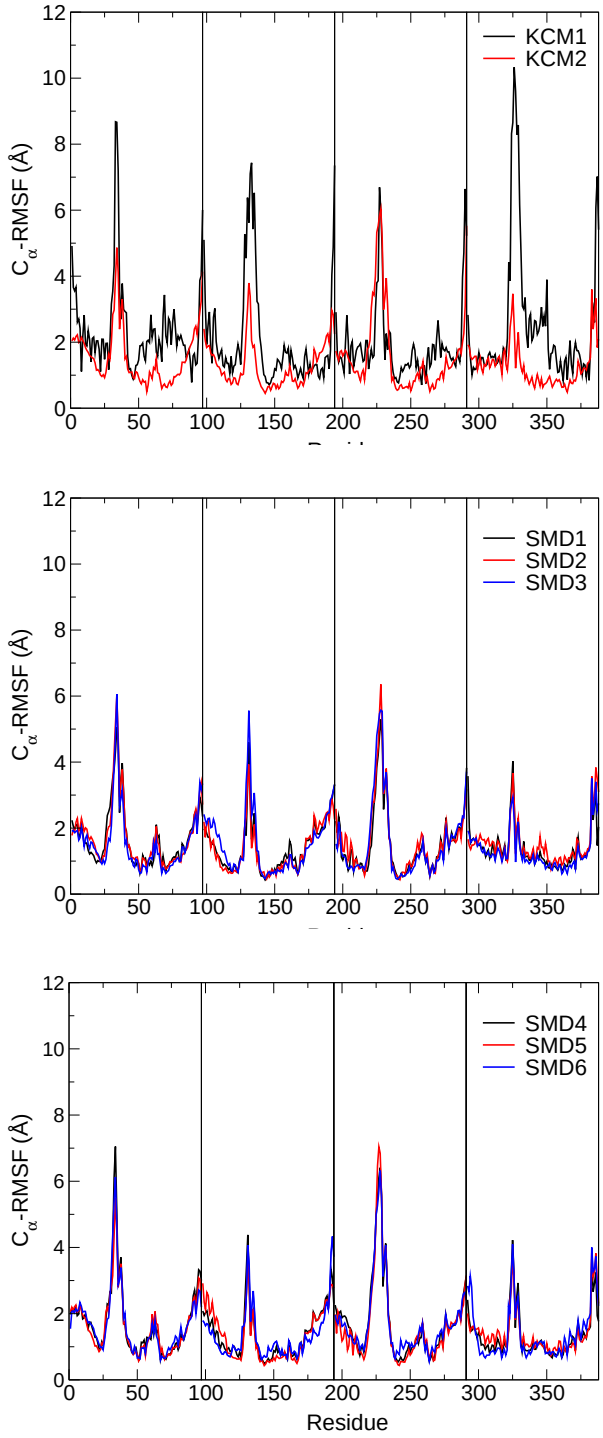

Figure 4.7.: The RMSF of the C_α atoms of the channel protein in simulation KCM1,2 and SMD1–6.

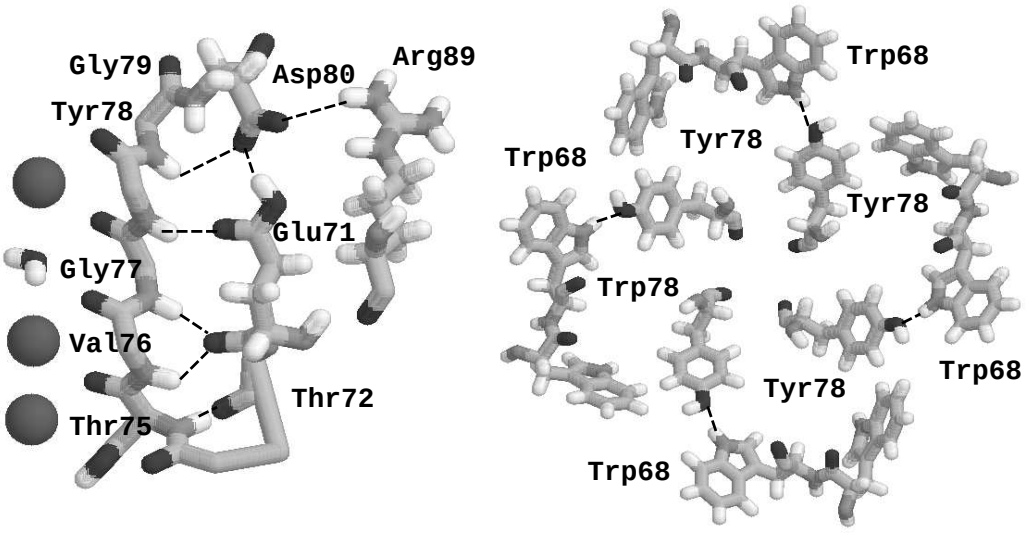

(a) (b)

Figure 4.8.: (a) hydrogen-bonded pair network in the selectivity filter region. The hydrogen bonds between Asp^{80} and Arg^{89} are inter-chain interaction. (b) The inter-chain interaction between aromatic amino acids Tyr^{78} and Trp^{68} viewed from the extracellular side.

4.6. The hydrogen-bonded network of the selectivity filter

The selectivity filter is the most important structural component for the function of a K^+ channel. It is composed of the backbone atoms of the K^+-channel signature sequence 'TVGYG'. Thus, the stability of the structure of the selectivity filter is essential for the function of the KcsA channel [87, 4]. The filter structure is sustained by a complex hydrogen-bonded network at this region, as revealed in the crystallographic data [3, 4]. Fig. 4.8 illustrates some of the possible bonded pairs which are important for sustaining the filter structure. Among them the bonding between the aromatic residues Tyr^{78} and Trp^{68}, and between the charged residues Asp^{80} and Arg^{89} are inter-chain interactions between residues from adjacent monomers. They are located close to the extracellular mouth and contribute to keeping the tetramer structure together. The others are intra-chain interactions. Among them the bonding between the side chains of Glu^{71} and Asp^{80} is the most crucial one to keep the selectivity filter structure. When the side chains of these two residues are properly located and bond with each other, the filter loops will be held in shape, and other intra-chain bonded pairs, the Glu^{71}O-Val^{76}HN and Thr^{72}O-Thr^{75}HN pairs at the lower part, the Glu^{71}OE1-Tyr^{78}HN pairs at the middle, and the Gly^{79}HN-Asp^{80}OD pairs at the upper part of the selectivity filter will be stabilized.

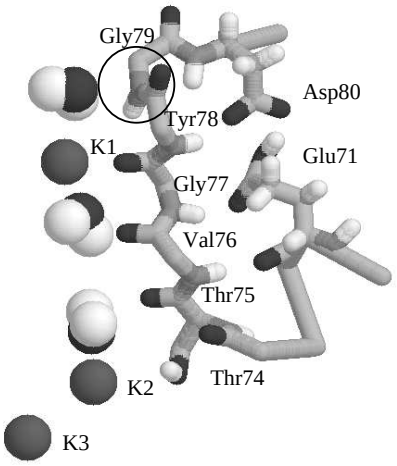

Figure 4.9.: In KCM1, the backbone amide group of Gly^{79} twisted and bind with the water located at the extracellular mouth during the simulation.

4.6.1. The hydrogen-bonded network in MD simulations

The stability of this hydrogen-bonded network in the MD simulations is presented by the average distances between each bonded pair. The average distance of those bonded pairs illustrated in Fig. 4.8 are given in Table 4.3. The pair distances of the crystallographic structure in PDB file 1BL8 and 1K4C are given for comparison. The coordinates of the side chain of Glu^{71} are missing in PDB file 1BL8; therefore, the distance between Glu^{71}HE1 and Asp^{80}OD and between Glu^{71}OE1 and Tyr^{78}HN are not given. For those bonded pairs involving the carboxylate oxygens of Asp^{80} and the amide hydrogens of Arg^{89}, only the nearest pairs are taken into account.

The data shows that in KCM1, only the lower part of the selectivity filter remained stable, consistent with the RMSF analysis. The average bonding distances of pair Thr^{72}O-Thr^{75}HN and Glu^{71}O-V^{76}HN are close to the crystallographic data with only small fluctuations. Except in monomer M3, the hydrogen bond between the carboxylate groups of Glu^{71} and Asp^{80} were not formed during the simulation. Without the supporting of this carboxyl-carboxylate bonding, the backbone atoms of the upper part of the filter altered their orientation during the simulation. The carbonyl oxygen of Val^{76} of M2 twisted inward, and the amide hydrogen of it turned towards the pore axis. Similar alteration occurred to Gly^{79} at the extracellular mouth of the filter in M1, M3, and M4. The amide hydrogens of Gly^{79} turned outward pointing towards the adjacent monomer, and bind to water molecules entering from the extracellular mouth, as shown in Fig. 4.9.

In KCM2, the hydrogen-bonded network of the selectivity filter shows good agreement to the crystallographic data. The bonding between the carboxylate groups of Glu^{71} and

Pair	1BL8	KCM1	1K4C	KCM2
Tyr^{78}OH-Trp^{68}NE1	2.71	3.87±0.77	3.40	2.81±0.22
	2.74	4.03±0.46	3.46	2.90±0.27
	2.63	5.27±1.65	3.51	2.83±0.22
	2.69	2.96±0.34	3.46	3.07±0.37
Asp^{80}OD-Arg^{89}NH	4.23	3.66±2.06	3.95	2.61±0.95
	4.26	4.92±0.87	4.00	3.68±0.36
	4.08	9.15±1.20	4.02	3.53±0.50
	4.19	8.14±1.72	4.10	4.15±0.55
Glu^{71}HE1-Asp^{80}OD	-	5.59±1.46	1.70	1.74±0.09
	-	3.48±1.67	1.70	1.72±0.08
	-	1.74±0.09	1.70	1.73±0.08
	-	4.29±1.66	1.70	1.74±0.10
Thr^{72}O-Thr^{75}HN	1.91	2.22±0.31	2.11	2.12±0.24
	1.91	2.12±0.24	2.11	2.12±0.25
	1.90	2.10±0.23	2.11	2.14±0.25
	1.91	2.16±0.29	2.11	2.13±0.24
Glu^{71}O-Val^{76}HN	2.22	1.97±0.17	2.33	2.21±0.24
	2.23	1.98±0.16	2.34	2.00±0.16
	2.23	2.23±0.31	2.33	2.07±0.19
	2.23	2.06±0.22	2.33	1.99±0.15
Glu^{71}O-Gly^{77}HN	3.25	2.66±0.66	2.01	3.40±0.51
	3.25	5.17±0.90	2.02	2.85±0.44
	3.25	3.67±0.51	2.01	2.92±0.45
	3.25	2.85±0.64	2.01	2.51±0.42
Glu^{71}OE1-Tyr^{78}HN	-	3.10±1.12	2.12	2.23±0.66
	-	3.77±0.98	2.12	1.99±0.18
	-	3.42±0.75	2.12	2.01±0.21
	-	2.21±0.59	2.12	2.01±0.35
Gly^{79}HN-Asp^{80}OD	3.93	5.69±1.21	3.41	3.76±0.27
	3.93	5.38±1.43	3.41	3.69±0.29
	3.93	3.76±0.60	3.41	3.77±0.34
	3.94	7.03±0.45	3.41	3.59±0.28

Table 4.3.: Average distances of bonded pairs in the hydrogen-bonded network in KCM1 and KCM2. The distances of the corresponding pairs in the crystallographic data in file 1BL8 and 1K4C are given as references. The first two pairs are inter-chain interaction between residues from adjacent monomers. For each pair the first row corresponds to bonded pair of monomer (1,2), the second row to (2,3), the third row to (3,4), and the fourth row to (4,1). The rest are intra-chain pairs in the four monomers.

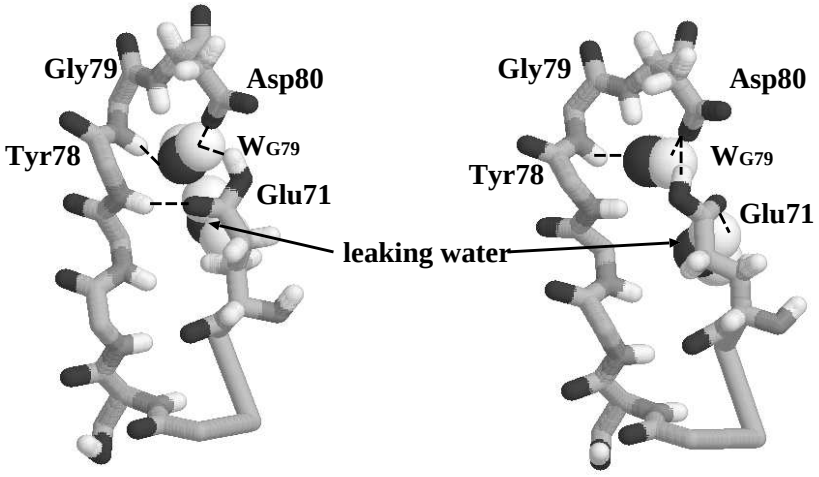

Figure 4.10.: The location of water molecule W_{G79}. It mediates the bonding between Glu^{71}OE1 and Tyr^{78}HN. Two alternative conformations of the side chain of Glu^{71} in KCM2 are presented here. The switching-motion of the side chain is induced by a water molecule leaking into the core part of the protein.

Asp^{80} was very stable with fluctuation less than 0.1 Å in all monomers. This aided to stabilize other bonded pairs along the side chains of Glu^{71} and Asp^{80}. At the extracellular mouth, the average distance between the bonded pair Gly^{79} and Asp^{80} of the selectivity filter was longer than a typical hydrogen bonded in all monomers, whereas the fluctuation was small. Actually, the amide hydrogen of Gly^{79} and the carboxylate oxygen of Asp^{80} were not bonded with each other directly, but mediated by a water molecule. This has been observed in the crystallographic data released in 2001 (PDB file 1K4C), in which the coordinates of a water oxygen sitting between Gly^{79} and Asp^{80} was resolved [4]. The oxygen of the water molecule forms hydrogen bond with the amide hydrogen of Gly^{79}, and its hydrogen (not presented in experimental data) atoms are supposed to bond to the carboxylate oxygens of Asp^{80} and Glu^{71}. We didn't insert any water molecule at this location when constructing the model. Instead, water molecules leaked into the structure themselves during the simulation, and sat at the position exactly as predicted in the crystallographic data. Here we denote this water molecule by W_{G79}. The position of water W_{G79} is as shown in Fig. 4.10. The average distances between W_{G79} and the surrounding residue atoms in each monomer are given in Table 4.4. This water-mediated bonded network was very stable during the 1 ns simulation.

For the pair distance of Glu^{71}OE1-Tyr^{78}HN, a relatively large fluctuation appeared to the pair in M1. By examining the time variation of the bonded distance, a "switching motion" of this bonded pair was observed, as shown in Fig. 4.11. The "switching motion" was due to the side chain of Glu^{71} switching between its alternative conformations. The

Pair	1K4C	KCM2
$Glu^{71}OE$-W_{G79}	1.80	2.83±0.43
	1.80	2.67±0.38
	1.80	2.64±0.38
	1.80	2.72±0.40
$Gly^{79}HN$-W_{G79}	1.88	1.99±0.21
	1.88	1.98±0.15
	1.88	1.96±0.13
	1.88	1.98±0.15
$Asp^{80}OD$-W_{G79}	2.20	1.84±0.17
	2.20	1.90±0.23
	2.20	1.93±0.31
	2.20	1.89±0.23

Table 4.4.: Average distance between water W_{G79} and the surrounded residue atoms in the four monomers of KCM2, comparing with the crystallographic data.

carboxylate end of the side chain adopted different dihedral angles, as illustrated in Fig. 4.10. By closely checking the details of different configurations, we observed that such "switching motion" was induced by a water molecule leaking into the core part of the filter. The carboxylate oxygen switching between bonding with the amide group of Tyr^{78} or with the leaking water molecule (see Fig. 4.10). The time variation of the number of water surrounding the $Glu^{71}OE1$ is shown in Fig. 4.12. The carboxylate of Glu^{71} stably bonded with W_{G79} in every monomer. And in M1 and M4, the $Glu^{71}OE1$ have contact with another water molecule once in a while. Comparing the variation of the data shown in Fig. 4.11 and Fig. 4.12, we found that the fluctuation of the pair distance of $Glu^{71}OE1$-$Tyr^{78}HN$ is related to the variation of the number of surrounding water.

4.6.2. The hydrogen-bonded network in SMD simulations

The average pair distances of those bonded pairs shown in Fig. 4.8 in SMD1–6 are given in Table 4.5 and Table 4.6. As shown in the tables, both inter-chain pairs, the average distance between the aromatic residues Tyr^{78} and Trp^{68} and between the charged residues Asp^{80} and Arg^{89} in the SMD simulations stay stably within the range of the original distances given in the crystallographic structure. The $Glu^{71}HE1$-$Asp^{80}OD$ pair distances are very stable in all SMD simulations, except in monomer M4 of SMD2 and SMD5. The average pair distances remain close to the crystallographic data with fluctuations less than 0.1 Å. The stability of the carboxyl-carboxylate bond stabilized other surrounded intra-chain bondings. Same as in KCM2, the pair distances of $Gly^{79}HN$–$Asp^{80}OD$ are long but the fluctuations are relatively small in most of the SMD simulations. The

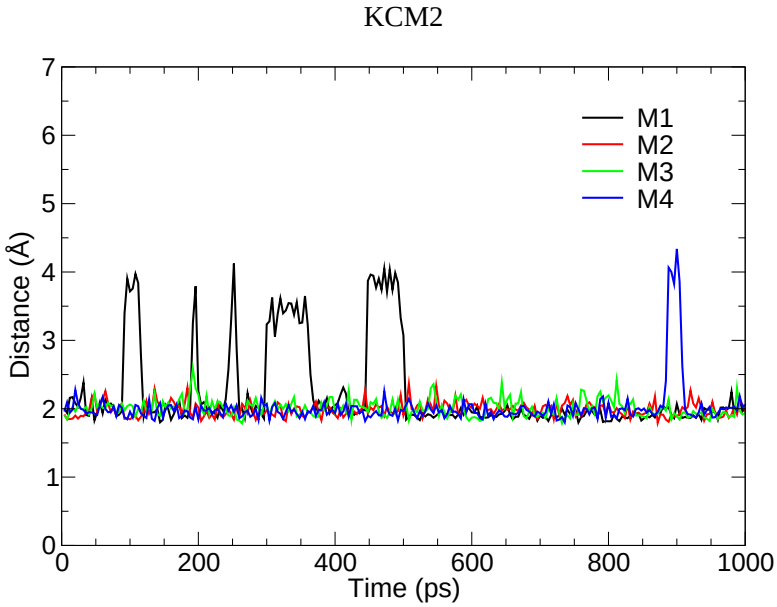

Figure 4.11.: Time variation of the pair distance of Glu^{71}HE1-Tyr^{78}OD in the four monomers of KCM2. The pair distance switches between two alternative values in monomer M1 and M4.

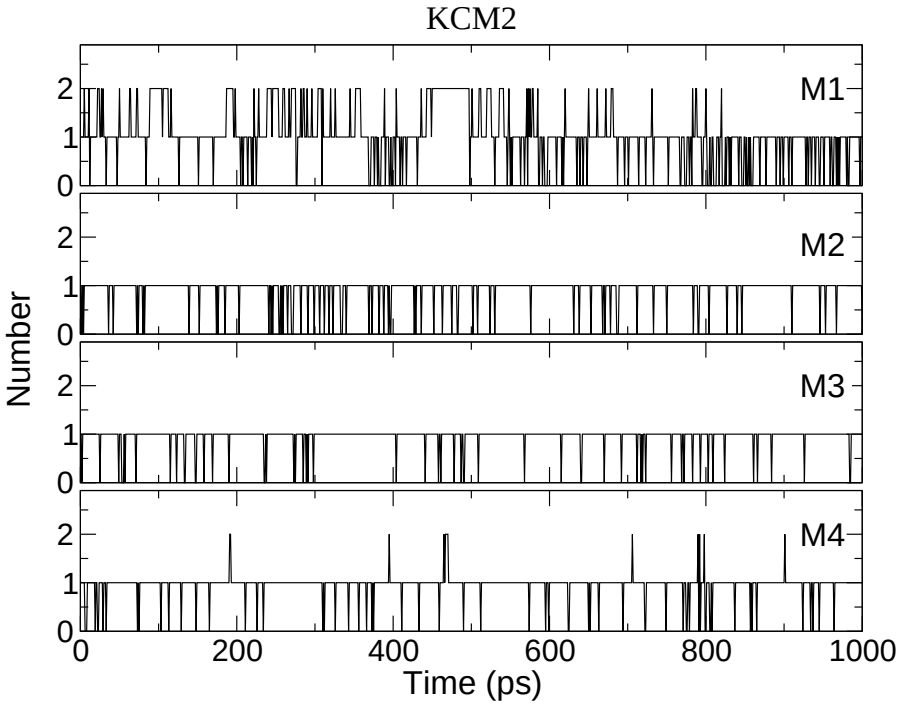

Figure 4.12.: Time variation of the number of water surrounding the carboxylate oxygen of Glu^{71} of the four monomers in KCM2.

Pair	1K4C	SMD1	SMD2	SMD3
$Tyr^{78}OH$-$Trp^{68}NE1$	3.40	2.76±0.18	2.78±0.19	2.80±0.23
	3.46	2.92±0.30	2.81±0.21	2.89±0.27
	3.51	2.81±0.23	2.79±0.22	2.80±0.20
	3.46	3.58±0.52	3.77±0.62	3.26±0.42
$Asp^{80}OD$-$Arg^{89}NH$	3.95	1.84±0.33	1.91±0.41	2.60±0.96
	4.00	3.55±0.57	2.34±0.79	3.22±0.76
	4.02	3.56±0.32	3.47±0.38	3.53±0.38
	4.10	4.56±0.56	5.23±1.26	4.45±0.57
$Glu^{71}HE1$-$Asp^{80}OD$	1.70	1.72±0.08	1.73±0.08	1.73±0.08
	1.70	1.73±0.09	1.72±0.08	1.73±0.14
	1.70	1.72±0.08	1.71±0.08	1.72±0.08
	1.70	1.74±0.10	3.48±1.72	1.75±0.09
$Thr^{72}O$-$Thr^{75}HN$	2.11	2.13±0.22	2.05±0.20	2.11±0.24
	2.11	2.08±0.21	2.09±0.25	2.06±0.21
	2.11	2.17±0.26	2.15±0.27	2.15±0.30
	2.11	2.09±0.23	2.11±0.23	2.28±0.50
$Glu^{71}O$-$Val^{76}HN$	2.33	2.20±0.20	2.16±0.20	2.20±0.23
	2.34	2.06±0.19	2.08±0.20	2.09±0.20
	2.33	2.04±0.20	2.20±0.29	2.08±0.21
	2.33	1.98±0.16	2.07±0.20	2.17±0.34
$Glu^{71}O$-$Gly^{77}HN$	2.01	3.70±0.37	3.66±0.43	3.61±0.45
	2.02	2.95±0.45	3.11±0.54	2.91±0.47
	2.01	2.72±0.42	2.80±0.50	2.69±0.45
	2.01	2.85±0.48	4.79±1.18	2.74±0.59
$Glu^{71}OE1$-$Tyr^{78}HN$	2.12	2.72±1.05	2.30±0.72	2.02±0.29
	2.12	1.99±0.22	1.97±0.17	2.03±0.29
	2.12	2.10±0.30	1.99±0.21	2.02±0.21
	2.12	2.25±0.77	4.00±1.41	2.92±1.10
$Gly^{79}HN$-$Asp^{80}OD$	3.41	3.82±0.26	3.78±0.27	3.81±0.29
	3.41	3.82±0.30	3.70±0.29	4.06±0.86
	3.41	3.74±0.29	3.81±0.31	3.76±0.28
	3.41	3.70±0.30	4.97±1.72	3.71±0.32

Table 4.5.: Average distance of bonded pairs in the hydrogen-bonded network in SMD1–3. The first two pairs are inter-chain interaction between adjacent monomers, where the first row corresponds to bonded pair of monomer (1,2), the second row to (2,3), the third row to (3,4), and the fourth row to (4,1). The other pairs are intra-chain interaction.

Pair	1K4C	SMD4	SMD5	SMD6
$Tyr^{78}OH$-$Trp^{68}NE1$	3.40	2.76±0.20	2.77±0.19	2.77±0.20
	3.46	2.93±0.31	2.91±0.31	3.05±0.51
	3.51	2.81±0.21	2.82±0.22	2.85±0.25
	3.46	3.03±0.34	3.24±0.48	3.22±0.53
$Asp^{80}OD$-$Arg^{89}NH$	3.95	2.30±0.77	2.63±0.86	2.56±0.95
	4.00	3.25±0.65	3.40±0.56	4.49±0.79
	4.02	3.51±0.63	3.49±0.64	3.59±0.45
	4.10	4.42±0.64	4.73±0.96	4.11±0.53
$Glu^{71}HE1$-$Asp^{80}OD$	1.70	1.73±0.09	1.75±0.09	1.74±0.09
	1.70	1.73±0.08	1.73±0.08	1.75±0.11
	1.70	1.73±0.08	1.73±0.09	1.77±0.28
	1.70	1.74±0.09	2.51±1.55	1.77±0.12
$Thr^{72}O$-$Thr^{75}HN$	2.11	2.06±0.20	2.09±0.21	2.15±0.27
	2.11	2.05±0.18	2.04±0.18	2.12±0.26
	2.11	2.13±0.25	2.10±0.21	2.25±0.33
	2.11	2.17±0.27	2.12±0.25	2.03±0.18
$Glu^{71}O$-$Val^{76}HN$	2.33	2.16±0.19	2.10±0.20	2.13±0.20
	2.34	2.04±0.17	2.06±0.20	2.03±0.18
	2.33	2.13±0.22	2.06±0.22	2.26±0.28
	2.33	2.22±0.40	2.20±0.29	1.99±0.16
$Glu^{71}O$-$Gly^{77}HN$	2.01	3.60±0.42	3.55±0.49	3.30±0.48
	2.02	2.92±0.63	2.86±0.49	2.82±0.51
	2.01	3.01±0.53	2.70±0.44	2.85±0.44
	2.01	2.84±0.51	2.67±0.53	2.34±0.41
$Glu^{71}OE1$-$Tyr^{78}HN$	2.12	2.16±0.54	2.64±0.86	2.28±0.72
	2.12	2.01±0.23	1.97±0.18	2.21±0.56
	2.12	2.00±0.23	2.03±0.25	3.08±0.71
	2.12	2.17±0.50	3.15±1.05	2.32±0.40
$Gly^{79}HN$-$Asp^{80}OD$	3.41	3.88±0.46	3.77±0.33	3.76±0.28
	3.41	3.70±0.29	3.71±0.31	3.72±0.27
	3.41	3.73±0.29	3.70±0.31	5.51±1.15
	3.41	3.63±0.29	5.32±1.43	5.09±1.26

Table 4.6.: Average distance of bonded pairs in the hydrogen-bonded network in SMD4–6. The first two pairs are inter-chain interaction between adjacent monomers, where the first row corresponds to bonded pair of monomer (1,2), the second row to (2,3), the third row to (3,4), and the fourth row to (4,1). The other pairs are intra-chain interaction.

Pair	1K4C	SMD1	SMD2	SMD3
$Glu^{71}OE\text{-}W_{G79}$	1.80	2.52±0.35	2.57±0.39	2.57±0.37
	1.80	2.52±0.35	2.69±0.37	2.50±0.42
	1.80	2.53±0.41	2.65±0.45	2.56±0.39
	1.80	2.76±0.57	3.72±1.01	3.17±0.59
$Gly^{79}HN\text{-}W_{G79}$	1.88	1.95±0.18	2.03±0.27	2.12±0.30
	1.88	1.98±0.14	1.99±0.15	2.01±0.19
	1.88	1.94±0.12	2.12±0.55	1.95±0.13
	1.88	1.99±0.15	2.41±0.90	2.02±0.18
$Asp^{80}OD\text{-}W_{G79}$	2.20	1.89±0.23	1.95±0.32	1.91±0.24
	2.20	1.94±0.24	1.88±0.20	2.20±0.80
	2.20	2.03±0.33	1.97±0.29	2.01±0.31
	2.20	1.90±0.22	3.28±1.93	1.89±0.26

Table 4.7.: Average distance between water W_{G79} and the surrounded residue atoms in the four monomers of SMD1–3, comparing with the crystallographic data.

Pair	1K4C	SMD4	SMD5	SMD6
$Glu^{71}OE\text{-}W_{G79}$	1.80	2.53±0.38	2.35±0.00	2.56±0.40
	1.80	2.64±0.35	2.61±0.35	2.75±0.42
	1.80	2.53±0.38	2.57±0.38	2.07±0.38
	1.80	2.77±0.41	2.63±0.84	2.24±0.44
$Gly^{79}HN\text{-}W_{G79}$	1.88	1.99±0.19	2.12±0.00	2.05±0.29
	1.88	1.99±0.15	2.00±0.16	2.03±0.19
	1.88	1.93±0.13	1.94±0.14	1.99±0.16
	1.88	1.98±0.16	2.12±0.31	2.05±0.21
$Asp^{80}OD\text{-}W_{G79}$	2.20	1.95±0.43	1.85±0.00	1.86±0.20
	2.20	1.90±0.23	1.89±0.22	1.88±0.19
	2.20	1.92±0.23	1.94±0.25	3.74±1.09
	2.20	1.87±0.21	3.61±1.68	3.35±1.17

Table 4.8.: Average distance between water W_{G79} and the surrounded residue atoms in the four monomers of SMD4–6, comparing with the crystallographic data.

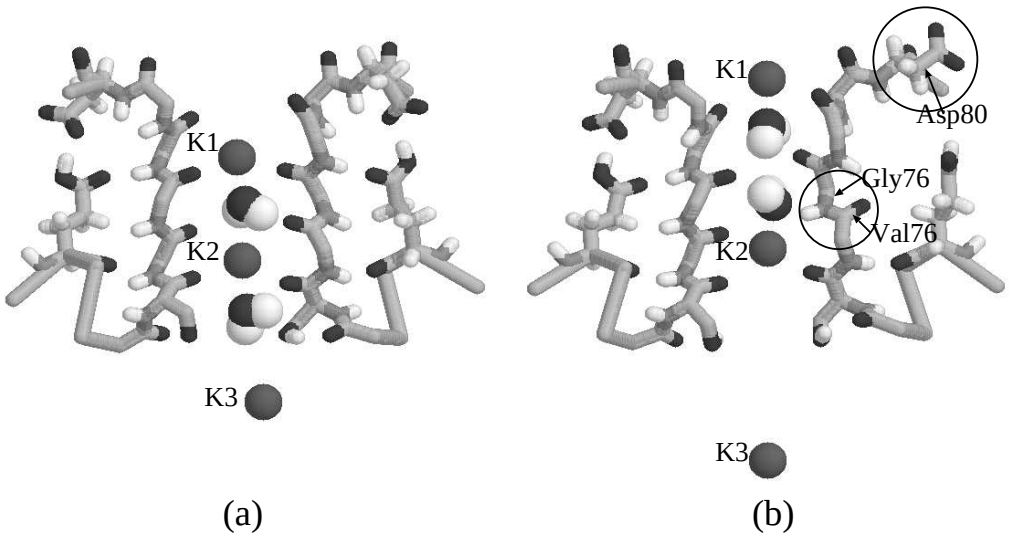

Figure 4.13.: The alternative conformations of the selectivity filter in SMD2. (a) the initial conformation of the selectivity filter. Only monomer M2 and M4 are shown here. (b) the alteration of the selectivity filter conformation. The amide hydrogen of Gly^{77} in M4 turns towards the pore axis and bound with a water molecule. And the side chain of Asp^{80} changes its orientation and the binding between Glu^{71} and Asp^{80} is broken up.

bonding was mediated by a water molecule (W_{G79}) as well in all simulations. The average distances between W_{G79} and the surrounding residue atoms in SMD1–6 are given in Table 4.7 and Table 4.8. Similar switching motion of the side chain of Glu^{71} occurred almost in every SMD simulation. It was mainly induced by water molecules leaking into the protein structure, as illustrated in Fig. 4.10.

In SMD2, the average distance of pair Glu^{71}HE1-Asp^{80}OD in M4 is long compared to other monomers. It was the result of a series of breakage of several bonded pairs. The backbone of Val^{76}-Gly^{77} peptide of M4 adopted a different conformation during the simulation. Instead of pointing towards the pore axis, the carbonyl oxygen of Val^{76} altered its orientation and pointed away from the pore center, which caused the neighboring amide hydrogen of Gly^{77} to point towards the pore, as shown in Fig. 4.13. Similar alteration of the backbone of the filter residues has been observed in the crystallographic structure under low salt concentration resolved by Zhou et al. [4]. In their experiments, because of the low salt concentration environment, the average ion occupancy number in the selectivity filter was lower. Therefore, the backbone of the filter adopted itself to an alternative conformation, in which the carbonyl oxygens of Val^{76} pointed away from the pore axis and bonded to a water leaking into the core part of the protein. The alternative filter structure corresponds to a 'non-conductive' state of the KcsA channel. And in SMD2, the amide hydrogen of Gly^{77} and the oxygen of water W1 formed a stable hydrogen bond and blocked the selectivity filter. The alteration of the backbone structure

in SMD2 was induced by water molecule W1. Details of the dynamics of ions and waters will be discussed in the next chapter. The twisting of Val^{76}-Gly^{77} backbone destabilized the filter structure in M4. It induced a breakage of the bonding of Glu^{71}OE-Tyr^{78}NH and Gly^{79}HN-Asp^{80}OD, which resulted to a further breakage of Glu^{71}HE1-Asp^{80}OD bond. The same story also occurred to the channel protein in SMD5. The twisting of the Val^{76}-Gly^{77} backbone induced the breakage of Glu^{71}HE1-Asp^{80}OD bond in M4 during the simulation.

The average pair distances and fluctuation of Gly^{79}HN-Asp^{80}OD of M4 in SMD2, SMD5, and SMD6 are larger. The side chain of Asp^{80} of M4 dislocates from its initial position, as shown in Fig. 4.13. The dihedral angle between the side chain and the backbone of Asp^{80} altered to a different value. The carboxylate of the side chain pointed towards the neighboring monomer instead of pointing downward. Because of the strong binding between the carboxylate groups of Asp^{80} and Glu^{71}, the side chain of Glu^{71} also altered its conformation and moved with the side chain of Asp^{80}. The binding of Glu^{71}HE1-Asp^{80}OD in M4 was broken up finally when K1 exited from site S_0 to extracellular mouth. The alteration the side chain of Asp^{80} made it detached from the amide hydrogen of Gly^{79}/W_{G79}, and hence gave a large fluctuation to the average pair distance. The same condition appeared in the M3 and M4 in SMD6 as well.

4.7. Summary

In this chapter, I have introduced the channel-membrane system for our MD/SMD simulations. The variation of the structural properties of the KcsA channel through the simulation processes was first examined. From various structure analyses, we have the following conclusions:

1. The structure of the selectivity filter is sustained by the hydrogen-bonded network.

   The selectivity filter structure is sustained by a delicate hydrogen-bonded network in the core part (see Fig. 4.8), as revealed in the crystallographic data [3, 4]. Among them, the most essential one is the bonding between side chains of Glu^{71} and Arg^{80}. If the side chains of these two residues form stable hydrogen bond, other hydrogen bonds in the network, including the water molecules leaking into the core part of the filter (Fig. 4.10), will be stabilized, such as in simulation KCM2 and SMDs; on the contrary, if Glu^{71}-Arg^{80} bonds are broken, the selectivity filter structure will be deformed, as in simulation KCM1.

2. The selectivity filter is very rigid.

   If the hydrogen-bonded network is well sustained, the structure of the selectivity filter is very rigid. Both the RMSD and RMSF analyses show that the selectivity filter has a lower average fluctuation than other parts of the channel.

3. The stability of the KcsA channel relies on the stability of the selectivity filter.

   The stability of the selectivity filter is crucial to the stability of the whole channel structure. In KCM1, because the selectivity filter was deformed, the RMSD of the whole channel went beyond 3 Å, which is 1 Å more than in other simulations.

4. The occupancy state in the selectivity filter is important to the stability of the filter structure.

   The occupancy state in the selectivity filter plays an role in the stability of the filter structure as well. It may cause the deformation of the selectivity filter if the ion occupancy number is too low. There must always be at least two K^+ in the selectivity filter to keep the filter in a functional structure. Our simulations were actually carried out in a low salt concentration environment, which usually results in a low ion occupancy state in experiments. The crystallographic structure prepared in low salt concentration shows a twist of the backbone of the selectivity filter. In simulation SMD2, the same deformation on the selectivity filter appears, whereas in multi-ion SMD simulations, no such deformation was found, even if the hydrogen bonds of Glu^{71}-Arg^{80} were broken off, because the selectivity filter was enforced to be in a high occupancy state through the whole simulation in this scheme.

5. The ion permeation mechanism in the KcsA channel

The structural properties of the model K^+ channel in the simulations have been presented in the last chapter. In this chapter, I am going to present the dynamical part of the simulation results.

The long-range electrostatic interaction is considered the most dominant term in many biophysical reactions. In K^+ channels, ions are supposed to permeate through the channel pore in a multi-ion fashion. Intuitively, one would think that the efficiency of multi-ion conduction is because the electrostatic repulsion between ions effectively reduce the energy barrier on the permeation pathway. But a simple view like this is not sufficient to describe the concerted movement of ions in a multi-ion permeation process. Such a movement requires a delicate energy balance between all interaction groups, including ions, waters, and the residue atoms along the channel pore. In our SMD simulations, we observed concerted movements of potassium ions and water molecules. Analyzing the interactions involving in this kind of movements may tell us the actual molecular mechanism of the multi-ion conduction in K^+ channels.

5.1. The multi-ion permeation mechanism

The multi-ion mechanism was first proposed by A. Hodgkin and R. Keynes in 1955 in their studies of the movement of potassium ions across the squid giant axon membrane [2]. By using the radioactive potassium ions, they were able to measure the ion flux at different applied membrane potentials. According to the assumption of independent movement of permeating ions, the ratio between the efflux J_o and the influx J_i of ion X is given by [1]

$$\frac{J_o}{J_i} = exp[\frac{(E - E_X)zF}{RT}], \tag{5.1}$$

where z is the charge number of the ion (e.g. $z = +1$ for K^+), F is the Faraday constant (96 500 C mol^{-1}), $(E - E_X)$ is the difference between the applied voltage and the equilibrium potential of ion X. By taking logarithm of both sides of Eq. (5.1), one obtains

$$ln\frac{J_o}{J_i} = \frac{(E - E_X)zF}{RT}, \tag{5.2}$$

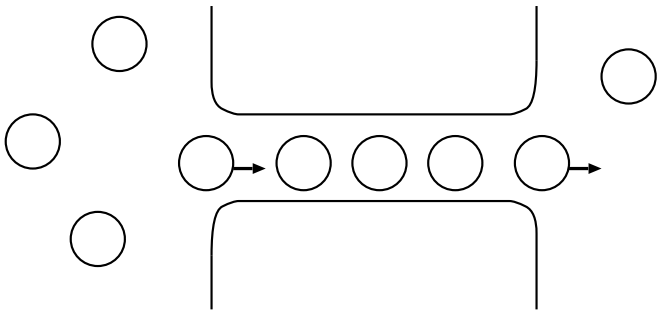

Figure 5.1.: A schematic picture of the multi-ion mechanism: permeating ions line up in the narrow pore; an ion entering the channel from the left side pushes the ion at the right end to escape from the channel.

that is, the logarithm of the flux ratio should be proportional to $(E - E_X)$ under the assumption of the independence of diffusion ions. However, the experimental result of Hodgkin and Keynes was 2∼3 fold steeper than predicted by the equation above. They found that the data was fitted better by adding a factor n to the exponent in Eq. (5.1):

$$\frac{J_o}{J_i} = exp[\frac{n(E - E_K)zF}{RT}], \tag{5.3}$$

with $n = 2.5$ in their original experiments. The factor n in this modified equation can be explained by a complex containing n ions moving through the channel pore as an integral, i.e., in a "multi-ion" fashion. To achieve a high conduction rate for a potassium channel, they suggested that ions should move one after another successively in a single file through the channel pore. An ion entering one end of the channel pore knocks out the ion at the other end, as illustrated in Fig. 5.1. In this case, the channel pore must be long and narrow. Therefore, the multi-ion permeation mechanism is also known as "the long-pore effect". This was actually the first time the idea of a **channel** appeared.

The theory of multi-ion transportation in potassium channels has been proposed for decades, but its molecular mechanism remains unknown. The determination of the crystallographic structure of the KcsA channel in 1998 provides a possibility to explore the permeation process at the microscopic level. Based on the structure of the KcsA channel, several theoretical calculations about the ion permeation process have been performed [14, 15, 16, 88, 89, 90]. Some calculations have shown that a multi-ion conduction is energetically more favored. For example, by using the FEP (free energy perturbation) methods, J. Åqvist and V. Luzhkov observed that the most favored conduction pathway involves the transition only between the (K-W-K-W) state and the (W-K-W-K) state in the selectivity filter with a free energy difference of 5 kcal mol^{-1} [89]. And the calculation of the free energy profile shows that the activation barrier for this transition is 6 kcal mol^{-1}. Similar results were obtained by S. Bernèche and B. Roux. They have performed calculations for the free energy profile of a multi-ion conduction process using

the umbrella sampling simulations [91]. The most favored ion conduction pathway they found was in agreement with the FEP calculations. And the highest free energy barrier of this conduction pathway is only around 2–3 kcal mol^{-1}. In both calculations, the (W-K-W-K) state was found energetically more stable than the other one.

In the study of Bernèche and Roux, they observed that the energy barrier for an ion at the outermost binding site to exit to the extracellular space decreased progressively when other K^+ in the channel pore approached it. They showed that basically a multi-ion conduction of K^+ can be a barrierless process. The ion-ion repulsion is essential for a fast ion conduction process, yet it seemed to act only at very short range. This conclusion looks peculiar, while the results of our SMD simulations may may provide a possible explanation to it. This will be discussed in section 5.3.

5.2. Ion dynamics in the simulations

In this section, I am going to show the dynamics of K^+ and water in MD and SMD simulations of the model KcsA channels. As introduced previously, in the selectivity filter there are 4+1 ion binding sites, denoted by S_1 to S_4 for the four binding sites in the filter, and S_0 for the one at the extracellular mouth (see Fig. 4.1). For simplicity, a binary code is used to represent the occupancy state of the selectivity filter, where '1' denotes a K^+, '0' denotes a water molecule, and an extra notation 'x' for an empty binding site. The occupancy state of the selectivity filter is represented by the binary code in a bracket '( )' on the sequence from S_0 to S_4. All of our simulations started with the occupancy state (01010).

5.2.1. Dynamics of K^+ and water in MD simulations

As described in the structural analysis in the last chapter, there is a significant structural difference in the selectivity filter region between simulation KCM1 and KCM2. So is the dynamics of K^+ appeared in the two simulations. The trajectories of the three potassium ions and some selected water molecules along the z-axis in simulation KCM1 and KCM2 are shown in Fig. 5.2, comparing with the average positions of the backbone carbonyl oxygens of residue TTVGYG (residue 74–79). All trajectories shown in this section were normalized by taking the center of mass of the KcsA channel as the origin. It is clearly shown in the figures that the dynamics of K^+ and waters in the selectivity filter in KCM2 are more stable than in KCM1.

The initial configuration of the three K^+ of the simulations are as shown in Fig. 4.1: K1 and K2 were located in site S_2 and S_4 respectively in the selectivity filter, and K3 was in the water cavity close to the inner entryway of the filter. In KCM1, only ion K1 remained in the selectivity filter through the 2 ns simulation. Ion K2 moved downward into the water cavity at 700 ps. It was due to the deformation of the selectivity filter. At 200 ps the backbone of Val^{76}-Gly^{77} of monomer M2 twisted and the inner entryway of the

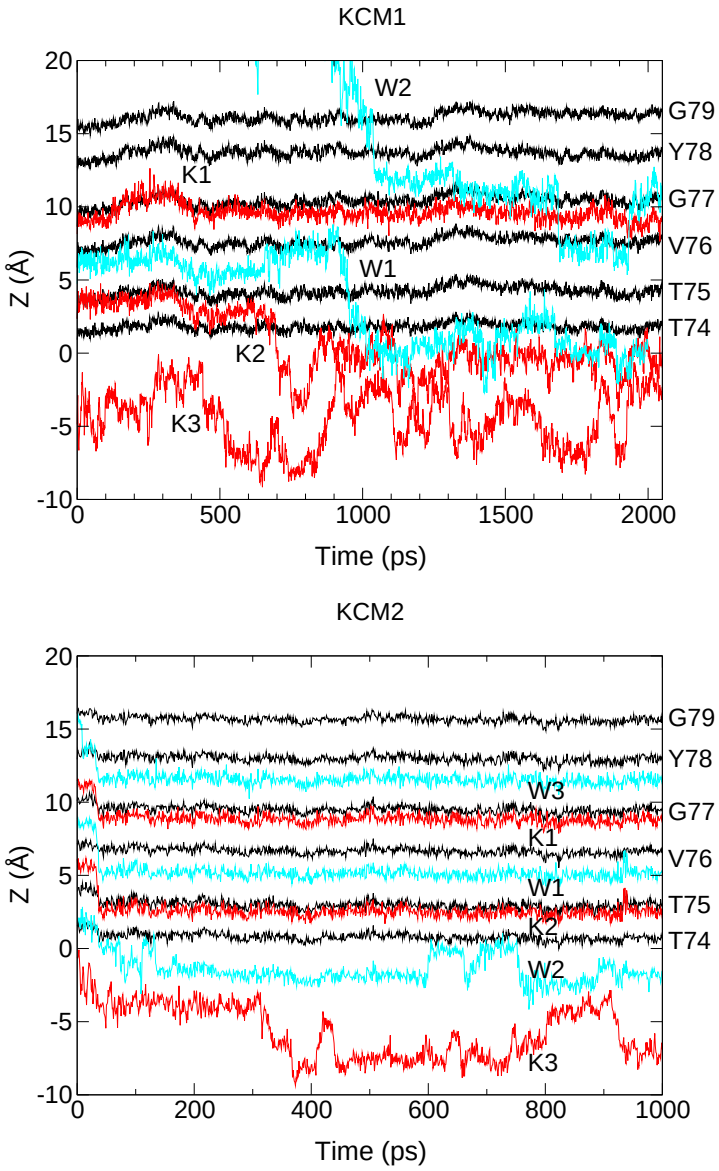

Figure 5.2.: Ion dynamics in simulation KCM1 and KCM2. The z-trajectories of potassium ions K1, K2, K3 (red), some selected water molecules (cyan), and the carbonyl oxygens of the selectivity filter residues T-T-V-G-Y-G (black) are shown. All trajectories were normalized by taking the center of mass of the KcsA channel as the origin. The positions of carbonyl oxygens were averaged over the four monomers. In KCM1, K2 and W1 move downward into the central cavity at 700 ps and 950 ps respectively. At 1000 ps W2 from the extracellular side enters the selectivity filter. It moves downward from site S_1 to S_3 across K1 at 1700 ps, and then moves upward again to site S_1 at 1900 ps. In KCM2, a "concerted movement" occurs between 30∼40 ps, where W3, K1, W1, K2, and W2 translocate concertedly downward to the next binding sites. The occupancy state in the selectivity filter transfers from (01010) to (00101) and remains in this state in the rest of the simulation.

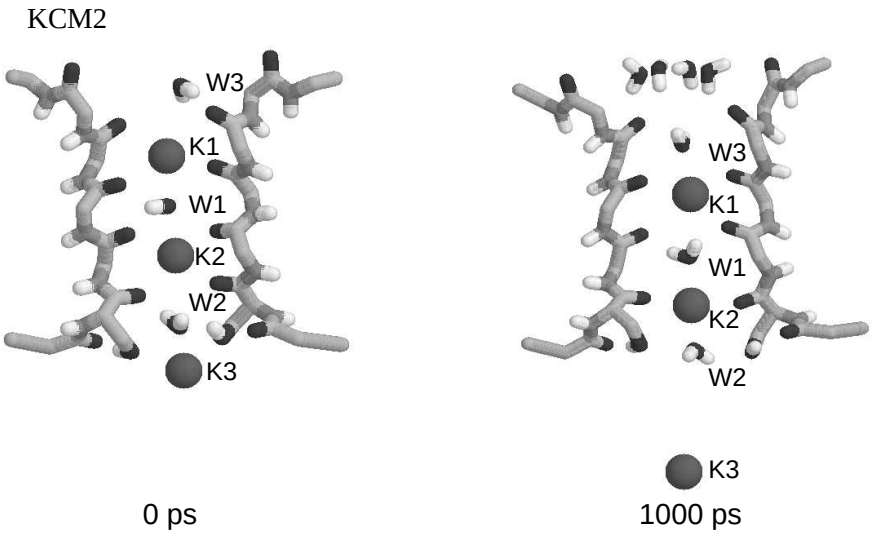

Figure 5.3.: The initial and the final configurations of the selectivity filter in KCM2. Only the backbone of the selectivity filter of M1 and M3 are shown. The occupancy state of the selectivity filter transfers from (01010) to (00101) during the simulation. A 'water ring' composed of four waters appears at the extracellular mouth in the final snapshot.

filter was widened up (see section 4.6.1), and thus more water molecules from the cavity were able to have close contact with K2. These water molecules gradually replaced the carbonyl oxygens of Thr^{75} to bind to K2 and finally detached K2 from the selectivity filter. After the displacement of K2, only K1 remained in the selectivity filter. The filter structure was further disfigured with a single-ion occupancy state. The trajectories of two water molecules W1 and W2 are also shown in Fig. 5.2. W1 was located at binding site S_3 between K1 and K2 at the beginning of the simulation. It moved downward into the central cavity at 950 ps after the displacement of K2. W2 was located initially in the extracellular space. It entered the selectivity filter from the extracellular mouth at 1000 ps and bound to K1. Later, some other water molecules entered the filter from both the inner and the outer entryways of the filter and flowed through the filter (not shown in Fig. 5.2). It implies that the filter was widened up and water molecules were able to move through the space between K1 and the selectivity filter. Ion K3 kept fluctuating up and down in the cavity for the whole simulation period.

In simulation KCM2, the structure of the selectivity filter was well sustained during the simulation. In Fig. 5.2, the z-trajectories of three water molecules W1, W2, and W3 are also presented. W1 was located at site S_2 between K1 and K2, W2 was at S_4 between K2 and K3, and W3 was at the extracellular mouth at the beginning of the simulation. A transition from the (01010) state to the (00101) state occurred in the first 50 ps, in which ion K1, K2, and water W1, W2, and W3 moved concertedly downward along the z-axis in the selectivity filter. The whole translocation process took

less than 10 ps. After this movement, K1 and K2 remained stably at binding site S_2 and S_4 respectively till the end of the simulation. It seems that the (00101) state is more stable than the (01010) state, agreed to the observation of the FEP calculations [89]. Site S_0 was occupied sometimes by more than one water molecules at the same time. As described in section 2.3, because of the special structure of the extracellular mouth constructed by the Gly^{79}, water molecules at the extracellular mouth can form a **water ring**, which usually contains four water molecules. Fig 5.3 shows the initial and final configuration of the selectivity filter. As shown in this figure, a water ring appeared at the extracellular mouth in the final configuration of the simulation. The water ring can serve in the hydration of the K^+ at S_0, and can be considered as an extended part of the selectivity filter. Of course, the water ring is not a fixed structure. Water molecules are mobile, and form a ring only at times. The formation of a water ring also relies on the occupancy state in site S_0.

5.2.2. Dynamics of K^+ and water in single-ion SMD simulations

Among the three single-ion SMD simulations, the ion dynamics in simulation SMD1 and SMD3 have similar features. The z-trajectories of potassium ions K1, K2, K3, and some water molecules in simulation SMD1 and SMD3 are shown in Fig. 5.4 and Fig. 5.5, relative to the average position of the backbone carbonyl oxygens of residues TTVGYG. The definition of the water dipole orientation appears in this figure will be given later. In single-ion SMD simulations, an external force was exerted on ion K1 and pulled K1 towards the extracellular mouth. In SMD1, the external force induced the first translocation of K1 from binding site S_1 to S_0 at 140 ps. Following the movement of K1, a **concerted movement** occurred to W1 and K2 at 140–146 ps, where W1 and K2 moved from site (S_2, S_3) to (S_1, S_2) respectively. As we can see in Fig. 5.4, the carbonyl oxygens of the filter residues shifted slightly downward in this concerted transportation. The whole transition of K1, W1, and K2 took less than 10 ps. It looked like that they were bound to a K-W-K complex and moved together as an integral.

The spontaneous translocation of K2 and W1 was not expected at all. Intuitively, because of the electrostatic repulsion between ions, we thought that a configuration with a longer inter-ion distance should be energetically more favored. And this was not a single case. The same spontaneous translocation also occurred in SMD3, where K1, W1, and K2 moved concertedly upward at 160 ps. In SMD3, the carbonyl oxygens of the filter residues also had a downward shift when the concerted translocation occurred (Fig. 5.5). Ion K2 remained at site S_2 after the translocation till the end of the simulation in both SMD1 and SMD3.

Fig 5.6 shows the time variation of the number of molecules surrounding K1 in SMD1–3. At the beginning, K1 was surrounded by 5–7 carbonyl oxygens. After K1 moved to S_0, the number of surrounding carbonyl groups decreased to 4, because the carbonyl oxygens of Gly^{79} didn't bind to K1 directly; in the meantime, the number of water surrounding K1 increased from 2 to 4. The extracellular mouth was surrounded by a water ring, as

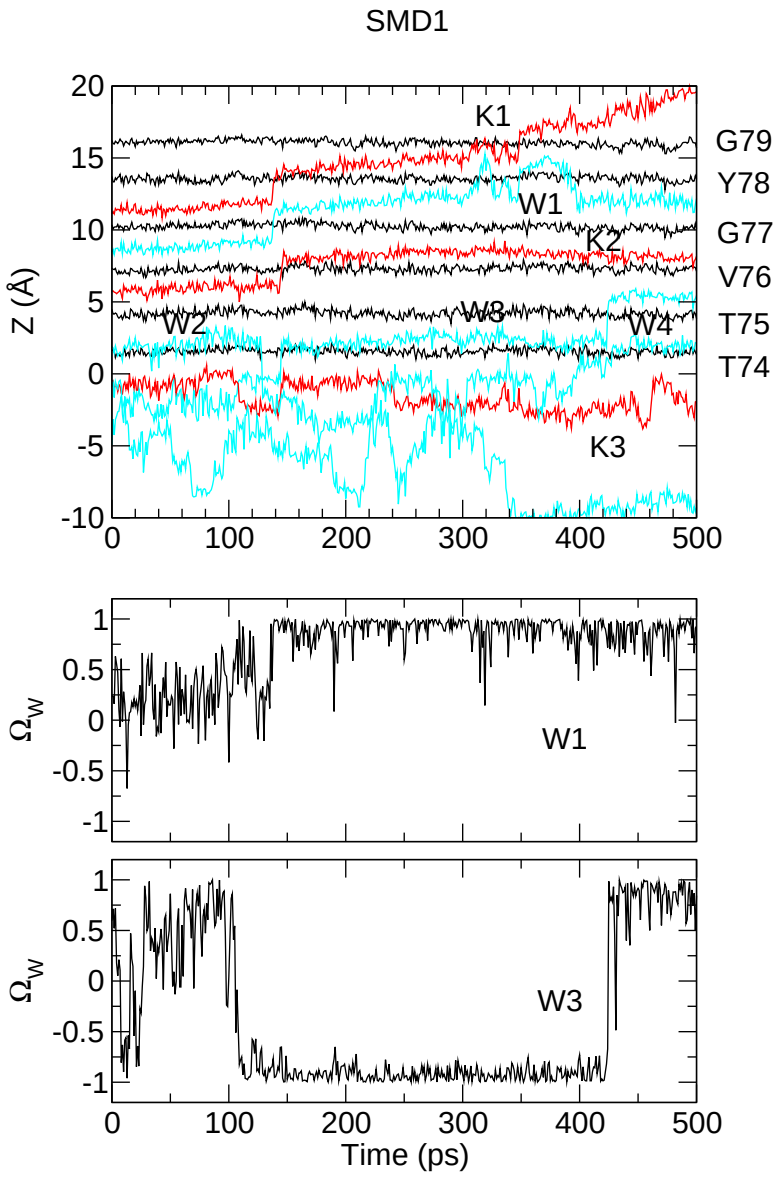

Figure 5.4.: Top: ion dynamics in SMD1. The z-trajectories of ions K1, K2, K3 (red), water molecules W1–W4 (cyan), and the carbonyl oxygens of the selectivity filter residues T-T-V-G-Y-G (black) are shown. A concerted movement of K1, K2, and W1 occurs spontaneously around 140 ps, where K1, K2, and W1 translocate concertedly upward to the next binding sites. K1 escapes completely from the selectivity filter at 350 ps. Middle and bottom: the water dipole orientation Ω_W of W1 and W3. At 140 ps when W1 translocates from S_2 to S_1, it orients upward ($\Omega_W \sim 1$) and bind to K1. The Ω_W of W3 switches to -1 at 110 ps and remains in this value. It switches from -1 to +1 at 430 ps when moving from S_4 to S_3.

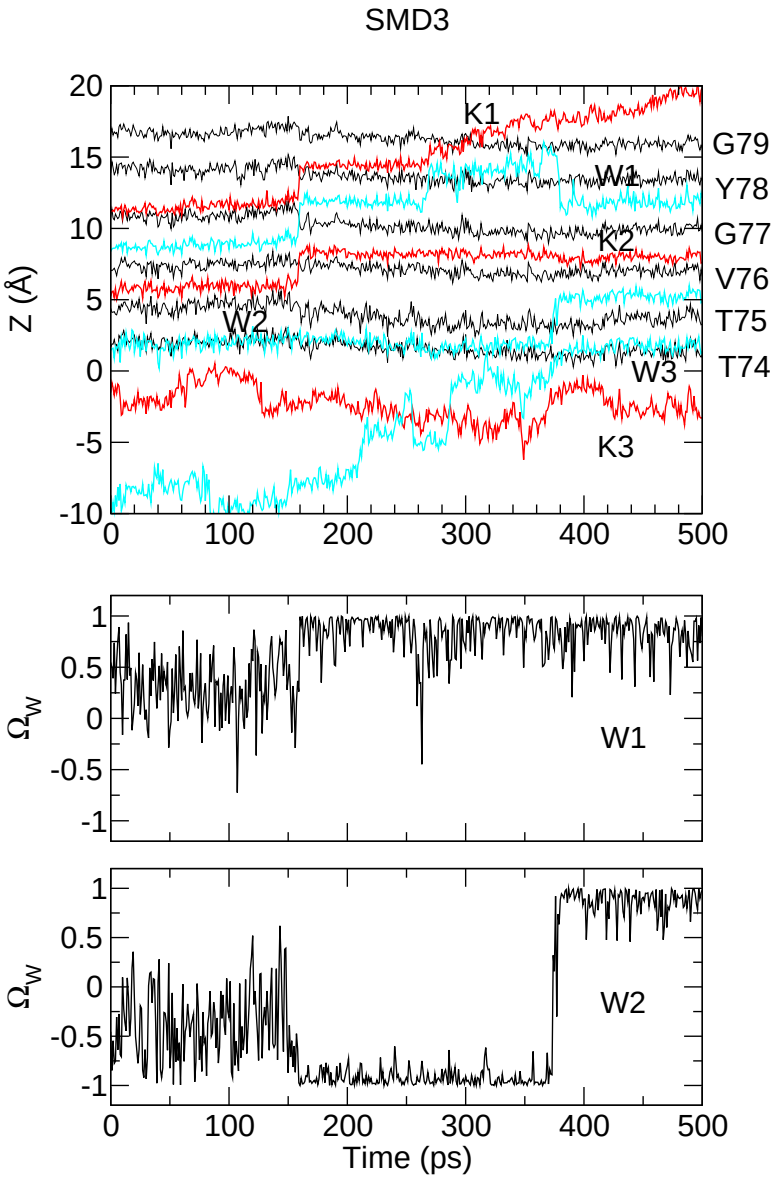

Figure 5.5.: Top: ion dynamics in SMD3. The z-trajectories of ions K1, K2, K3 (red), water molecules W1–W3 (cyan), and the carbonyl oxygens of the selectivity filter residues T-T-V-G-Y-G (black) are shown. A concerted movement of K1, K2, and W1 occurs around 160 ps, where K1, K2, and W1 translocate concertedly upward to the next binding sites. K1 escapes completely from the selectivity filter at 300 ps. Middle and bottom: the water dipole orientation Ω_W of W1 and W2. Ω_W of W1 turns to +1 when W1 moved from S_2 to S_1 at 160 ps. W2 oriented downward when K2 moves from S_3 to S_2 and oriented upward when W2 moves from S_4 to S_3.

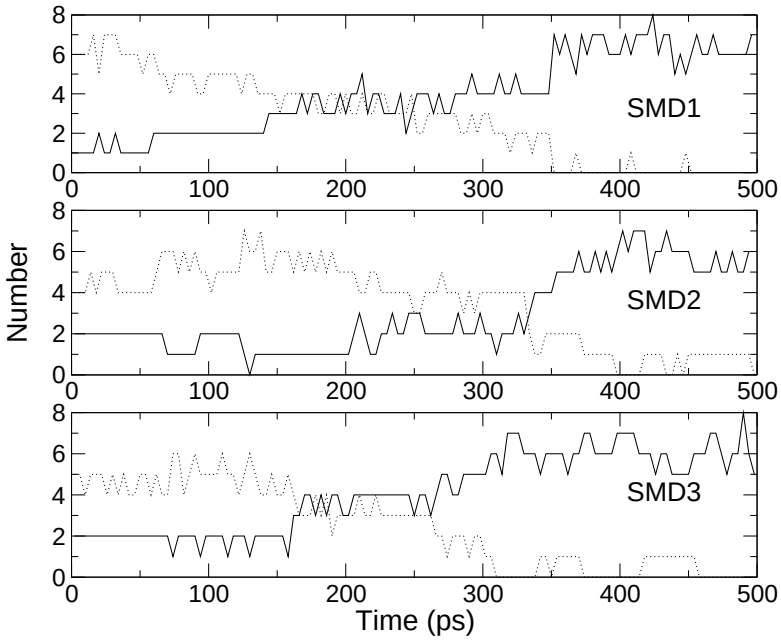

Figure 5.6.: Time variation of the number of water (solid) and carbonyl group (dot) surrounding K1 in simulation SMD1, SMD2, and SMD3.

revealed in the crystallographic structure. In SMD1, K1 stayed at S_0 for about 200 ps. Finally it penetrated through the water ring at 350 ps and was completely hydrated by 6–7 water molecules. In SMD3, K1 stayed at S_0 for a shorter period. At 300 ps the number of carbonyl groups surrounding it decreased to zero, and the number of water molecules increased to ∼6 at the same time, implying that K1 escaped completely from the channel pore.

Here we introduce a variable Ω_W for the orientation of a water dipole along the z-axis to describe the motion of a water molecule in the selectivity filter. Ω_W is defined by

$$\Omega_W = z_O - z_{HH}/r_{O\text{-}HH}, \tag{5.4}$$

where z_O is the z-coordinate of the water oxygen, z_{HH} is the z-coordinate of the center of the two hydrogen atoms, and $r_{O\text{-}HH}$ is the distance between water oxygen and the center of the two hydrogens. The water dipole orientation Ω_W is equal to 1 when the water oxygen pointing upward along the z-axis, -1 when it points downward, as illustrated in Fig. 5.7. According to the definition, we have calculated Ω_W of waters appeared in the selectivity filter. In Fig. 5.4, the time variation of Ω_W of W1 and W3 of SMD1 are given. We found that the translocation of water molecules in the selectivity filter has particular features. A clear transition occurred to the Ω_W whenever the water molecule translocated to a neighboring site, e.g. the Ω_{W1} switched from 0 to +1 at 140 ps when W1 moved from S_2 to S_1, and Ω_{W3} switched from −1 to +1 at 430 ps when W3 moved from S_4 to S_3. It reveals that the translocation of a water molecule in the selectivity

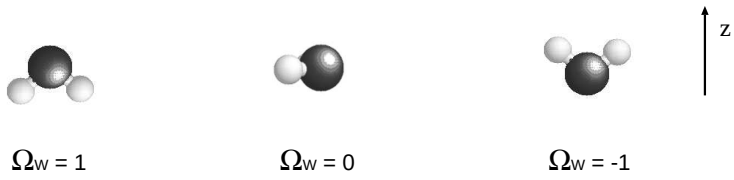

Figure 5.7.: Definition of the water dipole orientation Ω_W along the z-axis.

filter is not only a simple displacement, but involving many tumbles and rotations of the water molecule. The two water hydrogens attach to the carbonyl oxygen, like a gymnast holding the rings with his two hands, and then flip upward to shift to the next binding site. We observed that in the upward translocation of a water molecule, the water will orient upward (i.e. $\Omega_W > 0$) after the translocation, and in a downward translocation is the other way round (i.e. $\Omega_W < 0$). The orientation of a water dipole is determined by the relative positions of surrounding ions and carbonyl groups of the selectivity filter, and it has significant contribution to the concerted translocation of K^+. Further discussion will be presented in section 5.3.

In both SMD1 and SMD3, W1 oriented upward after the first translocation (Fig. 5.4, Fig. 5.5). The oxygen atom of W1 was bound to K1 afterwards, and they formed an ion-water complex. Following the movement of K1, W1 hopped back and forth between S_1 and S_0 at the time between 300–400 ps. The ion-water complex was eventually broken up when K1 escaped from the channel pore and W1 fell back to S_1. The oxygen of W3 was bound to K3 as it entered the selectivity filter at 100 ps, and thus its Ω_W was close to -1 (Fig. 5.4). In both SMD1 and SMD3, it happened that water molecules were **sucked in** to the filter from the inner entryway. The water at S_4 translocated to S_3, and its Ω_W flipped from -1 to $+1$ at the same time. The sucked-in phenomena offer us a probable mechanism to transport K^+ from the cavity into the selectivity filter. If the water at S_4 is bound to a K^+ below it, it may have a chance to bring the K^+ with it to enter the selectivity filter. In SMD1, K3 was unbound from W3 at 240 ps. Therefore, when W3 translocated into S_3 it failed to bring K3 upward with it. The same happened to water W2 in SMD3 when it translocated into S_3 (Fig. 5.5). We suggest that for a continual flow of potassium ions, there should be at least two K^+ in the cavity at the same time, so that the electrostatic repulsion between K^+ can aid to drive a K^+ entering the selectivity filter.

The z-trajectories of the three K^+ and some water molecules (W1–W5) in simulation SMD2 are shown in Fig. 5.8. The first translocation of K1 from site S_1 to S_0 occurred at 200 ps. Different from the other two simulations, no concerted movement was observed in this simulation. Instead, W1 and K2 remained in their initial locations (site S_2 and S_3) for the whole simulation. The structure of the selectivity filter was deformed during the simulation. The Val^{76}-Gly^{77} backbone of monomer M4 twisted, which made the carbonyl oxygen of Val^{76} point away from the pore axis, and the amide hydrogen of Gly^{77} turn

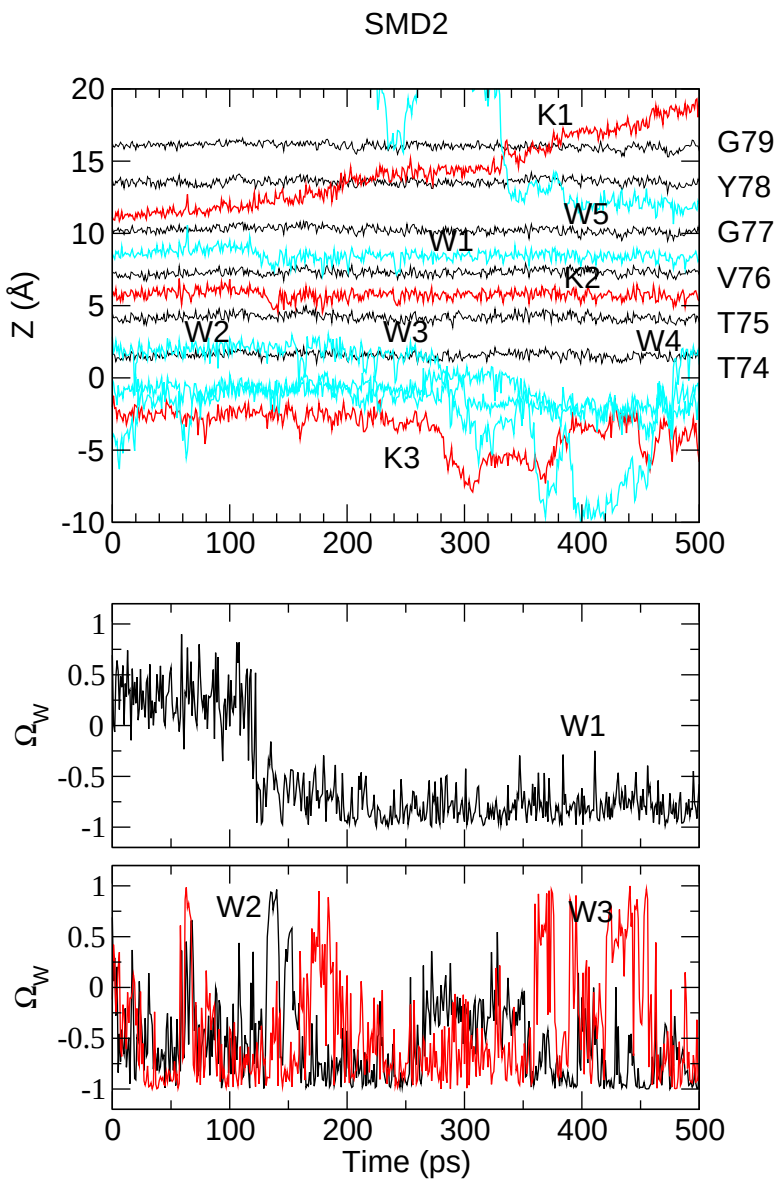

Figure 5.8.: Top: The z-trajectories of ions K1, K2, K3 (red), water molecules W1–W5 (cyan), and the carbonyl oxygens of the selectivity filter residues T-T-V-G-Y-G (black) are shown. K1 translocates from S_1 to S_0 at 200 ps and escapes from the selectivity filter at 380 ps. K2 and W1 remained in S_3 and S_2 respectively through the whole simulation. Middle and bottom: the water dipole orientation Ω_W of W1, W2, and W3. At 125 ps the Ω_W of W1 turns to -1 and remains in this value till the end of the simulation.

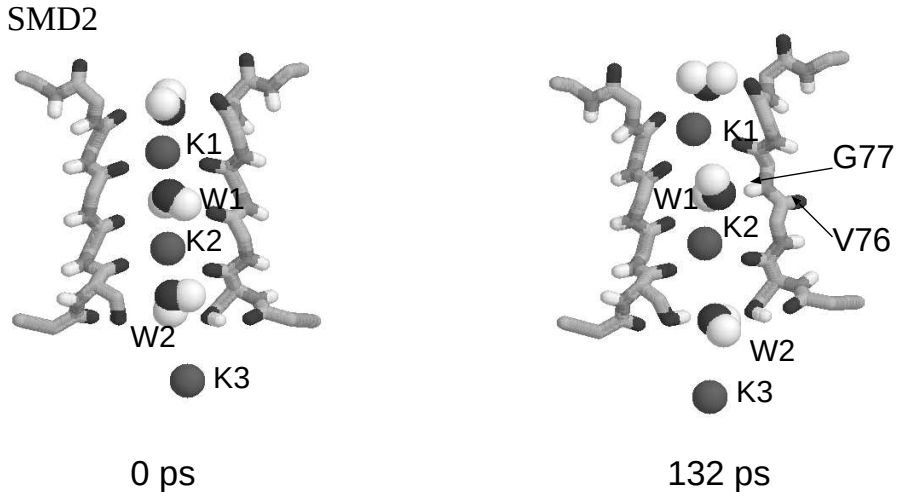

Figure 5.9.: Snapshots of the selectivity filter from SMD2. The twist of the backbone of Val^{76}-Gly^{77} of M4 is caused by the tumbling motion of W1. W1 binds to the amide hydrogen of Gly^{77} of M4 after then and the filter is blocked.

in and point to the pore axis, as described in section 4.6.2. The twist of the Val^{76}-Gly^{77} backbone was induced by the tumbling motion of W1. Being wedged between K1 and K2, W1 was at its optimal orientation at the beginning, which is slightly upward. Owing to the movement of K1, W1 had to adjust both its orientation and position. Unlike in SMD1 and SMD3, in SMD2, when K1 translocated to S_0, W1 failed to bind to K1. As shown in Fig. 5.8, the Ω_W of W1 fluctuated between 0 and +1 between 125 and 130 ps and caused the Val^{76}-Gly^{77} backbone of M2 to twist for short time and then turn back to the original orientation. Later it caused the same segment of M4 to twist. The oxygen atom of W1 and the amide hydrogen of Gly^{77} of M4 formed a stable hydrogen bond and remained like this for the rest of the simulation. The water-induced deformation of the selectivity filter is shown in Fig. 5.9. The binding of W1 and the amide hydrogen of Gly^{77} blocked the selectivity filter and thus W1 and K2 remained at the same biding sites till the end of the simulation. The crystallographic structure of the KcsA channel at low salt concentration resolved by Zhou et al. [4] shows similar structural deformation on the selectivity filter. We suggest that if a K^+ enters the selectivity filter from the extracellular mouth, it might activate W1 again, so that W1 can unbind itself from the amide hydrogen of Gly^{77}, and the structure of the selectivity filter may be recovered. While in a low salt concentration environment, the occurrence of such events is less probable, and thus the filter structure remains in a disfunction conformation.

K1 kept fluctuating at site S_0 till 380 ps and moved to S_{ext}. It stayed at S_{ext} for a short period till it was fully hydrated by 6–8 waters (Fig. 5.6). Afterwards some water molecules entered the selectivity filter from the extracellular mouth, as shown in Fig. 5.8,

and occupancy state became (00010) at the end of the simulation.

5.2.3. Dynamics of K^+ and water in multi-ion SMD simulations

In multi-ion SMD simulations, the external forces were applied to all three K^+. Therefore the movements of ions in multi-ion SMD simulations were more restricted. The trajectories of ions K1, K2, K3 and water molecules W1 and W2 of the multi-ion SMD simulations SMD4, SMD5, and SMD6 are shown in Fig. 5.10– 5.12. The average position of the backbone carbonyl oxygens of the selectivity filter residues TTVGYG are given for comparisons as usual. In SMD4, the first translocation of all three K^+ ions happened between 210 to 225 ps. The three K^+ and the two intervened water moved upward to the next binding sites in this movement. The shift of the carbonyl oxygens of the filter residues are even more clear here. It looks like it was the backbone carbonyl groups conveying the K-W-K-W-K complex upward. The second translocation occurred at 450 ps, where K1 moved to S_{ext} and the other K^+ and waters shifted upward to the next sites simultaneously. The time variation of the number of nearest carbonyl oxygens and water molecules surrounding K1 in all three multi-ion SMD simulation are shown in Fig. 5.13. The figure shows that in SMD4, the carbonyl groups binding to K1 were gradually replaced after 380 ps, and till 450 ps K1 was completely solvated by water molecules. Then K1 was able to escape into the extracellular space. The water dipole orientation of W1 and W2 versus time are given in Fig. 5.10. After the first translocation, W1 oriented upward and bound to K1. Comparing with the data in single-ion SMD simulation SMD1 and SMD3, the Ω_W of W1 fluctuated more when it was at S_1, because in this simulation K2 kept approaching W1. When W1 unbound from K1 at 450 ps, it oriented downward immediately and bound to K2. After moving to site S_3, water W2 fluctuated wildly between ± 1, which was due to the approach of ion K3. The occupancy state turns to be (0101x) at the end of the simulation. No extra water molecule was sucked into site S_4 till the end of the simulation.

The ion dynamics in simulation SMD5 is different from SMD4. As shown in Fig 5.11, the first translocation in SMD5 occurred at 126 ps. Only K1, W1, and K2 translocated upward. A clear downward shift of the trajectories of the carbonyl oxygens was shown as the ion-water complex moved upward, same as in SMD4. The time variation of Ω_{W3} shows that W3 oriented downward and bound to K3, and hence it failed to bring K3 to attach to the K1-W1-K2 complex. K3 moved upward and entered site S_4 later at 190 ps. Instead of shifting to the empty site S_3, water W2 exchanged its position with K3 and moved into the central cavity at 193 ps. Thus, a vacancy was generated between K2 and K3 and remained there for the rest of the simulation. K1 moved from site S_0 to S_{ext} at 400 ps. At 200 ps, the side chain of Asp^{80} of monomer M4 dislocate from its initial position. It adopted an alternative conformation and hence the carboxylate of the side chain pointed to the neighboring monomer rather than pointing downward. Since the binding between the carboxylate groups of Asp^{80} and Glu^{71} was very strong, the side chain of Glu^{71} adjusted its orientation following the movement of the side chain of Asp^{80}

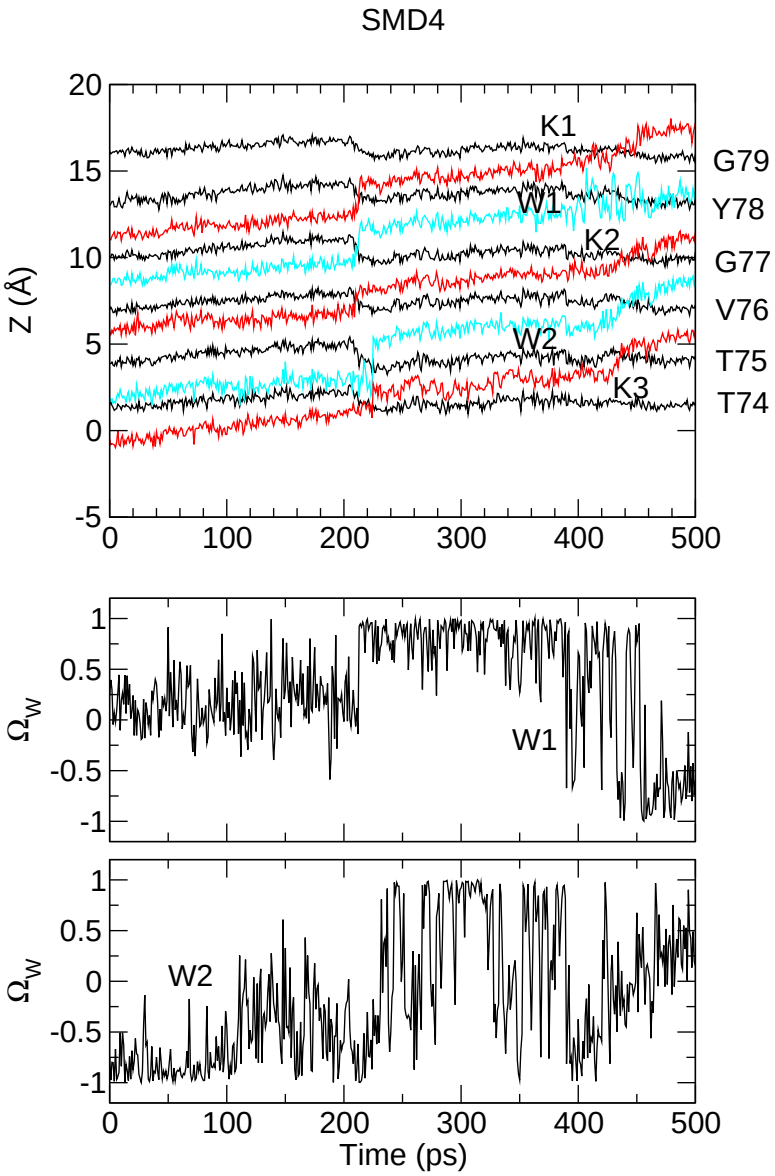

Figure 5.10.: Top: ion dynamics in SMD4. The z-trajectories of ions K1, K2, K3 (red), water molecules W1, W2 (cyan), and the carbonyl oxygens of the selectivity filter residues T-T-V-G-Y-G (black) are shown. The first concerted translocation of the K-W-K-W-K complex occurs around 210 ps. The occupancy state of the selectivity filter transfers from (01010) to (10101). A downward shift appears in the trajectories of all carbonyl oxygens of the filter residues when the concerted movement of ions takes place. The second translocation of the three K^+ and the two waters occurred at 450 ps and K1 escapes from the channel pore. Middle and bottom: the time variation of the water dipole orientation Ω_W of W1 and W2. Ω_W of both W1 and W2 turn to +1 after their upward translocation. The large fluctuation of Ω_W are caused by the approach of the K^+ below.

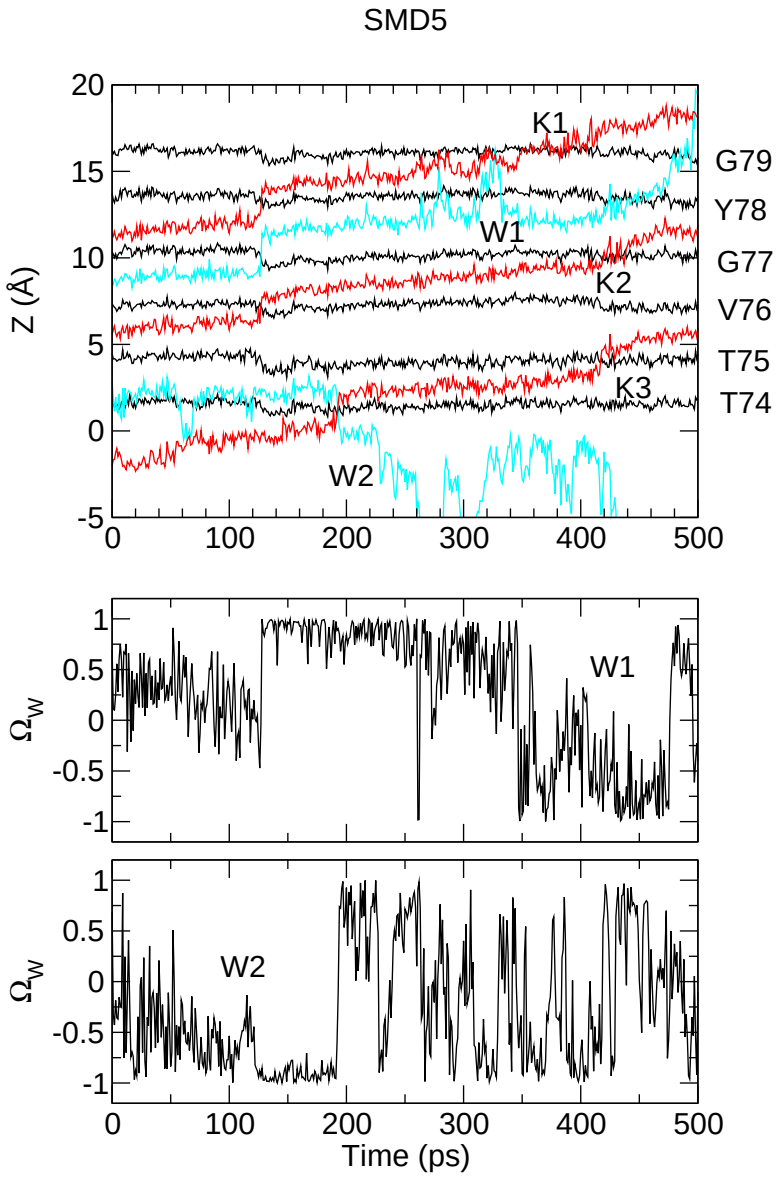

Figure 5.11.: Top: ion dynamics in SMD5. The z-trajectories of ions K1, K2, K3 (red), water molecules W1, W2 (cyan), and the carbonyl oxygens of the selectivity filter residues T-T-V-G-Y-G (black) are shown. The first concerted translocation occurs around 126 ps. Only K1, W1, and K2 translocated upward cooperatively. W2 failed to bind to K2 and move downward into the cavity at 193 ps. K3 moved into the filter later at 190 ps. K1 escapes from the channel pore at 400 ps, and K2 and K3 translocate upward to (S_1, S_3) at 420 ps. Middle and bottom: the water dipole orientation Ω_W of W1 and W2. Ω_W shows a clear transition whenever the translocation of water occurs.

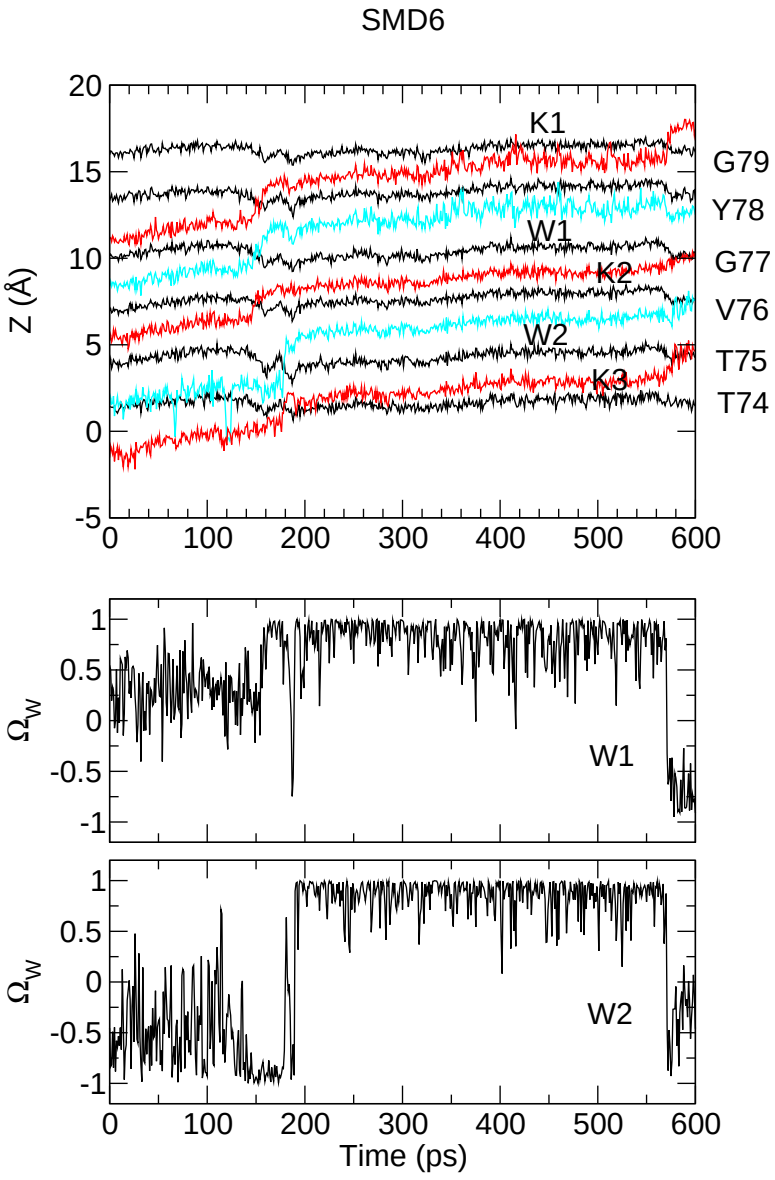

Figure 5.12.: Top: ion dynamics in SMD6. The z-trajectories of ions K1, K2, K3 (red), water molecules W1–W4 (cyan), and the carbonyl oxygens of the selectivity filter residues T-T-V-G-Y-G (black) are shown. The first concerted translocation of the K-W-K-W-K complex occurs around 150–180 ps, and the second concerted translocation occurs at 570 ps. Middle and bottom: the time variation of the water dipole orientation Ω_W of W1 and W2.

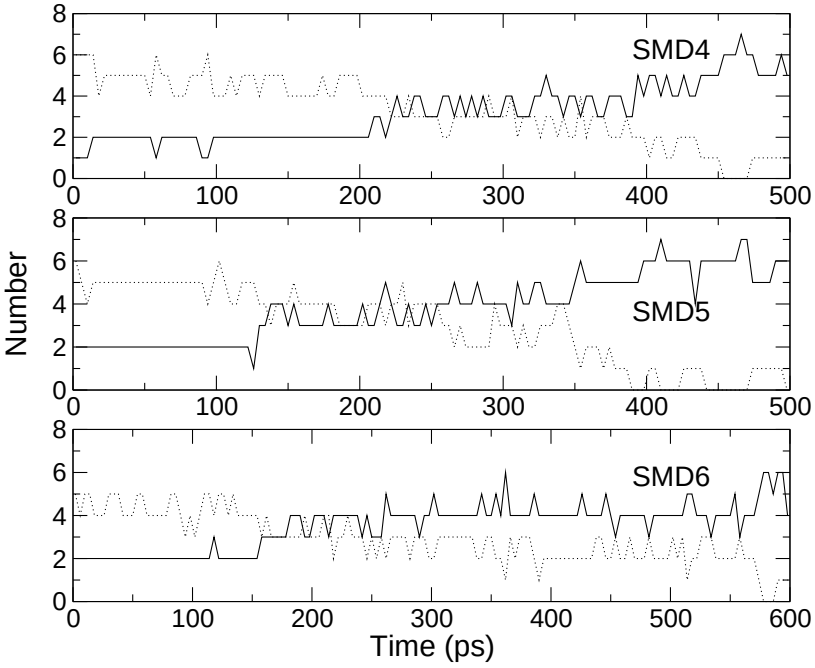

Figure 5.13.: Time variation of the number of nearest neighbor of ion K1 from carbonyl groups (dot), and from water (solid) in SMD4, SMD5, and SMD6.

(see Fig. 4.13). As described in section 4.6.2, due to the dislocation of the side chain of Glu^{71}, some hydrogen bonds which should support the structure of the selectivity filter were broken, but the filter structure was still well sustained, because the K^+ inside the filter were able to stabilize its structure. The binding of Glu^{71}HE1-Asp^{80}OD of M4 was finally broken around 400 ps when K1 escaped from site S_0. Water molecules have replaced the carbonyl oxygens and solvated K1 within a short period. W1 was bound to K1 and moved back and forth between site S_1 and S_0 at 270–340 ps. At 340 ps when the binding of K1 and W1 was broken, W1 oriented downward and bound to K2. K3 moved from site S_4 to S_3 at 420 ps and drove K2 and W1 shifting from site (S_1, S_2) to (S_0, S_1). W1 was replaced by other water molecules entering from the extracellular mouth and it escaped into the extracellular space at the end of the simulation. The occupancy state of the selectivity filter becomes (01x1x) at 500 ps; binding site S_2 and S_4 were left empty till the end of the simulation.

The translocation process in simulation SMD6 has similar pattern as in SMD4. In SMD6, the first concerted translocation of the K-W-K-W-K complex occurred at 150–180 ps (see Fig. 5.12). A downward shift of the trajectories of the carbonyl oxygens was observed in SMD6 as well. It took longer for the second concerted translocation to occur in this simulation. At 570 ps, the K-W-K-W-K complex moved upward to the next binding sites in the selectivity filter and K1 moved to S_{ext}. The same deformation as in SMD5 at the selectivity filter region also happened in SMD6. The side chains of Asp^{80} of

monomer M3 and M4 dislocated at 160–180 ps, and hence the hydrogen bonds between $Gly^{79}HN$ and $Asp^{80}OD$ were broken. Without the counterbalance of these hydrogen bonds, the binding between the carbonyl oxygens and K^+ were stronger and thus the whole filter backbone shifted slightly upward with the movements of ions. This explains why the occurrence of the second translocation in SMD6 took a longer time. The water dipole orientation of water W1 and W2 is rather stable in SMD6, compared to SMD4 and SMD5. The difference mainly came from different initial configuration, in which the ion-ion distances were slightly different among the three simulations. After the first concerted translocation, both W1 and W2 oriented upward and bound to the K^+ above them. When the second translocation of the ion-water complex took place, both of them oriented downward almost simultaneously.

5.3. The concerted movement in the selectivity filter of KcsA channel

The concerted movement of K^+ and water in SMD1 and SMD3 is the most important observation of our work. It provides us an insight to the mechanism of the high conduction rate in K^+ channels. This phenomenon has also been observed in some other MD simulations of KcsA channels [14, 15]. Yet a clear explanation of its molecular mechanism is still absent. In this section, I will focus on this phenomenon, and try to investigate its molecular mechanism.

First we examine the interaction energy between those atoms involved in the concerted movement. In simulation SMD1, the concerted translocation occurred around 140 ps. Figure. 5.14 shows the variation of the interaction energy between ions, waters, and the carbonyl groups of the filter residues before and after the first translocation. Both electrostatic and van der Waals interactions were involved in the energy calculation. The interaction energy involving carbonyl groups were summed over the four monomers. From the figure one can see that between 140–150 ps there is a clear transition of the interaction energy between K2 and the carbonyl groups of Thr^{75} and Gly^{77}. The interaction between K2 and $Thr^{75}CO$ switched from -25 to $+10$ kcal mol^{-1} around 145 ps, and meanwhile, between K2 and $Gly^{77}CO$ it switched from $+20$ to -15 kcal mol^{-1}. Between K2 and $Val^{76}CO$ it turned slightly more attractive (from -20 to -30 kcal mol^{-1}) after the translocation. Before the translocation took place, K2 was surrounded by the carbonyl groups of Thr^{75} and Val^{76}, and after the translocation by the carbonyl groups of Val^{76} and Gly^{77}. That is, the interactions between K2 and the carbonyl groups surrounding it are attractive, while between K2 and the carbonyl groups from the neighboring sites are repulsive. Similar transition of the interaction energy occurred to W1 as well. Fig. 5.4 shows that the dipole orientation Ω_{W1} is ≥ 0 most of the time, implying that its negatively charged oxygen pointed more upward most of the time, and hence the interactions between W1 and the carbonyl groups/K^+ below were attractive, while between W1 and

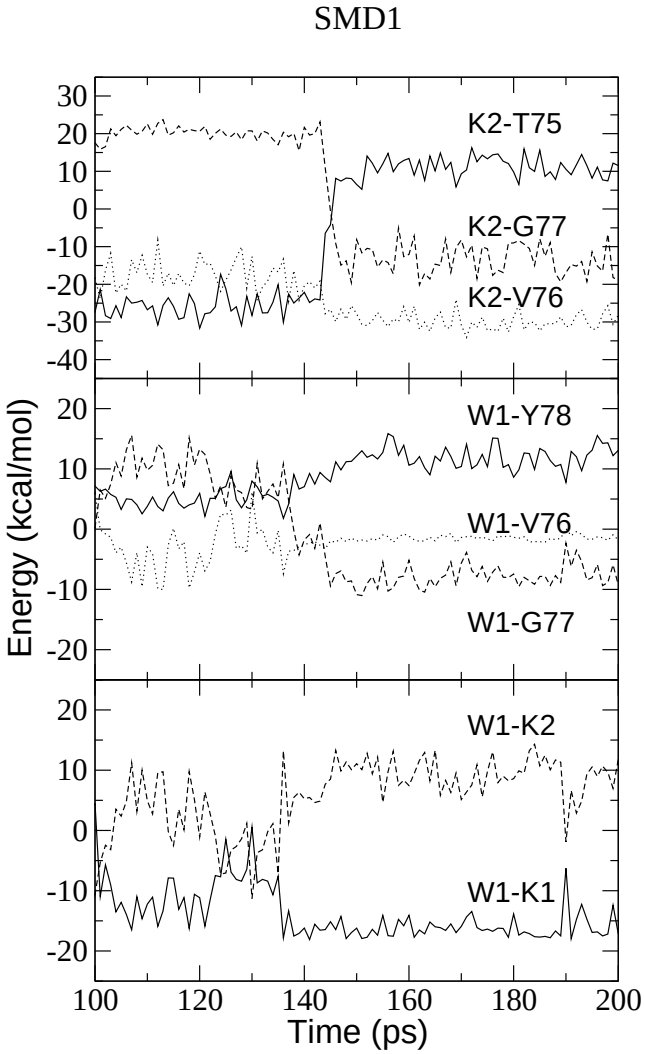

Figure 5.14.: The variation of the interaction energy before and after the first translocation in SMD1. The interaction energy between K2 and the carbonyl groups of Thr^{75}, Val^{76}, and Gly^{77} (top), between W1 and the carbonyl groups of Val^{76}, Gly^{77}, and Tyr^{78} (middle), and between W1 and K1 and K2 (bottom) are shown. Both electrostatic and van der Waals interactions were involved in the energy calculation. The interaction energy involving the carbonyl groups of the filter residues are summed over the four monomers. When K2 translocates from S_3 to S_2, the interaction between K2 and the carbonyl groups of Thr^{75} switches from attractive to repulsive with the energy transition from -25 to $+10$ kcal mol^{-1}, while between K2 and the carbonyl groups of Gly^{77} it switches from repulsive to attractive with the energy transition from $+20$ to -15 kcal mol^{-1}. Between K2 and the carbonyl groups of Val^{76} the interaction energy turns from -20 to -30 kcal mol^{-1}. After the translocation, the interaction energy between W1 and the carbonyl groups of Val^{76} becomes zero, bewteen W1 and the carbonyl groups of Gly^{77} turns to -8 kcal mol^{-1}, and bewteen W1 and the carbonyl groups of Tyr^{78} turns to $+10$ kcal mol^{-1}. W1 orients upward at 135 ps and binds to K1. The interaction energy between W1 and K1 becomes -18 kcal mol^{-1}, and between W1 and K2 turns to $+10$ kcal mol^{-1}.

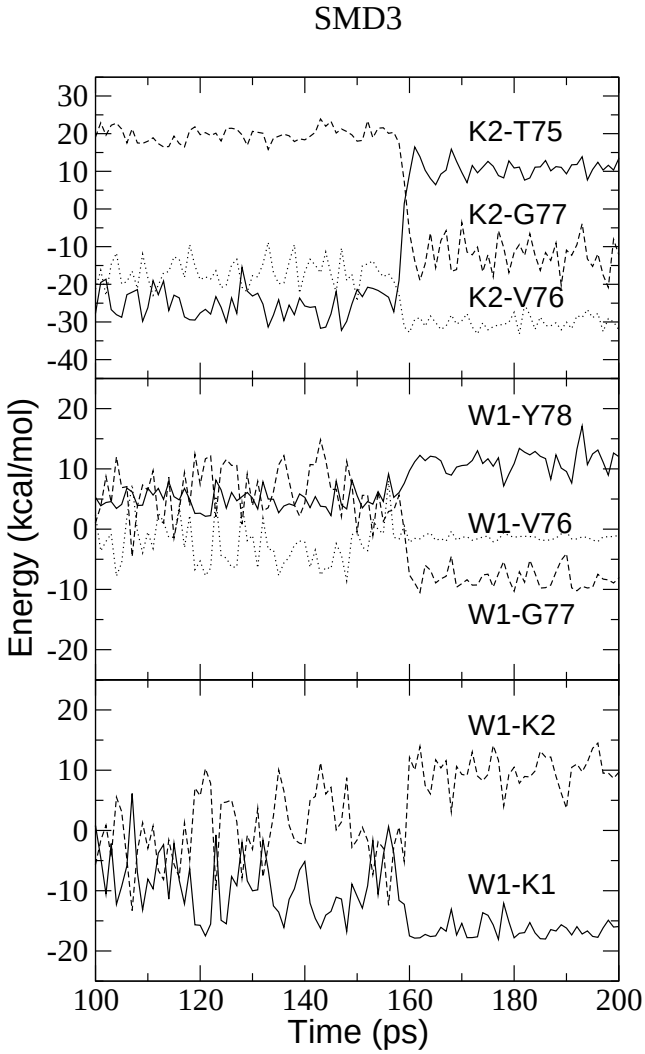

Figure 5.15.: The variation of the interaction energy before and after the first translocation in SMD3. The interaction energy between K2 and the carbonyl groups of Thr^{75}, Val^{76}, and Gly^{77} (top), between W1 and the carbonyl groups of Val^{76}, Gly^{77}, and Tyr^{78} (middle), and between W1 and K1 and K2 (bottom) are shown. Both electrostatic and van der Waals interactions were involved in the energy calculation. The interaction energy involving the carbonyl groups of the filter residues were summed over the four monomers. Similar to SMD1, when K2 translocates from S_3 to S_2, the interaction between K2 and the carbonyl groups of Thr^{75} switches from attractive to repulsive with the energy transition from -25 to $+10$ kcal mol^{-1}, while between K2 and the carbonyl groups of Gly^{77} it switches from repulsive to attractive with the energy transition from $+20$ to -15 kcal mol^{-1}. Between K2 and the carbonyl groups of Val^{76} the interaction energy turns from -20 to -30 kcal mol^{-1}. After the translocation, the interaction energy between W1 and the carbonyl groups of Val^{76} becomes zero, bewteen W1 and the carbonyl groups of Gly^{77} turns to -8 kcal mol^{-1}, and bewteen W1 and the carbonyl groups of Tyr^{78} turns to $+10$ kcal mol^{-1}. W1 orients upward at 160 ps and bound to K1. The interaction energy between W1 and K1 becomes -18 kcal mol^{-1}, and between W1 and K2 turns to $+10$ kcal mol^{-1}.

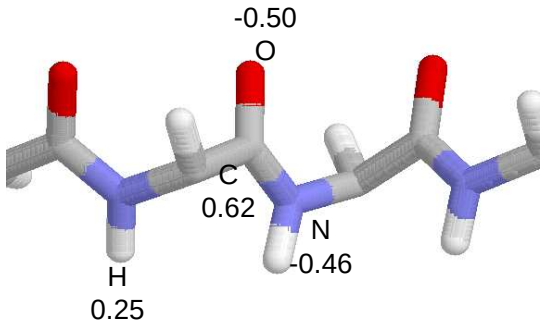

Figure 5.16.: Charge distribution of the C (grey), O (red), N (blue), and H (white) atoms on the backbone in electron unit.

the carbonyl groups/K^+ above were repulsive. After the translocation, W1 moved to S_1 and were surrounded by the carbonyl groups of Gly^{77} and Tyr^{78}. Its water dipole oriented entirely upward (with $\Omega_W \simeq 1$) and bound to K1. The interaction between W1 and the carbonyl groups of Gly^{77} became attractive with the energy of -8 kcal mol^{-1}, and between W1 and the carbonyl groups of Tyr^{78} it turned more repulsive with the energy of $+10$ kcal mol^{-1}. The interaction energy between W1 and K1 became -18 kcal mol^{-1}, and between W1 and K2 $+10$ kcal mol^{-1} after the translocation. Between a water and the carbonyl groups of residues away from it (e.g. between W1 and Val^{76} in Fig. 5.14), the interaction energy is zero. The time variation of the interaction energy between K^+, water, and the surrounding carbonyl groups around the first translocation in SMD3 are shown in Fig. 5.15. The transition features of the interaction energy in SMD3 are similar to SMD1.

From the analysis of the interaction energy, we observe that rather than the long-range electrostatic interaction, the concerted movement is more dominant by the short-range interaction with polar groups. A polar group is a chemical group with asymmetric charge distribution on its components. Water, for example, is the most important polar molecule in biophysical systems. Its oxygen atom is negatively charged, and the two hydrogens are positively charged. A polar group has only short range contribution to the electrostatic interaction. And for nearby atoms, the relative orientation of the polar group is a more crucial factor in the interaction.

The backbone carbonyl groups of the selectivity filter residues play an important role in the concerted movement. When a potassium ion sits at a binding site in the selectivity filter, it is stably coordinated by eight carbonyl oxygens above and below it. However, a

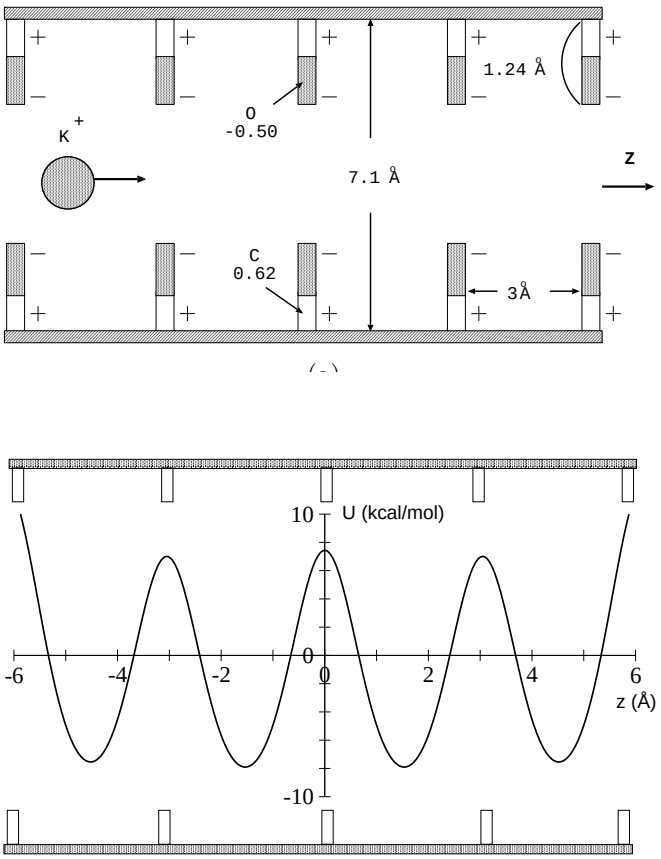

(b)

Figure 5.17.: (a) An illustration of the simplified 2-D model of the selectivity filter. Two parallel rods with the length of 12 Å long separated by 7.1 Å from each other represent the backbone of the selectivity filter. Five short sticks of the size of 1.24 Å are attached to each rods with equal spacing represent the five carbonyl groups of the five filter residues. The connecting point of each stick carries a charge of 0.62 electron unit and the tip of the stick 0.5 electron unit. (b) The energy profile along the pore axis (z-axis) for a K^+ in the 2-D model illustrated in (a). Both electrostatic and van der Waals interaction were involved in the energy calculation. Four potential wells are shown between each binding site, corresponding to the four binding sites in the selectivity filter. The energy barrier between each neighboring binding site is about 16 kcal mol^{-1}.

carbonyl group is also a polar group. Its oxygen end is negatively charged, and the carbon atom is positively charged. The charge distribution of some of the backbone atoms is given in Fig. 5.16, referred to the '91 parameter set of AMBER [42]. The carbonyl oxygen carries a charge of -0.5 electron unit and the carbon carries 0.62 electron unit. The total charge of a carbonyl group is equal to 0.12, which is slightly positive. Therefore, when a potassium ion is far from a carbonyl group, the electrostatic interaction between them should be slightly repulsive. On the contrary, when they are very close to each other, the relative orientation of the carbonyl group determines whether the interaction is repulsive or attractive.

The interaction between a K^+ and the backbone carbonyl groups of the filter can be described by a simplified 2-D model of the selectivity filter. Consider two parallel rods with the length of 12 Å long separated by 7.1 Å from each other. Five short sticks are attached to each rods with equal spacing. The short stick is of the size of 1.24 Å, which is about the equilibrium bond length of a carbonyl group. The connecting point of each stick carries a charge of 0.62 electron unit and the tip -0.5 electron unit. The 2-D model filter is as illustrated in Fig. 5.17(a). The distance between the two parallel rods is an average value obtained from MD simulation KCM2. The parallel line in the middle of the two rods is defined as the z-axis (pore-axis) of the model filter. The energy profile along the z-axis for a K^+ is as shown in Fig. 5.17(b). Both electrostatic and van der Waals interactions are involved. Four potential wells are located between each neighboring sticks, corresponding to the four binding sites in the selectivity filter. The energy barrier between neighboring binding sites is about +16 kcal mol^{-1}.

Now consider the interaction between a K^+ and only one pair of carbonyl groups in the 2-D model filter, as illustrated in Fig. 5.18(a). The energy profile for a K^+ along the z-axis is shown in Fig. 5.18(b). Two potential wells appear symmetrically with the minimum at ± 1.18 Å. At ± 3 Å the potential goes to zero and turns repulsive when the distance is > 3 Å, which is about the length of a binding site, i.e., a carbonyl group acts mainly within the range of a binding site. Now consider if the carbonyl groups are able to alter their orientation. Here we define the tip angle θ of a carbonyl group as in Fig. 5.18(a). The energy profiles along the z-axis corresponding to different tip angles θ are given in Fig. 5.18(b). One can see that as the carbonyl groups tip, the energy profile becomes asymmetric: at one side the potential well rises up, and at the other side the potential well goes down; the minimum of both potential wells shifts towards the direction opposite to the tip direction. When $\theta \geq 25°$, the two potential wells merge into one. One side of the carbonyl groups turns more attractive to a K^+, while the other side becomes non-attractive, or even repulsive to a K^+. The tipped carbonyl groups can act even in the next binding site.

The interaction energy between a K^+ and another polar molecule in the system– the water molecule– is shown in Fig. 5.19. It is calculated by fixing the water oxygen at the zero point and moving the K^+ along the z-axis. The potentials shown in the figure correspond to two different water orientations– $\Omega_W = 0$ and $\Omega_W = +1$ with respect to the z-axis. When $\Omega_W = 0$, the potential is symmetric with shallow potential wells with a

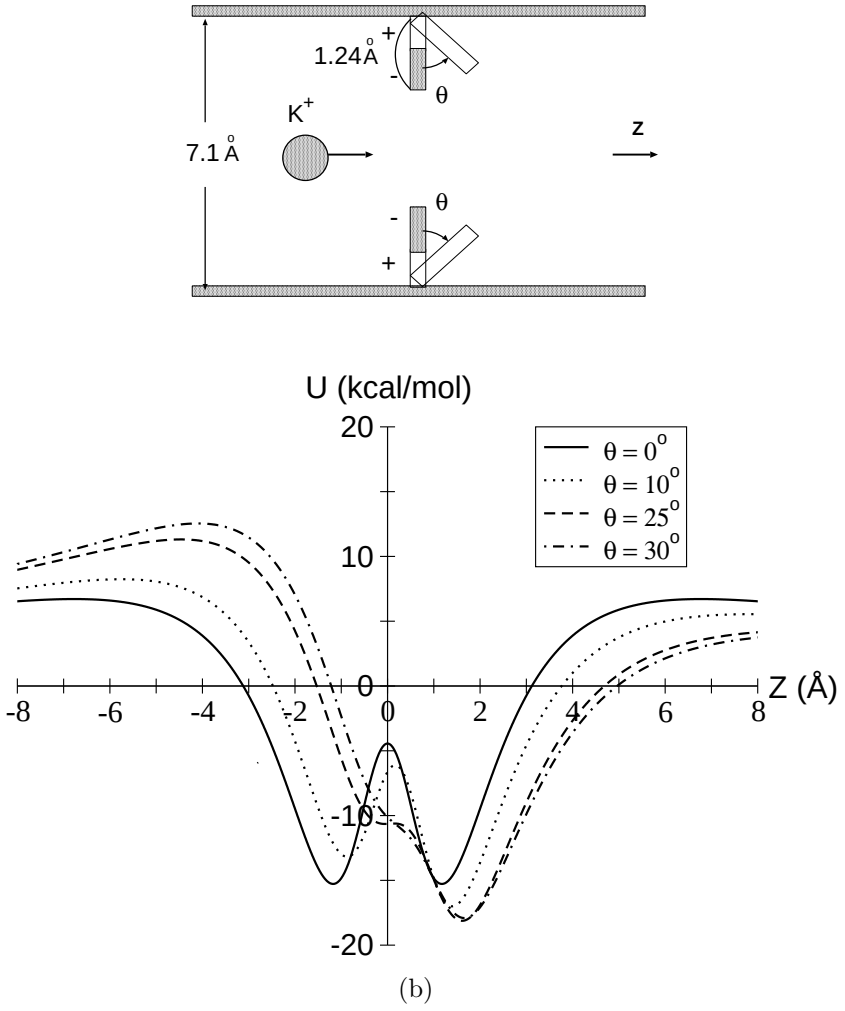

(b)

Figure 5.18.: (a) An illustration of the 2-D model filter with only one pair of carbonyl groups. The tip angle θ of the carbonyl groups can be altered. (b) The energy profile along the filter axis (z-axis) with different tip angles θ of the carbonyl groups in the 2-D model illustrated in (a). Both electrostatic and van der Waals interaction were involved in the energy calculation. When the carbonyl groups are perpendicular to the backbone rods ($\theta = 0$), two potential wells appear symmetrically at ± 1.18 Å with the depth of -15.57 kcal mol^{-1}. As θ increased, the potential well at the right side rises up, while at the left side the potential well becomes deeper, and both potential well shift leftward. When $\theta \geq 25°$, only one potential well is left.

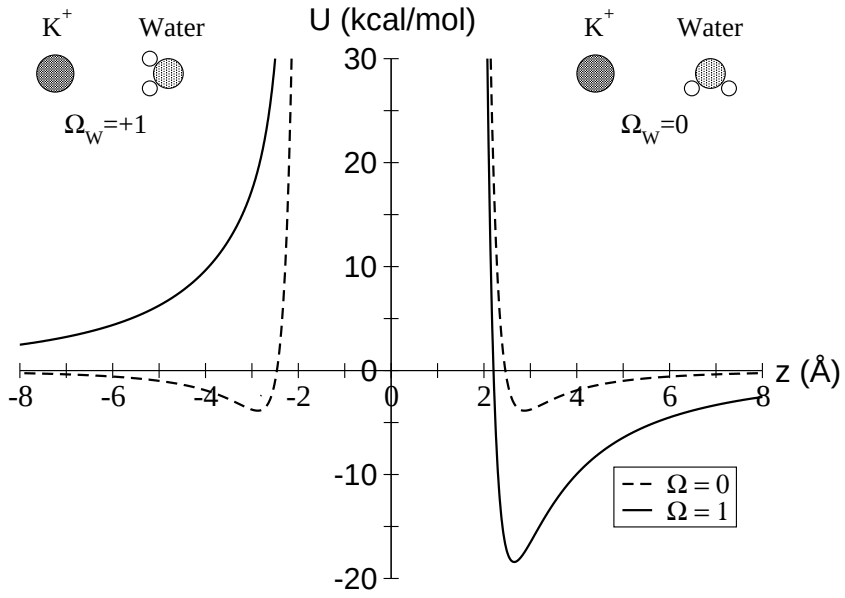

Figure 5.19.: The interaction energy between a K^+ and a water molecule in different orientations ($\Omega_W = 0 and \Omega_W = 1$).

depth of about -3 kcal mol^{-1} at ± 2.7 Å. When $\Omega_W = 1$, one side along the z-axis turns repulsive for a K^+, while the other side becomes more attractive with the well depth of -18 kcal mol^{-1}, same value as the interaction energy between K1 and W1 when they were bound with each other after the first translocation (see Fig. 5.14 and Fig. 5.15).

Now consider the interaction between a water molecule and carbonyl groups. The K^+ in Fig 5.18(a) is replaced by a water molecule, as illustrated in Fig. 5.20(a). The energy profile of the water molecule with its Ω_W fixed to 1 is shown in Fig. 5.20(b). It shows that for the water to move through the carbonyl group pair, it has to cross over an energy barrier with the height of $+21$ kcal mol^{-1}. It is mainly from the electrostatic repulsion between the water oxygen and oxygen atoms of the carbonyl groups. As the carbonyl groups tilt progressively towards the right hand hand side, the energy barrier decreases correspondingly. When the tip angle $\theta \geq 25°$, more than half of the energy barrier is reduced. It implies that when a water molecule moves through the selectivity filter, the carbonyl groups must adjust their tip angle accordingly to decrease the energy barrier in this process. Although not shown here, the water molecule will also adjust its orientation accordingly during the translocation to minimize the energy cost of the movement.

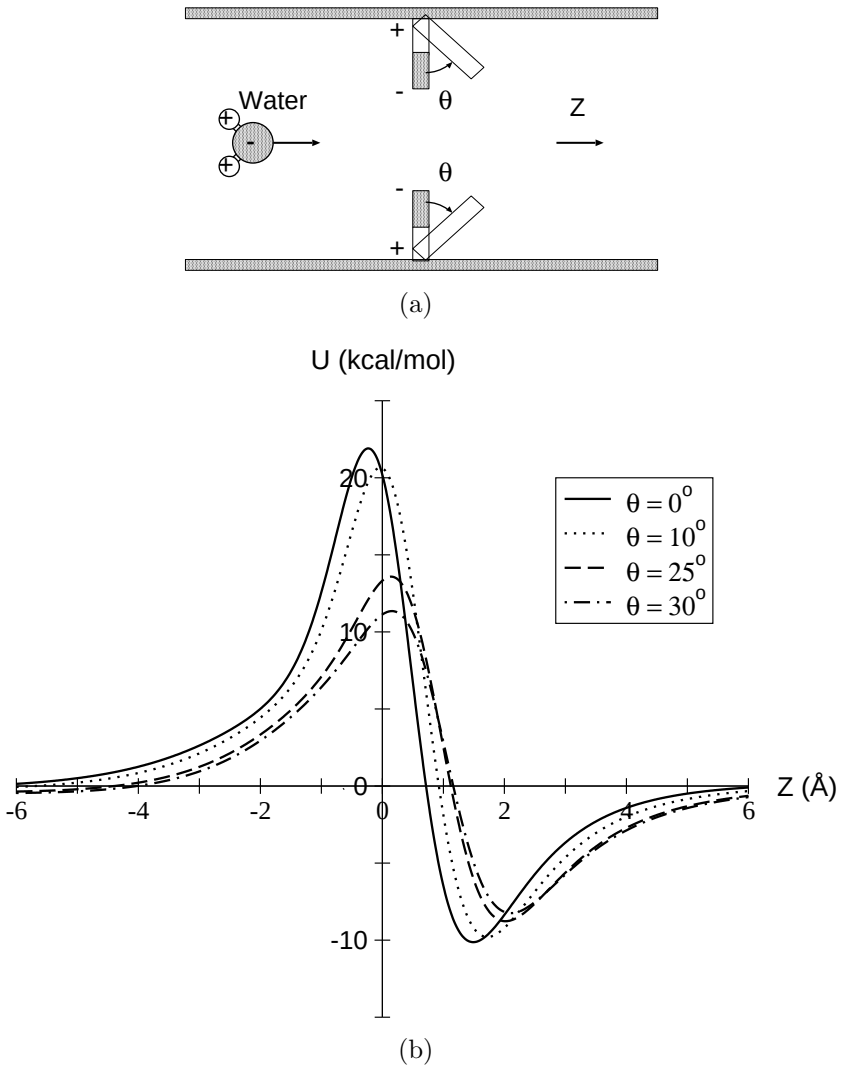

Figure 5.20.: (a) An illustration of a water with its Ω_W fixed to 1 moving along the z-axis. (b) The energy profile for a water molecule along the z-axis corresponding to different tip angle θ of the carbonyl groups illustrated in (a). Both electrostatic and van der Waals interaction were involved in the energy calculation. An energy barrier of +21 kcal mol^{-1} appears for a water molecule to move through the carbonyl groups pair with its Ω_W fixed to 1. As the tip angle θ increased, the energy barrier is reduced correspondingly. When $\theta \geq 25°$, more than half of the energy barrier is reduced.

From the simple analysis shown above, we understand that merely to alter the orientation of carbonyl groups, the interaction can be changed noticeably. This is an effective mechanism to reduce the energy barrier on the permeation pathway. We now come back to the 2-D model with five carbonyl group pairs. With certain configurations, the energy barrier between neighboring binding sites can be reduced to zero, and thus a K^+ can easily move from one site to another, as shown in Fig. 5.21. Similar variation of the potential profile appeared in SMD simulations as well. As shown in Fig. 5.22(a) and (b), we took snapshots from SMD1 and SMD3, and calculated the potential profile for a K^+ along the pore axis in the selectivity filter. Only the carbonyl groups of the five filter residues were included in the calculations. In both SMD1 and SMD3, before the translocation, K2 was located in S_3, and therefore the potential well at S_3 was deeper. Then the potential barrier between S_3 and S_2 gradually reduced to zero, and K2 was able to move to S_2. And after the translocation, the potential well at S_2 became deeper.

We can conclude that the concerted movement of K^+ is a result of interacting with the polar carbonyl groups and water molecules, or more precisely, a result of the exquisite interplay among carbonyl groups, water molecules, and K^+ itself. The movement of K^+ induces the rotation of water molecules and the alteration of the carbonyl groups' orientations, which reversely drive the K^+ to move further. To carry out such delicate cooperative movement, the length of a binding site, the width of the selectivity filter, and the size of a water molecule and a K^+ must all well match to each other. Therefore, we can say that the structure of the selectivity filter itself provides the basis for the concerted movement of potassium ions.

5.4. Summary

In this chapter, we have revealed the molecular mechanism of the concerted transportation of ions in potassium channels. The facts we observed in our simulations can be summarized as follows:

1. The binding sites S_2 and S_4 in the selectivity filter are more stable for K^+.
2. The concerted transportation is dominated by the polar interaction.
3. An alternative sequence of K^+ and water is required for the concerted transportation in the selectivity filter.

In simulation KCM2, the K-W-K-W occupancy state switched to the W-K-W-K state at the beginning of the simulation and remained in the same state through the 1 ns simulation. This result agrees with the conclusions from other more elaborate calculations, such as the free energy perturbation (FEP) calculation [89] and the umbrella sampling simulations [91]. In those studies, it is shown that the W-K-W-K occupancy state is energetically more stable than the K-W-K-W state.

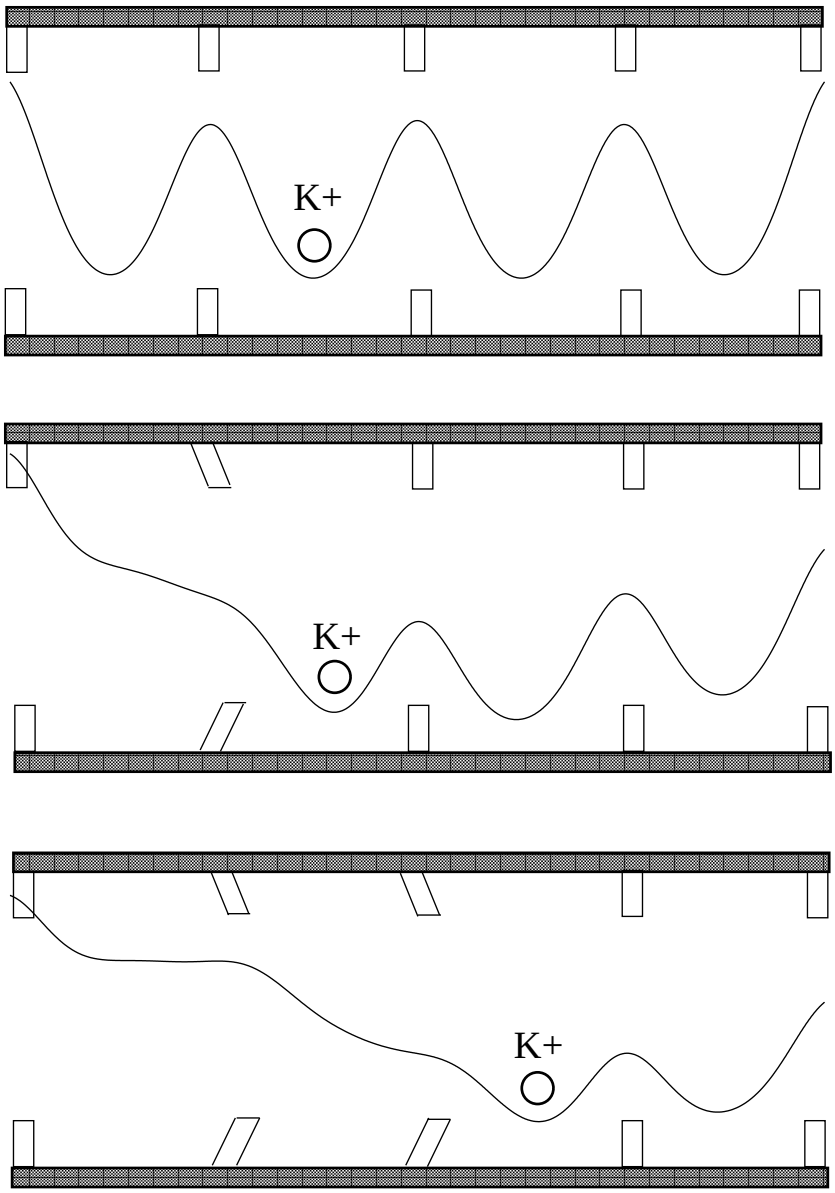

Figure 5.21.: The variation of the potential profile along the z-axis in the 2-D model of the selectivity filter corresponding to different configurations. As the carbonyl sticks tip, the energy barrier between binding site S_3 and S_2 decreases, and thus the translocation of the K^+ is possible.

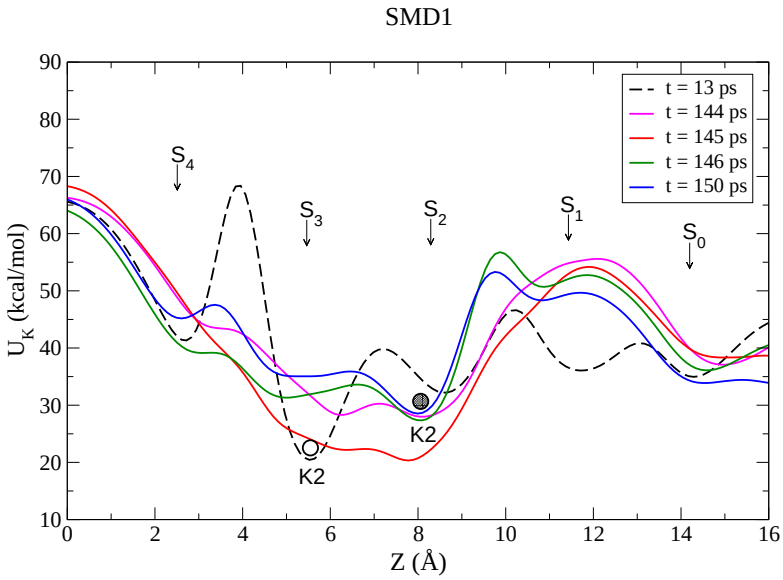

(a)

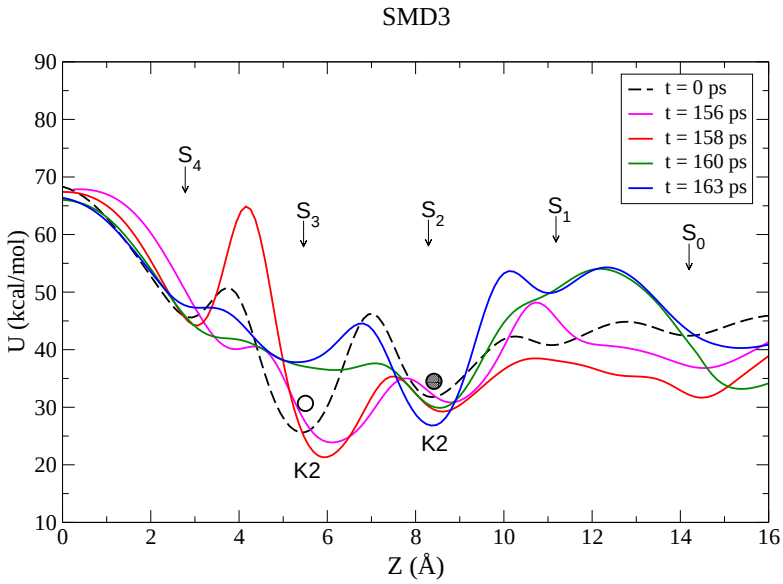

(b)

Figure 5.22.: Snapshots of the potential profile along the pore axis in the selectivity filter in (a) SMD1 and (b) SMD3. Only the carbonyl groups were involved in the potential calculation. The empty and full circles represent the position of K2 before and after the translocation (from S_3 to S_2). The energy barrier between S_3 and S_2 is reduced short before the translocation, then the two potential wells merge into one. K2 moves to S_2 and potential well at S_2 becomes deeper.

The second fact of our observations is the most important one in this study. The conventional view of the multi-ion conduction is that the electrostatic repulsion between ions counterbalances the attraction between ions and the channel. In this view, the ion channel has a fixed potential profile along the channel pore. However, the analysis of the concerted movement occurred in the SMD simulations shows that the potential profile along the channel pore is not a fixed function. The potential wells swing up and down during the simulations. Occasionally, the barrier between two potential wells may vanish, and that is the moment when a spontaneous translocation of an ion can occur. An incident like this can happen if the potential wells are constructed by polar groups. The interaction of polar groups is sensitive to the relative orientation of the polar groups, and thus the interaction form can be changed easily by altering the orientation of polar groups. The binding sites of the selectivity filter are composed of the backbone carbonyl groups, which are polar groups. If the carbonyl groups can alter their orientation simultaneously in a cooperative way, a concerted movement of ions can be induced.

To induce the cooperative motion of the carbonyl groups, the occupancy state in the selectivity filter must be an alternative sequence of K^+ and water, i.e., a "K-W-K-W" or "W-K-W-K" sequence. Water molecules plays an important role here. A water molecule is also a polar molecule. When a water molecule sitting between two K^+ in the selectivity filter, it has to rotate and flip to find the configuration of minimum energy. The rotation and flip of the water molecule induce the carbonyl groups around it to change their orientation, which then cause the translocation of K^+ and waters. The concerted movement is a very dynamical picture; it is the result of a delicate cooperation among K^+, water molecules, and the carbonyl groups. Simulation methods like the free energy perturbation or the umbrella sampling are superior on the free energy estimation though, they can only make interpolation among static pictures. The steered molecular dynamics simulation method is advantageous in revealing the dynamical parts of a reaction, and complements the whole picture.

6. Reconstructing the potential of mean force from SMD simulations

As introduced briefly in Chapter 3, the steered molecular dynamics simulation method is inspired by the atomic force microscopy (AFM) technique. The original attempt of SMD simulations is to reveal the microscopic process of AFM experiments [68]. However, these two techniques indeed work on different time scales: in AFM experiments, unbinding processes usually take place on the time scale of milliseconds to seconds, whereas SMD simulations can cover only nanosecond time scale, which is at least 10^6 times smaller than in AFM experiments. This implies that the mechanisms underlying the dissociation processes induced by these two methods are very different. AFM experiments operate in a thermally activated regime, where a system remains in quasi-equilibrium during the unbinding process, while SMD simulations operate in the drift regime, where the unbinding rate is limited by friction. A significant amount of irreversible work is generated by the fast manipulated reaction during SMD simulations. This work has to be discounted from the reversible one in order to generate comparable thermodynamic quantities.

The main purpose of employing micromanipulation methods in biomolecules studies is to induce transitions from one equilibrium state to another. The manipulated transition is an irreversible process where an extra work W is performed on the system. It has been proved that the equilibrium free energy difference ΔG between two states can be estimated from nonequilibrium processes by applying the Jarzynski identity [92, 93]:

$$\langle exp[-W(x)/k_BT]\rangle = exp[-\Delta G(x)/k_BT], \tag{6.1}$$

in which $\langle\cdots\rangle$ denotes the ensemble average over many trajectories.

However, to derive the thermodynamic energy difference from the Jarzynski identity, certain number of trajectories have to be generated to obtain reasonable statistics. Alternative algorithm employed in SMD trajectory analyses includes the application of the fluctuation-dissipation theorem, in which a fast manipulated process is represented by a one-dimensional stochastic model [94, 95, 96]. A potential corresponding to a mean force, $U(x)$, along the selected pathway x can be reconstructed from the time series of the position $x(t)$ and the applied force $F(x,t)$. An additional parameter, the friction coefficient γ, is introduced here, and the accuracy of the above potential reconstruction is usually limited by this parameter. The friction coefficient can be derived from the velocity autocorrelation analysis.

In this chapter, we employed the analysis based on the fluctuation-dissipation theorem to reconstruct the potential of mean force along the ion permeation pathway.

6.1. The stochastic model

Assume that the dissociation process of a ligand-protein complex can be described by a single reaction coordinate, which does not change when an external force is applied to the system. When the time scale of the dissociation is long compared with the relaxation times of all other degrees of freedom of the system, the friction coefficient γ between the ligand and the protein can be taken as a time-independent parameter. With these two assumptions, we can describe such a manipulated unbinding process by the Langevin equation

$$m\ddot{x} = -\gamma\dot{x} - \frac{dU}{dx} + F(x,t) + \sigma\xi(t), \tag{6.2}$$

where x is the reaction coordinate of the unbinding process, $U(x)$ is the associated thermodynamic potential, $F(x,t)$ is the applied force along the reaction path, γ is the friction coefficient, $\xi(t)$ represents the Gaussian white noise with correlation function $\langle\xi(t)\xi(t')\rangle = \delta(t-t')$, and σ is the amplitude of the fluctuating forces. For large friction coefficient, the second derivative term at the left hand side of Eq. (6.2) can be neglected. Then we obtain the stochastic differential equation

$$\gamma\dot{x} = -\frac{dU}{dx} + F(x,t) + \sigma\xi(t), \tag{6.3}$$

According to the fluctuation-dissipation theorem, parameters γ and σ are related to temperature as $\sigma^2 = 2k_BT\gamma$.

In the SMD simulation, an external force with the following functional form is applied to the system

$$F(x,t) = k_0(vt - x). \tag{6.4}$$

It corresponds to attaching a symbolic spring with spring constant k_0 to the ligand, and dragging the spring along the reaction coordinate x with the constant velocity v. According to the Boltzmann distribution of a harmonically bound particle, the position fluctuation of the attached ligand is

$$\delta x \sim (k_BT/k_0)^{1/2}, \tag{6.5}$$

and the fluctuation of the applied force is

$$\delta F \sim (k_0k_BT)^{1/2}. \tag{6.6}$$

Therefore, a stiff spring with large spring constant confines the ligand fluctuating in a small region of the binding pocket so that only local properties of the binding potential

are sampled. Meanwhile, the fluctuation of the applied force is large. Whereas for a soft spring with small spring constant, the ligand fluctuation is larger, and the force fluctuation becomes small.

The position of the ligand can be written as $x(t) = x_0(t) + \delta x(t)$, in which $x_0(t)$ represents the trajectory in the limit of zero noise, and $\delta x(t)$ is the deviation of x_0. Substitute into Eq. (6.3), and we obtain

$$\gamma(\dot{x_0} + \delta\dot{x}) = -\frac{dU(x_0 + \delta x)}{dx} + F(x_0 + \delta x, t) + \sigma\xi(t). \tag{6.7}$$

We can expand Eq.(6.7) in the power of δx. The zeroth order of the expansion is

$$\gamma\dot{x_0} = -\frac{d}{dx}U(x_0) + k_0(vt - x_0), \tag{6.8}$$

and the first-order correction is

$$\gamma\delta\dot{x} = -[k_0 + \frac{d^2}{dx_0^2}U(x_0)]\delta x + \sigma\xi(t). \tag{6.9}$$

For a stiff spring, which means $k_0 \gg |d^2U/dx^2|$, the fluctuations δx are small according to Eq. (6.5), so the higher-order corrections can be ignored, as well as the $d^2U(x_0)/dx_0^2$ term in Eq. (6.9). Equation (6.9) then becomes

$$\gamma\delta\dot{x} = -k_0\delta x + \sigma\xi(t), \tag{6.10}$$

which is the Langevin equation for an overdamped harmonic oscillator. The characteristic time τ in this system is

$$\tau = \gamma/k_0. \tag{6.11}$$

When averaged over a time scale longer than τ, the position fluctuation δx is close to zero, then we can replace $x_0(t)$ in Eq. (6.9) by the average position $\bar{x}(t)$ and get

$$\gamma\dot{\bar{x}} \approx -\frac{dU(x)}{dx} + k_0(vt - \bar{x}). \tag{6.12}$$

For a stiff spring under the overdamped condition, the average velocity $\dot{\bar{x}}(t)$ is close to v. We can then write Eq. (6.12) as

$$\bar{F} = \frac{dU(x)}{dx} + \gamma v, \tag{6.13}$$

where $\bar{F} = k_0(vt - \bar{x})$.

According to Eq. (6.13), the binding potential $U(x)$ can be obtained by integrating over the average reaction coordinate $\bar{x}$ by

$$\bar{U}(x) - U(0) = \int_0^x dx'(\bar{F} - \gamma v), \tag{6.14}$$

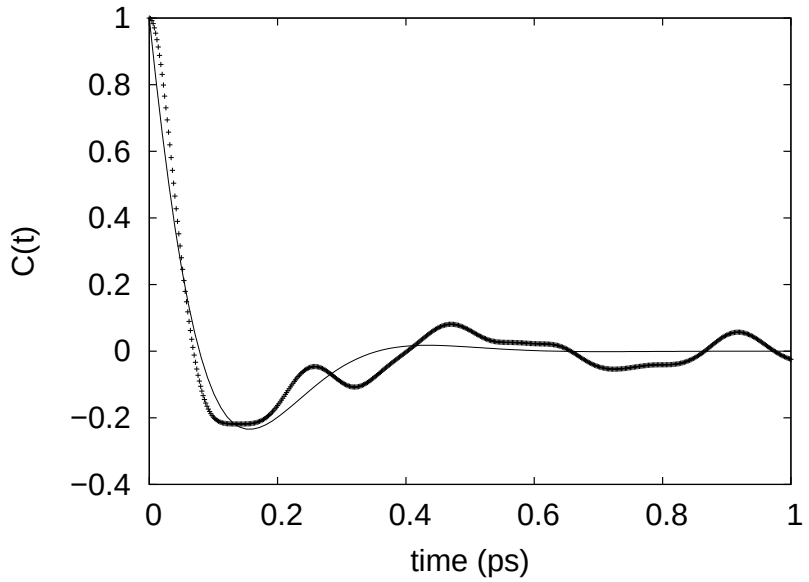

Figure 6.1.: Velocity autocorrelation function $C_v(t)$ from simulation SMD1 (cross). The solid line is the least squares fit of Eq. (6.18) which gives $\gamma = 500$ pN·ps/Å.

so that the frictional contribution is discounted from the applied forces on reconstructing the potential of mean force along the reaction pathway [95]. The friction coefficient γ can be obtained by the velocity autocorrelation analysis.

Equation (6.14) is applied to the estimation of the unbinding energy in the following SMD simulations. Higher order correction of reconstructing the potential of mean force or data analyzing from multi SMD trajectories can be found in references [96, 97].

6.2. The velocity autocorrelation function

To evaluate the potential of mean force by employing Eq. (6.14), one needs to know the friction coefficient γ. The friction coefficient can be determined by the velocity autocorrelation function $C_v(t)$

$$C_v(t) = \frac{\langle [v(t'+t) - \langle v \rangle][v(t') - \langle v \rangle] \rangle}{\langle [v(t') - \langle v \rangle]^2 \rangle}. \tag{6.15}$$

The above equation is in the normalized form.

Since our system is in the strong friction regime, we assume that the potential $U(x)$ makes a negligible contribution to the velocity autocorrelation function. In our simulations, the force term in Eq. (6.2) is

$$F(x,t) = k_0(vt - x). \tag{6.16}$$

Then Eq. (6.2) can be written as

$$m\ddot{y} + \gamma\dot{y} + k_0 y = \sigma\xi(t), \tag{6.17}$$

where y is defined by $y \equiv x - vt + \gamma v/k_0$ [96].

Eq. 6.17 is in the same form as the Langevin equation describing the Brownian motion in a harmonic potential. According to [98], the velocity autocorrelation function of such a system is

$$C_v(t) = e^{-\gamma t/2m}[\cos\frac{\omega t}{2} - \frac{\gamma}{m\omega}\sin\frac{\omega t}{2}], \tag{6.18}$$

where

$$\omega \equiv [\frac{4k_0}{m} - (\frac{\gamma}{m})^2]^{1/2}. \tag{6.19}$$

Fig. 6.1 shows the velocity autocorrelation function $C_v(t)$ and the nonlinear least-squares fit using Eq. (6.18). The correlation function was determined by averaging over a 100-ps trajectory from simulation SMD1. The figure shows that the relaxation time of the system is shorter than 0.4 ps. The friction coefficient γ determined from the fitting is equal to 442 pN·ps/Å.

6.3. Energetics of ion permeation through the selectivity filter

As described in section 6.1, the potential of mean force (PMF) along the permeation pathway in the KcsA channel can be calculated from the steered MD simulation data by employing stochastic models. According to Eq. (6.13) and Eq. (6.14), the PMF can be calculated by the following formulas:

$$(\frac{dU}{dx})_{x=vt} = \bar{F}(t) - \gamma v = \frac{dt}{\Delta t}\sum_{j=0}^{\Delta t/dt} F(jdt) - \gamma v, \tag{6.20}$$

$$\bar{U}(x = vt) = \sum_{j=0}^{\Delta t/dt} (\bar{F}(jdt) - \gamma v)vdt, \tag{6.21}$$

where $F[x(t), t]$ is the force applied to the target at time t, Δt is a time period which is long compared to the relaxation time of the system, but short compared to the total unbinding time, v is the pulling velocity, and γ is the friction coefficient. $F[x(t), t]$ is the harmonic force with the pulling velocity of 0.015 Å/ps in all SMD simulations. According to the velocity autocorrelation analysis in the previous section, the friction coefficient γ is 442 pNps/Å. The relaxation time in our system is smaller than 1 ps (Fig. 6.1, and the total unbinding time is about 300 to 400 ps (for K1). We take $\Delta t = 20$ ps as the period for averaging the force.

The force exerted on ion K1 and the PMF U derived from it in single-ion SMD simulation SMD1, SMD2, and SMD3 are shown in Fig. 6.2. In SMD1 and SMD3, two peaks along the energy profile are shown. They correspond to the energy barrier between binding site S_1 and S_0, and between S_0 and the extracellular space. In SMD1 the barrier height of the first peak is about 1.61 kcal mol^{-1}, about three times of the thermal energy ($\sim$ 0.6 kcal mol^{-1} at 300 K), and the second peak is about 4.36 kcal mol^{-1}. In SMD3, the barriers height on the first and the second peaks are 3.17 kcal mol^{-1} and 4.43 kcal mol^{-1}, respectively. In SMD2, in which the concerted movement did not occur, the translocation of K1 is energetically difficult. The PMF shows a continuously increasing barrier along the pathway of K1. The barrier height is 7.6 kcal mol^{-1}, which is almost the double of the height of the energy barrier in SMD1 and SMD3. The reason is that when a K^+ translocates upward, the bindings between the K^+ and the carbonyl oxygens below it must be broken off first. If there is a water molecule at the binding site below it, then the carbonyl oxygens can easily bind to the water hydrogens instead, and hence lower the energy barrier. In SMD2, W1 remained in S_2 when K1 moved to S_0, that means no substitute to replace K1 to bind to the carbonyl oxygens of Tyr^{78} when K1 moved upward, and therefore the free energy barrier is higher. The result from our SMD simulations is comparable with the free energy obtained by using the umbrella sampling method [91]. According to S. Bernéche and B. Roux, the free energy barrier for a K^+ to move from S_1 to the extracellular space is in the range of 0–5 kcal mol^{-1}, depending on the configuration of the test, which is of the same order as our result.

In multi-ion SMD simulations, external dragging forces were applied to the three K^+ simultaneously. The electrostatic repulsion between ions in this scheme is stronger than in single-ion SMD simulations. According to the conventional view of multi-ion mechanism, the strong electrostatic repulsion is supposed to lower the energy barrier for ion translocation. The force exerted on ion K1 and the corresponding PMF in multi-ion SMD simulation SMD4, SMD5, and SMD6 are shown in Fig. 6.3. The first energy barriers for K1 in the three SMD simulations are 2.41 kcal mol^{-1}, 1.93 kcal mol^{-1}, and 1.48 kcal mol^{-1}, respectively; and the second barriers are 2.20 kcal mol^{-1}, 1.93 kcal mol^{-1}, and 5.48 kcal mol^{-1}, respectively. The first energy barriers are not evidently smaller than in single-ion SMD simulations; but the second barriers in SMD4 and SMD5 are less than the half of the same barrier in single-ion SMD simulations. In SMD6, the barrier between S_0 and the extracellular space is two to three times higher than in the other two simulations. The high energy barrier in SMD6 mainly comes from the deformation of the selectivity filter. The side chain of Asp^{80} of M4 dislocated, and thus the binding between Asp^{80} and Gly^{79}/W$_{G79}$ was broken, as mentioned in section 4.6.2. In this condition, the binding between K1 and the filter is stronger, and therefore the movement of K1 was impeded.

The PMF calculation for K1 in multi-ion SMD simulations seems to agree to the hypothesis of multi-ion mechanism. Yet, the PMF for K2 and K3 reveal more about the nature of multi-ion transportation. The PMF along the pathway of K2 and K3 in SMD4–6 are shown in Fig. 6.4. In this figure, the z coordinates of the PMF are normalized to the center of mass of the KcsA channel. The first barriers for K2 in SMD4, 5, and 6 are

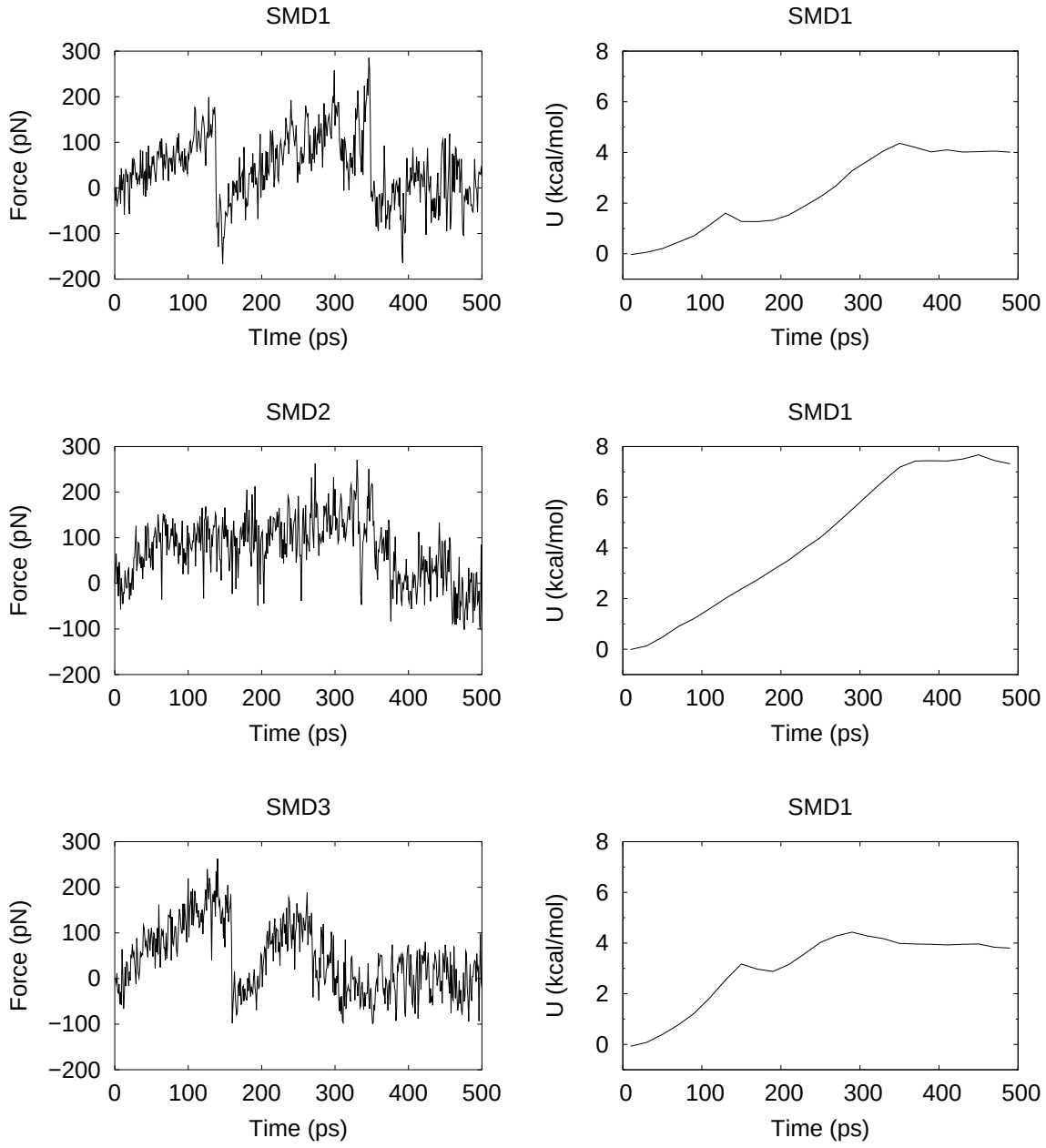

Figure 6.2.: The force exerted on K1 (left) and the derived potential of mean force (right) in the single-ion SMD simulation SMD1, SMD2, and SMD3.

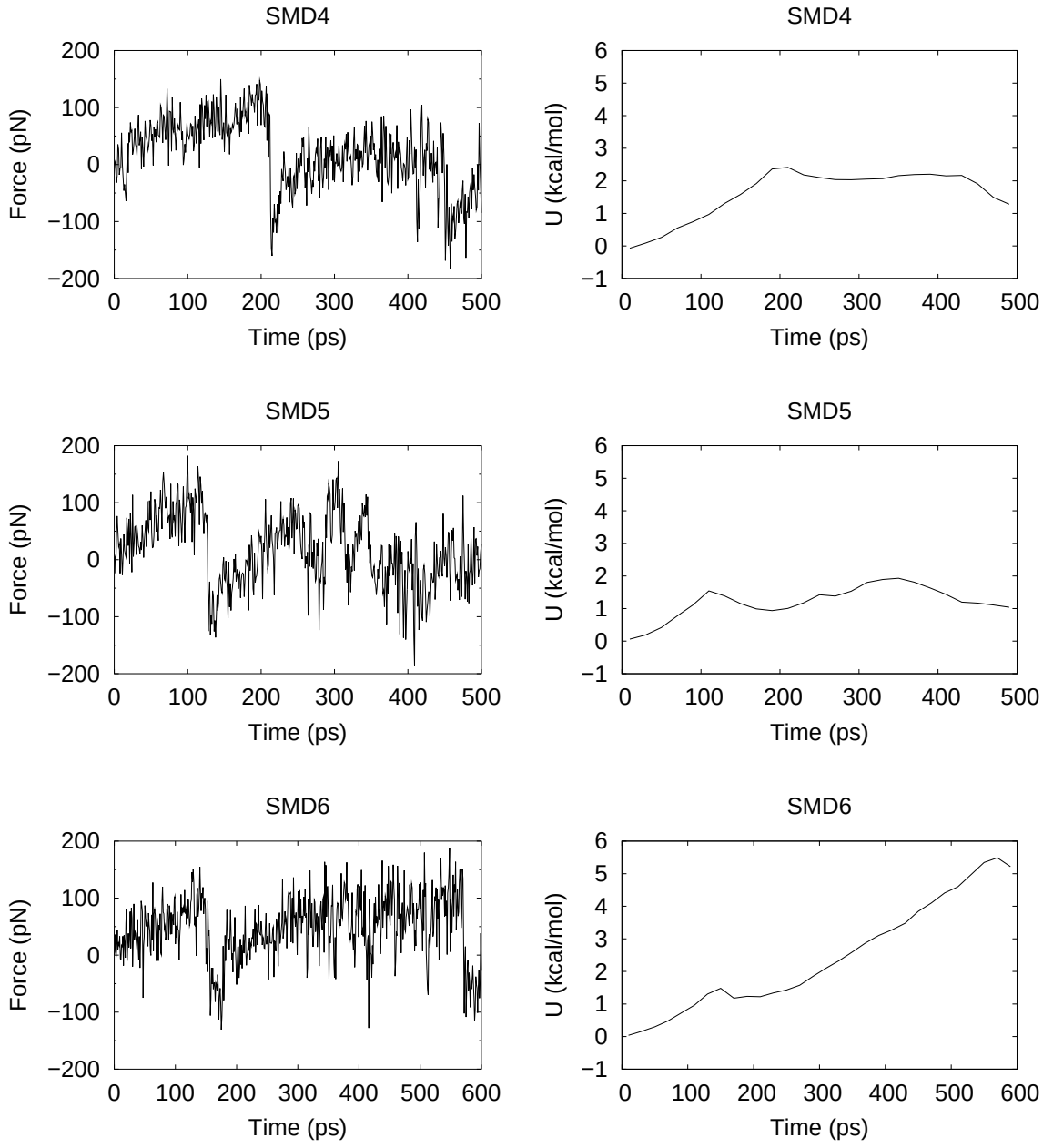

Figure 6.3.: The force exerted on K1 (left) and the reconstructed PMF (right) in multi-ion SMD simulation SMD4 (top), SMD5 (middle), and SMD6 (bottom).

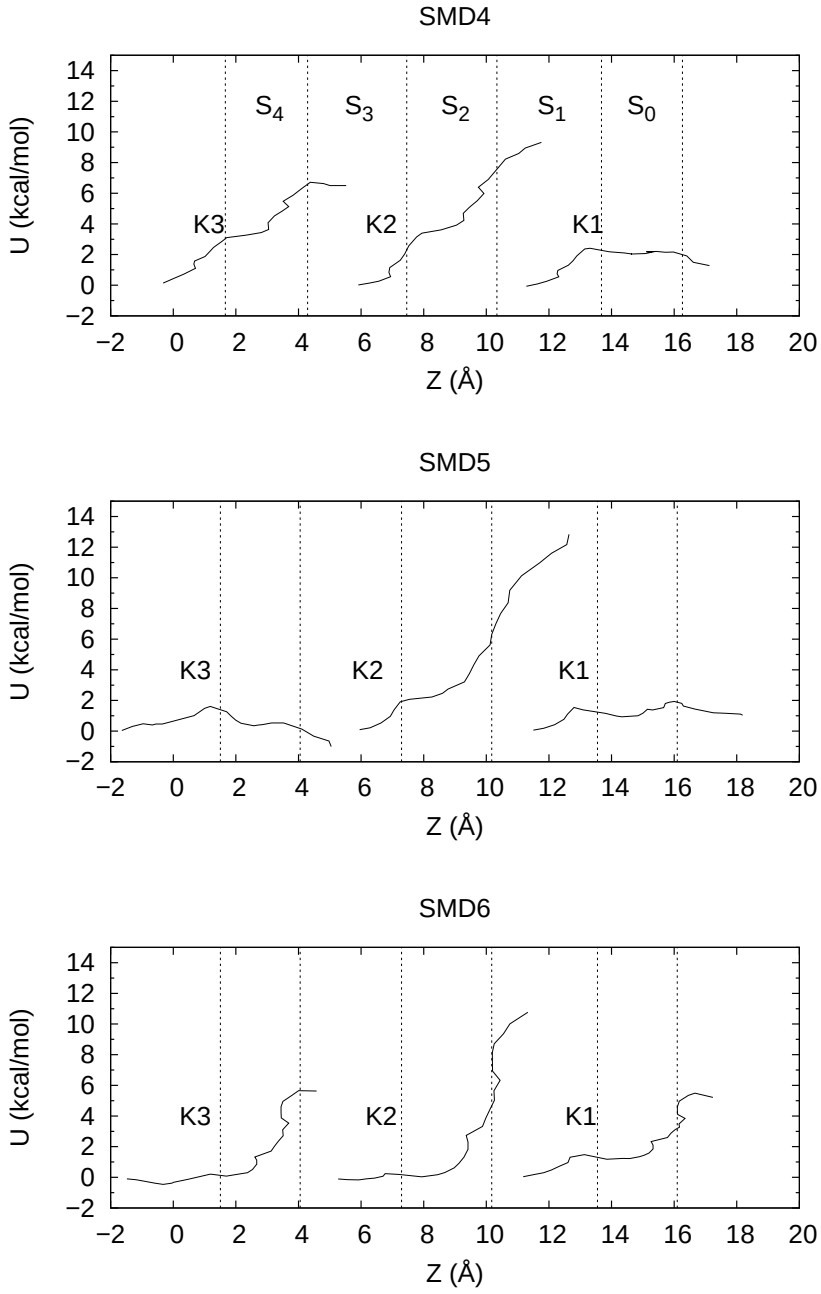

Figure 6.4.: The potential of mean force along the translocation path of the three K^+ in multi-ion SMD simulations SMD4 (top), SMD5 (middle), and SMD6 (bottom). The perpendicular dashed lines correspond to the average positions of carbonyl oxygens of the filter residue TVGYG (left to right). The positions of K^+ and carbonyl oxygens have been normalized to the center of mass of the KcsA channel.

3.15 kcal mol^{-1}, 1.91 kcal mol^{-1}, and 0.19 kcal mol^{-1}, respectively. After moving to S_2, the PMF for K2 keep increasing to over 10 kcal mol^{-1} in all three simulations. The high energy barrier came from the particular orientation of W1. After the first translocation, W1 oriented upward, i.e., $\Omega_W \sim 1$ in all three multi-ion SMD simulations. With this orientation, W1 is repulsive to K2, but attractive to K1. The binding between W1 and K1 is very stable, as one can see from the fluctuation of Ω_W in Fig. 5.10– 5.12. Water molecules are important in the concerted transportation of ions. The tumbling motion of water can induce the carbonyl groups to change their orientation. The strong binding between W1 and K1 reduces the mobility of W1, and therefore has less perturbation on the carbonyl groups. This configuration is unfavored for the upward translocation of K2, as shown by the high energy barrier.

For K3, the first barriers in SMD4, 5, and 6 are 2.84 kcal mol^{-1}, 1.6 kcal mol^{-1}, and 0.21 kcal mol^{-1}, respectively; the second barriers are 6.72 kcal mol^{-1} in SMD4, and 5.65 kcal mol^{-1} in SMD6; in SMD5, the PMF for K3 to move from S_4 to S_3 is negative, though it had to move against the repulsion from K1 and K2. Same as K2, the height of the energy barriers is related to the orientation of water molecule (W2) between K2 and K3. In SMD4 and SMD6, W2 has a more upward orientation after the first translocation, which creates the high energy barrier for K3 to move from S_4 to S_3. The particular thing is the negative PMF that appeared in SMD5. In SMD5, when K3 entered the selectivity filter, W2 ran away from S_4 to the cavity. Therefore, the binding site between K2 and K3 is empty. Without the blockage of water, K3 can move to S_3 freely. The electrostatic repulsion from K1 and K2 doesn't seem to act on the movement of K3.

Comparing the PMF among multi-ion SMD simulations, we found the energy barriers for the first translocation of K2 and K3 in SMD6 are only about zero, which is lower than in the other two simulations. The PMF seems to be sensitive to initial distances between ions. The initial distances between K1 and K2 in SMD4–6 are 5.43 Å, 5.67 Å, and 5.94 Å, and between K2 and K3 are 6.39 Å, 7.71 Å, and 6.77 Å, respectively. The distances between K1 and K2 in SMD4 and SMD6 have a difference of 0.5 Å, which is a considerable quantity when comparing with the size of a binding site (∼3 Å). The zero translocation barriers imply that a spontaneous concerted movement of multiple ions is possible, as occurred in the single-ion SMD simulations. We suggest that the concerted transportation of multiple ions is the pathway of the lowest free energy in the configuration space. As verified by the 2-D model in Chapter 5, the interaction energy is sensitive to the variation of the interatomic distance and the relative orientation, i.e., sensitive to the configurational variations. This indicates that the concerted transportation of multiple ions must move along a very specific pathway in the configuration space. In this case, the multi-ion SMD scheme may be too harsh to generate a "real" multi-ion process.

6.4. Summary

In this chapter, we have derived the potential of mean force along the permeation pathway of ions in all single-ion and multi-ion SMD simulations. The results show that the second translocation energy barriers for K2 and K3 in most multi-ion SMD simulations are very high. The high energy barriers mainly come from the water molecules sitting between ions. Water molecules are important in the concerted transportation of ions. The water molecules between K1 and K2, and between K2 and K3 oriented upward (i.e., $\Omega_W > 0$) after the first translocation. The water molecule with upward orientation is repulsive to the ion below, but attractive to the ion above. With such orientation, the water can bind to the ion above stably. The strong binding between the water and the ion reduces the mobility of the water, and hence the water molecule generates less perturbation to the surrounding carbonyl groups. This configuration is unfavored for the upward movement of the ion below. Therefore the PMF for upward translocation is high.

Comparing the results of single-ion and multi-ion SMD simulations, the approaching of K2 and K3 reduced the translocation energy barrier for K1, as suggested in the multi-ion mechanism. To accomplish the effective multi-ion transportation, the first thing is to 'have' a multiply occupied state in the selectivity filter. Till now most free energy studies of the multi-ion mechanism carried out on pre-defined multi-ion states [89, 91]. Same as in our multi-ion SMD simulations, the multi-ion occupancy state is manipulated. The high energy barriers along the permeation pathway of K2 and K3 indicate that to generate a multi-ion state in the selectivity filter is not a straightforward task. The fact that the multi-ion transportation is dominated by the polar interactions implies that it is sensitive to subtle configurational variations, like the interatomic distances and the relative orientation. This implies that a multi-ion transportation moves along a very specific pathway in the configuration space. To generate a more realistic, "dynamical" multi-ion movement in simulations, we need better manipulation scheme and some modification of the simulation system, like employing the open conformation of a channel and simulate the system in a high salt concentration environment.

7. Summary

Multi-ion permeation is a general feature in the permeation process of potassium channels. In this study, the molecular mechanism of the multi-ion conduction is elucidated. We found that K^+ and water molecules move concertedly while permeating through the selectivity filter of the channel. This concerted movement is mediated by the carbonyl groups of the backbone of residues lining the selectivity filter. The accomplishment of this mechanism relies on the particular feature of the polar interaction. The backbone carbonyl group is a polar group, as well as the water molecule. A polar group creates a kind of bistable potential when there is a ion nearby. The ion can sit stably in one of the potential wells. By changing the relative orientation of the polar group, the shape of the bistable potential can be changed easily: one potential well becomes deeper and another one shallower; at certain point, the barrier between the two potential wells vanishes completely, which turns the bistable potential unistable. By this means, the ions sitting in one of the potential wells can easily move to another one by a minor perturbation. With the proper arrangement, a sequence of ions lining in the channel pore can move from one binding site to another simultaneously, like they move in an integral, such as the concerted movement occurred in the single-ion SMD simulations shown in Chapter 5.

The proper arrangement includes: first, the positioning of the carbonyl groups. Both the space between neighboring carbonyl groups and the distance between carbonyl groups from the opposite monomers are crucial. Second, the occupancy state in the selectivity filter must be an alternative sequence of K^+ and waters, i.e. a K-W-K-W or a W-K-W-K sequence. Only then the interaction between carbonyl groups, K^+, and water molecules will fall in the same range and therefore can replace each other easily, which makes the occurrence of the spontaneous concerted movement possible. The structure of the selectivity filter itself offers the basis for the concerted movement of K^+ and water molecules. In other words, the structure of the ion channel defines its function.

The potential of mean force calculation shows that the approaching of K2 and K3 reduced the translocation energy barrier for K1, i.e. the multi-ion transportation is energetically more favored. To carry out the effective multi-ion transportation in potassium channels, the selectivity filter must be occupied by multiple ions. However, the high energy barriers along the permeation pathway of K2 and K3 indicate that to have a multiply occupied state in the selectivity filter is not as straightforward as we expected with our present system. The fact that the multi-ion transportation is dominated by the polar interactions implies that it is sensitive to subtle configurational variations, like the interatomic distances and the relative orientation. This implies that a multi-ion transportation moves along a very specific pathway in the configuration space. To gen-

erate energywise more realistic multiple ion transportation, the model system must be improved, e.g. to simulate the system with a opened channel or in a high salt concentration environment.

Finally, as described above, the structure of the selectivity filter is important to the function of potassium channels. Despite the arrangement of the sequence of the channel protein, the occupancy state in the selectivity filter also affects the stability of the filter structure. As shown in one of the single-ion SMD simulations, the movement of the water molecule in the selectivity filter induces the twist of the backbone of the filter, which turns the selectivity filter to a dysfunctional state, same as the crystallographic structure of the KcsA channel in low salt concentration. We can say that the functioning of the channel sustains the protein structure as well.

A. pK_A values of ionizible amino residues

Some amino acids have ionizable side-chains. That means when they are solvated in solvent, their side-chains can be in different charged states. The pK_A value of an amino residue is a measure of its probability of being in a charged state under certain conditions. It depends on several parameters from the environment like temperature, pH value, microenvironment around the solute, etc.

The ionization equilibrium of a weak acid is given by

$$HA \rightleftharpoons H^+ + A^- \tag{A.1}$$

The equilibrium constant K of this ionization is

$$K = \frac{[H^+][A^-]}{[HA]} \tag{A.2}$$

The pK value of an acid is defined as

$$pK = -logK = log\frac{1}{K} \tag{A.3}$$

And we already know the definition of pH value of a solution is

$$pH = log_{10}\frac{1}{[H^+]} = -log_{10}[H^+] \tag{A.4}$$

One can derive the relationship between pH and pK values from equation (A.2)

$$\frac{1}{[H^+]} = \frac{1}{K}\frac{[A^-]}{[HA]} \tag{A.5}$$

Take logarithm of both sides of equation (A.5)

$$log\frac{1}{[H^+]} = log\frac{1}{K} + log\frac{[A^-]}{[HA]} \tag{A.6}$$

substitute log $1/[H^+]$ to pH and log $1/K$ to pK in equation (A.6) we get the so called Henderson-Hasselbach equation

$$pH = pK + log\frac{[A^-]}{[HA]} \tag{A.7}$$

Amino acid	pK_A value (25°C)
ASP	3.9
GLU	4.3
HIS	6.0
CYS	8.3
TYR	10.9
LYS	10.8
ARG	12.5

Table A.1.: pK_A value of side-chain ionizable amino acids.

The pK value can be calculated if the molar proportion of A^- to HA and the pH value of the solution are known.

Table A.1 gives the typical pK_A value of amino residues with ionizable side cahins:

In neutral pH, lysin and arginine are positively charged, and aspartic and glutamic acid are negatively charged. The pK_A value of the side chain of histidine is close to 7.0. It can be either uncharged or positively charged, depending on its local environment.

B. Orthogonal transformation used for structure comparison

Conformation comparison is an important topic on bimolecular simulation. The main subject of this calculation is to determine a proper transformation operator which generates the best superposition of the compared structures. The coordinate of a given conformation is then translated by the operator and compared to the referenced one. The criterion for the best superposition of two molecular conformations is that the sum of the squared distances between corresponding atoms is minimal. The center of mass of the structures under comparison are first moved the origin, then the rotation matrix which generated the optimal superposition of the two coordinate sets is to be found. However, the elements of the rotation matrix are not linearly independent, and some iterative optimization procedures always occur. To solve this problem, a simple and efficient algorithm using quaternion algebra has been developed by Mackay in 1984 [86] and later been further improved by Kearsley [85].

A quaternion can be considered as a row matrix of four numbers or the combination of a scalar with a 3D Cartesian vector;

$$Q = (q_1, q_2, q_3, q_4) \equiv [q_1, \mathbf{q}].$$

The product of two quaternions P and Q is also a quaternion and can be expressed by matrix multiplication or through a combination of vector product:

$$\begin{aligned} PQ &= \begin{pmatrix} p_1 & -p_2 & -p_3 & -p_4 \\ p_2 & p_1 & -p_4 & p_3 \\ p_3 & p_4 & p_1 & -p_2 \\ p_4 & -p_3 & p_2 & p_1 \end{pmatrix} \begin{pmatrix} q_1 \\ q_2 \\ q_3 \\ q_4 \end{pmatrix} \\ &\equiv [p_1 q_1 - \mathbf{p}\cdot\mathbf{q}, p_1\mathbf{q} + q_1\mathbf{p} + \mathbf{p}\wedge\mathbf{q}]. \end{aligned} \tag{B.1}$$

The norm squared of Q, $|Q|^2$, is given by $(q_1^2 + \mathbf{q}\cdot\mathbf{q})$ and the inverse by $[q_1, -\mathbf{q}]/|Q|^2$. The norm of the product of two quaternions is equal to the product of their individual norms, $|PQ| = |P||Q|$. A unit quaternion $\hat{Q}$ can be used as a rotation operator to translate $\mathbf{x}$ to a new position $\mathbf{x}^{\mathbf{R}}$ as follows:

$$\begin{aligned} [0, \mathbf{x}^{\mathbf{R}}] &= \hat{Q}^{-1}[0, \mathbf{x}]\hat{Q} \\ &= [0, q_1^2\mathbf{x} + (\mathbf{x}\cdot\mathbf{q})\mathbf{q} + 2q_1(\mathbf{x}\wedge\mathbf{q})]. \end{aligned} \tag{B.2}$$

$$\begin{aligned}\mathbf{x^R} &= \mathbf{Rx} \\ &= \begin{pmatrix} q_1^2+q_2^2-q_3^2-q_4^2 & 2(q_2q_3+q_1q_4) & 2(q_2q_4-q_1q_3) \\ 2(q_2q_3-q_1q_4) & q_1^2+q_3^2-q_2^2-q_4^2 & 2(q_3q_4+q_1q_2) \\ 2(q_2q_4+q_1q_3) & 2(q_3q_4-q_1q_2) & q_1^2+q_4^2-q_2^2-q_3^2 \end{pmatrix} \begin{pmatrix} x \\ y \\ z \end{pmatrix},\end{aligned} \tag{B.3}$$

where vectors are treated as quaternions with zero scalar component.

Either $\hat{Q}$ or R can be used for rotation. An advantage of using quaternion formulation is that improper rotation is prevented, since the determinant of R, which reduced to $(q_1^2+q_2^2+q_3^2+q_4^2)^3$, is always greater than zero.

However, without appropriate weighting scheme, applying a unit quaternion $\hat{Q}$ doesn't minimize the sum of the squared distances between atoms, but rather the sum of angles between tow coordinate sets. Therefore, instead of using a unit quaternion, a general quaternion Q is used in Kearsley's method. The difference between two comparing structures after applying the transformation is defined as the residual quaternion $[0, \mathbf{e}]$, where

$$[0, \mathbf{e}] = [0, \mathbf{x}^{'}] - Q^{-1}[0, \mathbf{x}]Q. \tag{B.4}$$

Q is determined by using corresponding atomic position vectors and minimizing the sum of the squared magnitudes of the residual vectors $\sum |\mathbf{e}|^2 = \sum |[0, \mathbf{e}]|^2$. To solve the problem algebraically, first multiply through by Q,

$$Q[0, \mathbf{e}] = Q[0, \mathbf{x}^{'}] - QQ^{-1}[0, \mathbf{x}]Q = Q[0, \mathbf{x}^{'}] - [0, \mathbf{x}]Q. \tag{B.5}$$

then construct a least-squares residual function ε.

$$\begin{aligned}\varepsilon &= \sum |Q[0, \mathbf{e}]|^2 = \sum |Q|^2|\mathbf{e}|^2 = |Q|^2 \sum |\mathbf{e}|^2 \\ &= \sum |-\mathbf{q} \cdot (\mathbf{x}^{'} - \mathbf{x}), q_1(\mathbf{x}^{'} - \mathbf{x}) + \mathbf{q} \wedge (\mathbf{x}^{'} + \mathbf{x})]|^2.\end{aligned} \tag{B.6}$$

To prevent the transformed structure from expanding, the norm of Q is now constrained to unity using the Lagrange multiplier procedure. The method is used to determine the best plane through a set of points in the space. The residual function ε expressed in terms of the quaternion components is given by

$$\begin{aligned}\varepsilon &= \sum \{[q_2(x^{'} - x) + q_3(y^{'} - y) + q_4(z^{'} - z)]^2 \\ &\quad +[q_1(x^{'} - x) + q_3(z^{'} + z) - q_4(y^{'} + y)]^2 \\ &\quad +[q_1(y^{'} - y) + q_4(x^{'} + x) - q_2(z^{'} + z)]^2 \\ &\quad +[q_1(z^{'} - z) + q_2(y^{'} + y) - q_3(x^{'} + x)]^2\} \\ &\quad +\lambda(1 - q_1^2 - q_2^2 - q_3^2 - q_4^2).\end{aligned} \tag{B.7}$$

where λ is the Lagrange multiplier. The non-linear aspect of the least-squares refinement has been moved to the λ multiplier. Differentiating ε with respect to each Q component

and setting to zero, we find that the resulting equations can be organized as an eigenvalue problem where $x_m = (x^{'} - x)$, $x_p = (x^{'} + x)$ with similar definition for y_m, y_p, z_m and z_p.

$$\begin{pmatrix} \sum(x_m^2 + y_m^2 + z_m^2) & \sum(y_p z_m - y_m z_p) & \sum(x_m z_p - x_p z_m) \\ \sum(y_p z_m - y_m z_p) & \sum(y_p^2 + z_p^2 + x_m^2) & \sum(x_m y_m - x_p y_p) \\ \sum(x_m z_p - x_p z_m) & \sum(x_m y_m - x_p y_p) & \sum(x_p^2 + z_p^2 + y_m^2) \\ \sum(x_p y_m - x_m y_p) & \sum(x_m z_m - x_p z_p) & \sum(y_m z_m - y_p z_p) \end{pmatrix}$$
$$\begin{pmatrix} \sum(x_p y_m - x_m y_p) \\ \sum(x_m z_m - x_p z_p) \\ \sum(y_m z_m - y_p z_p) \\ \sum(x_p^2 + y_p^2 + z_m^2) \end{pmatrix} \begin{pmatrix} q_1 \\ q_2 \\ q_3 \\ q_4 \end{pmatrix} = \lambda \begin{pmatrix} q_1 \\ q_2 \\ q_3 \\ q_4 \end{pmatrix}. \tag{B.8}$$

Diagonalizing this symmetric matrix will give four orthogonal unit quaternions. The eigenvalues is the value of the residual when applying the corresponding eigenvector to transform the coordinate sets. The root-mean-squares deviation is given by

$$rmsd = (\lambda/n)^{1/2}, \tag{B.9}$$

where n is the number of atoms compared. The smallest eigenvalue gives the r.m.s.d. of the optimal superposition of the compared structures.

Bibliography

[1] H. H. Ussing. The distinction by means of tracers between active transport and diffusion. *Acta Physiol. Scandinavica*, **19**:43–56, 1949.

[2] A. L. Hodgkin and R. D. Keynes. The potassium permeability of a giant nerve fibre. *J. Physiol.*, **128**:61–88, 1955.

[3] D. A. Doyle, J. M. Cabral, R. A. Pfuetzner, A. Kuo, J. M. Gulbis, S. L. Cohen, B. T. Chait, and R. MacKinnon. The structure of the potassium channel: molecular basis of K^+ conduction and selectivity. *Nature*, **280**:69–77, 1998.

[4] Y. Zhou, J. H. Morais-Cabral, A. Kaufman, and R. MacKinnon. Chemistry of ion coordination and hydration revealed by a K^+ channel-Fab complex at 2.0 Å resolution. *Nature*, **414**:43–48, 2001.

[5] C. L. Brooks, M. Karplus, and B. M. Pettitt. *Proteins: A theoretical perspective of dynamics, structure and thermodynamics.* John Wiley & Sons, New York, 1988.

[6] M. Karplus, G. A. Petsko. Molecular dynamics simulations in biology. *Nature*, **347**:631–639, 1990.

[7] M. Karplus and J. A. McCammon. Molecular dynamics simulations of biomolecules. *Nature Struct. Biol.*, **9**:646–652, 2002.

[8] E. Tajkhorshid, A. Aksimentiev, I. Balabin, M. Gao, B. Isralewitz, J. C. Phillips, F. Zhu, and K. Schulten. Large scale simulation of protein mechanics and function. *Advances in Protein Chemistry*, edited by F. M. Richards, D. S. Eisenberg, and J. Kuriyan,**vol. 66**: 195–247, Elsevier Academic Press, New York, 2003.

[9] S. W. Chiu, S. Subramanian, and E. Jakobsson. Simulation study of a gramicidin/lipid bilayer system in excess water and lipid. I. Structure of the molecular complex. *Biophys. J.*, **76**:1929–1938, 1999.

[10] S. W. Chiu, S. Subramanian, and E. Jakobsson. Simulation study of a gramicidin/lipid bilayer system in excess water and lipid. II. Rates and mechanisms of water transport. *Biophys. J.*, **76**:1939–1950, 1999.

[11] R. Pomes and B. Roux. Molecular mechanism of H^+ conduction in the single-file water chain of the gramicidin channel. *Biophys. J.*, **82**:2304–2316, 2002.

[12] D. P. Tieleman and H. J. C. Berendsen. A molecular dynamics study of the pores formed by Escherichia coli OmpF porin in a fully hydrated palmitoyloleoylphosphatidylcholine bilayer. *Biophys. J.*, **74**:2786–2801, 1998.

[13] W. Im and B. Roux. Ions and counterions in a biological channel: a molecular dynamics simulation of OmpF porin from Escherichia coli in an explicit membrane with 1 M KCl aqueous salt solution. *J. Mol. Biol.*, **319**:1177–1197, 2002.

[14] S. Bernéche and B. Roux. Molecular dynamics of the KcsA K^+ channel in a bilayer membrane. *Biophys. J.*, **78**:2900–2917, 2000.

[15] I. H. Shrivastava and M. S. Sansom. Simulations of ion permeation through a potassium channel: molecular dynamics of KcsA in a phospholipid bilayer. *Biophys. J.*, **78**:557–570, 2000.

[16] T. W. Allen, S. Kuyucak, and S. -H. Chung. Molecular dynamics study of the KcsA potassium channel. *Biophys. J.*, **77**:2502–2516, 1999.

[17] H. Schrempf, O. Schmidt, R. Kummerlein, S. Hinnah, D. Muller, M. Betzler, T. Steinkamp, and R. Wagner. A prokaryotic potassiumion channel with 2 predicted transmembrane segments from *Streptomyces lividans*˙ *EMBO J.*, **14**:5170–5178, 1995.

[18] D. M. Cortes and E. Perozo. Structural dynamics of the *S*treptomyces lividans K^+ channel (SKC1): oligomeric stoichiometry and stability. *Biochemistry*, **36**:10343–10352, 1997.

[19] L. Heginbotham, E. Odessey, and C. Miller. Tetrameric stoichiometry of a prokaryotic K^+ channel. *Biochemistry*, **36**:10335–10342, 1997.

[20] B. Hille. *Ion Channels of Excitable Membranes.* Sinauer Associates, Inc., 2001.

[21] M. LeMasurier, L. Heginbotham, and C. Miller. KcsA: It's a potassium channel. *J. Gen. Physiol.*, **118**:303–313, 2001.

[22] L. Heginbotham, M. LeMasurier, L. Kolmakova-Partensky, and C. Miller. Single streptomyces lividans K^+ channels: functional asymmetries and sidedness of proton activation. *J. Gen. Physiol.*, **114**:551–560, 1999.

[23] G. Yellen. Ionic permeation and blockade in Ca^{2+}-activated K^+ channels of bovine chromaffin cells. *J. Gen. Physiol.*, **84**:157–186, 1984.

[24] L. Heginbotham, T. Abramson, and R. MacKinnon. A functional connection between the pores of distantly related ion channels as revealed by mutant K^+ channels. *Science*, **258**:1152–1155, 1992.

[25] L. Heginbotham, Z. Lu, T. Abramson, and R. MacKinnon. Mutations in the K+ channel signature sequence. *Biophys. J.*, **66**:1061–1067, 1994.

[26] F. Bezanilla and C. M. Armstrong. Negative conductance caused by entry of sodium and cesium ions into the potassium channels of squid axons. *J. Gen. Physiol.*, **60**:588–608, 1972.

[27] R. J. French and J. B. Wells. Sodium ions as blocking agents and charge carriers in the potassium channel of the squid giant axon. *J. Gen. Physiol.*, **70**:707–724, 1977.

[28] C. M. Nimigean and C. Miller. Na^+ block and permeation in a K^+ channel of known structure. *J. Gen. Physiol.*, **120**:323–335, 2002.

[29] D. Meuser, H. Splitt, R. Wagner, and H. Schrempf. Exploring the open pore of the potassium channel from *Streptomyces lividans*˙ *FEBS Letters*, **462**:447–452, 1999.

[30] B. Roux and R. MacKinnon. The cavity and pore helices in the KcsA K^+ channel: electrostatic stabilization of monovalent cations. *Science*, **285**:100–102, 1999.

[31] B. Roux, S. Bernéche, and W. Im. Ion channels, permeation, and electrostatics: insight into the function of KcsA. *Biochemistry*, **39**:13295–13306, 2000.

[32] I. M. Williamson, S. J. Alvis, J. M. East, and A. G. Lee. Interactions of phospholipids with the potassium channel KcsA. *Biophys. J.*, **83**:2026–2038, 2002.

[33] D M. Cortes, L. G. Cuello and E. Perozo. Molecular architecture of full-length *K*csA: role of cytoplasmic domains in ion permeation and activation gating. *J. Gen. Physiol.*, **117**:165–180, 2001.

[34] Y. Jiang, A. Lee, J. Chen, M. Cadene, B. T. Chait, and R. MacKinnon. Crystal structure and mechanism of a calcium-gated potassium channel. *Nature*, **417**:515–522, 2002.

[35] L. G. Cuello, J. G. Romero, D M. Cortes and E. Perozo. pH-dependent gating in the *S*treptomyces lividans K^+ channel. *Biochemistry*, **37**:3229–3236, 1998.

[36] E. Perozo, D M. Cortes and L. G. Cuello. Three dimensional architecture and gating mechanism of a K^+ channel studied by EPR spectroscopy. *Nat. Struct. Biol.*, **5**:459–469, 1998.

[37] Y. Jiang, A. Lee, J. Chen, M. Cadene, and R. MacKinnon. The open pore conformation of potassium channels. *Nature*, **417**:523–526, 2002.

[38] M. Karplus and G. A. Petsko. Molecular dynamics simulations in biology. *Nature*, **347**: 631–639, 1990.

[39] J. A. McCammon, B. R. Gelin, M. Karplus. Dynamics of folded proteins. *Nature*, **267**:585–590, 1977.

[40] S. Izrailev, S. Stepaniants, B. Isralewitz, D. Kosztin, H. Lu, F. Molnar, W. Wriggers, and K. Schulten. Steered molecular dynamics, in *Computational molecular dynamics: challenges, methods, ideas*, edited by P. Deuflhard, J. Hermans, B. Leimkuhler, A. E. Mark, S. Reich, and R. D. Skeel, Lecture Notes in Computational Science and Engineering, 39–65. Springer-Verlag, Berlin, 1998.

[41] H. J. C. Berendsen. Molecular dynamics simulations: the limits and beyond. *Computational molecular dynamics: challenges, methods, ideas*, edited by P. Deuflhard, J. Hermans, B. Leimkuhler, A. E. Mark, S. Reich, and R. D. Skeel, Lecture Notes in Computational Science and Engineering, 3–36. Springer-Verlag, Berlin, 1998.

[42] C. A. Case, D. A. Pearlman, J. W. Cadwell, T. E. Cheatham III, W. S. Ross, C. L. Simmerling, T. A. Darden, K. M. Merz, R. V. Stanton, A. L. Cheng, J .J. Vincent, M. Crowley, D. M. Ferguson, R. J. Radmer, G. L. Seibel, U. C. Singh, and P. A. Kollman. AMBER 5. University of California, San Francisco, 1997.

[43] M. P. Allen and D. J. Tildesley. *Computer Simulation of Liquids.* Oxford University Press, New York, 1987.

[44] L. Verlet. Computer 'experiments' on classical fluids. I. Thermodynamical properties of Lennard-Jones molecules. *Phys. Rev.*, **159**:98–103, 1967.

[45] R. W. Hockney. The potential calculation and some applications. *Methods comput. Phys.*, **9**:136–211, 1970.

[46] W. C. Swope, H. C. Andersen, P. H. Berens, and K. R. Wilson. A computer simulation method for the calculation of equilibrium constants for the formation of physical clusters of molecules: application to small water clusters. *J. Chem. Phys.*, **76**:637–649, 1982.

[47] J. M. Thijssen. *Computational Physics.* Cambridge University Press, 1999.

[48] J. Ryckaert, G. Ciccotti, and H. J. C. Berendsen. Numerical integration of the cartesian equations of motion of a system with constraints: molecular dynamics of n-alkanes. *J. Comp. Phys.*, **23**:327–341, 1977.

[49] W. F. van Gunsteren and H. J. C. Berendsen. Algorithms for macromolecular dynamics and constraint dynamics. *Mol. Phys.*, **34**:1311–1327, 1977.

[50] W. F. van Gunsteren and M. Karplus. Effect of constraints on the dynamics of macromolecules. *Macromolecules*, **15**:1528–1544, 1982.

[51] H. C. Andersen. Molecular dynamics simulations at constant pressure and/or temperature. *J. Chem. Phys.*, **72**:2384–2393, 1980.

[52] H. J. C. Berendsen, J. P. M. Postma, W. F. van Gunsteren, A. DiNola, and J. R. Haak. Molecular dynamics with coupling to an external bath. *J. Chem. Phys.*, **81**:3684–3690, 1984.

[53] T. Morishita, Fluctuation formulas in molecular-dynamics simulations with the weak coupling heat bath. *J. Chem. Phys.*, **113**:2976–2982, 2000.

[54] S. Nosé. A molecular dynamics method for simulationsin the canonical ensemble. *Mol. Phys.*, **52**:255–268, 1984.

[55] W. G. Hoover. Canonical dynamics: equilibrium phase-space distributions. *Phys. Rev.*, **A31**:1695–1697, 1985.

[56] S. Feller, Y. Zhang, R. W. Pastor, and B. R. Brooks. Constant pressure molecular dynamics simulation: the Langevin piston method. *J. Chem. Phys.*, **103**:4613–4621, 1995.

[57] P. Ewald. Die Berechnung optischer und elektrostatischer Gitterpotentiale. *Ann. Phys.*, **64**: 253–287, 1921.

[58] S. W. de Leeuw, J. W. Perram and E. R. Smith. Simulation of electrostatic systems in periodic boundary conditions. I. Lattice sums and dielectric constants. *Proc. R. Soc. Lond.*, **A373**:27–56, 1980.

[59] R. W. Hockney and J. W. Eastwood. *Computer Simulation Using Particles.* Institute of Physics Publishing, Bristol, 2nd ed., 1988.

[60] S. J. Weiner, P. A. Kollman, D. A. Case, U. C. Singh, C. Ghio, G. Alagona, S. Profeta, and P. Weiner. A new force field for molecular mechanical simulation of nucleic acids and proteins. *J. Am. Chem. Soc.*, **106**:765–784, 1984.

[61] S. J. Weiner, P. A. Kollman, D. T. Nguyen, and D. A. Case. An all atom force filed for simulations of proteins and nucleic acids. *J. Comp. Chem.*, **7**:230–252, 1986.

[62] W. D. Cornell, P. Cieplak, C. I. Bayley, I. R. Gould, K. M. Merz, D. M. Ferguson, D. C. Spellmeyer, T. Fox, J. W. Cadwell, and P. A. Kollman. A second generation force field for the simulation of proteins, nucleic acids, and organic molecules. *J. Am. Chem. Soc.*, **117**:5179–5197, 1995.

[63] W. D. Cornell, P. Cieplak, C. I. Bayley, and P. A. Kollman. Application of RESP charges to calculate conformational energies, hydrogen bond energies, and free energies of solvation. *J. Am. Chem. Soc.*, **115**:9620–9631, 1993.

[64] W. L. Jorgensen, J. Chandrasekhar, J. D. Madura, R. W. Impey, and M. L. Klein. Comparison of simple potential functions for simulating liquid water. *J. Chem. Phys.*, **79**:926–935, 1983.

[65] C. I. Bayly, P. Cieplak, W. D. Cornell, and P. A. Kollman. A well-behaved electrostatic potential based method using charge restraints for deriving atomic charges: the RESP model. *J. Phys. Chem.*, **97**:10269–10280, 1993.

[66] E. L. Florin, V. T. Moy, and H. E. Gaub. Adhesion force between individual ligand-receptor pairs. *Science*, **264**:415–417, 1994.

[67] A. Chilcotti and P. S. Stayton. Molecular origins of the slow streptavidin-biotin dissociation kinetics. *J. Am. Chem. Soc.*, **117**:10622–10628, 1995.

[68] H. Grubmüller, B. Heymann, and P. Tavan. Ligand binding: molecular mechanics calculation of the streptavidin-biotin rupture force. *Science*, **271**:997–999, 1996.

[69] B. Isralewitz, S. Izrailev, and K. Schulten. Binding pathway of retinal to bacterioopsin: A prediction by molecular dynamics simulations. *Biophys. J.*, **73**:2972–2979, 1997.

[70] S. Stepaniants, S. Izrailev, and K. Schulten. Extraction of lipids from phospholipid membranes by steered molecular dynamics. *J. Mol. Model.*, **3**:473–475, 1997.

[71] S.-J. Marrink, O. Berger, P. Tieleman, and F. Jähnig. Adhesion forces of lipids in a phospholipid membrane studied by molecular dynamics simulations. *Biophys. J.*, **74**:931–943, 1998.

[72] S. Izrailev, S. Stepaniants, M. Balsera, Y. Oono, and K. Schulten. Molecular dynamics study of unbinding of the avidin-biotin complex. *Biophys. J.*, **72**:1568–1581, 1997.

[73] S. K. Lüdemann, O. Carugo, and R. C. Wade. Substrate access to cytochrome P450cam: A comparison of a thermal motion pathway analysis with molecular dynamics simulation data. *J. Mol. Model.*, **3**:369–374, 1997.

[74] J. L. Sussman, D. Lin, J. Jiang, N. O. Manning, J. Prilusky, O. Ritter, and E. E. Abola. Protein Data Bank (PDB): database of three-dimensional structural information of biological macromolecules. *Acta Crystallogr. D Biol. Crystallogr.*, **54**:1078–1084, 1998.

[75] C. E. A. F. Schafmeister, W. S. Ross, and V. Romanvoski. LEaP. University of California, San Francisco, 1995.

[76] H. Heller, M. Schaefer, and K. Schulten. Molecular dynamics simulation of a bilayer of 200 lipids in the gel and in the liquid crystal phases. *J. Phys. Chem.*, **97**:8343–8360, 1993.

[77] J.-H. Lin. Structures, dynamics, and energetics of protein membrane interactions: Molecular dynamics studies. *Doctoral Dissertation*, IFF, Forschungszentrum Jülich, Germany, 2000.

[78] L. Stryer. *Biochemistry.* W. H. Freeman and Company, New York, 1995.

[79] V. B. Luzhkov and J. Åqvist. A computational study of ion binding and protonation states in the KcsA potassium channel. *Biochim. Biophys. Acta*, **1481**:360–370, 2000.

[80] K. M. Ranatunga, I. H. Shrivastava, G. R. Smith, and M. S. P. Sansom. Side-chain ionization states in a potassium channel. *Biophys. J.*, **80**:1210–1219, 2001.

[81] S. Bernéche and B. Roux. The ionization state and the conformation of Glu-71 in the KcsA K(+) channel. *Biophys. J.*, **82**:772–780, 2002.

[82] S. C. Harvey, R. K.-Z. Tan, and T. E. Cheatham III. The flying ice cube: velocity rescaling in molecular dynamics leads to violation of energy equipartition. *J. Comp. Chem.*, **19**:726–740, 1998.

[83] T. Darden, D. York, and L. Pederson. Particle mesh Ewald: An $N{\cdot}log(N)$ method for Ewald sums in large systems. *J. Chem. Phys.*, **98**:10089–10092, 1993.

[84] U. Essmann, L. Perera, M. L. Berkowitz, T. Darden, H. Lee, and L. G. Pederson. A smooth particle mesh Ewald method. *J. Chem. Phys.*, **103**:8577–8593, 1995.

[85] K. Kearsley. On the orthogonal transformation used for structural comparisons. *Acta Cryst.*, **A45**:208–210, 1989.

[86] A. L. Mackay. Quaternion transformation of molecular orientation. *Acta Cryst.*, **A40**:165–166, 1984.

[87] J. H. Morais-Cabral, Y. Zhou, and R. MacKinnon. Energetic optimization of ion conduction rate by the K^+ selectivity filter. *Nature*, **414**:37–42, 2001.

[88] L. Guidoni and P. Carloni. Potassium permeation through the KcsA channel: a density functional study. *Biochim. Biophys. Acta*, **1563**:1–6, 2002.

[89] J. Åqvist and V. Luzhkov. Ion permeation mechanism of the potassium channel. *Nature*, **404**:881–884, 2000.

[90] S. Garofoli and P. C. Jordan. Modeling permeation energetics in the KcsA potassium channel. *Biophys. J.*, **84**:2814–2830, 2003.

[91] S. Bernéche and B. Roux. Energetics of ion conduction through the K^+ channel. *Nature*, **414**:73–77, 2001.

[92] C. Jarzynski. Nonequilibrium equality for free energy differences. *Phys. Rev. Lett.*, **78**:2690–2693, 1997.

[93] C. Jarzynski. Equilibrium free-energy differences from nonequilibrium measurements: A master-equation. *Phys. Rev. E*, **56**:5018–5035, 1997.

[94] E. Evans and K. Ritchie. Dynamic strength of molecular adhesion bonds. *Biophys. J.*, **72**:1541–1555, 1997.

[95] M. Balsera, S. Stepaniants, S. Izrailev, Y. Oono, and K. Schulten. Reconstructing potential energy functions from simulated force-induced unbinding processes. *Biophys. J.*, **73**:1281–1287, 1997.

[96] J. R. Gullingsrud, R. Braun, and K. Schulten. Reconstructing potential of mean force through time series analysis of steered molecular dynamics simulation. *J. Comp. Phys.*, **151**:190–211, 1999.

[97] S. Park, F. Khalili-Araghi, E. Tajkhorshid, and K. Schulten. Free energy calculation from steered molecular dynamics simulations using Jarzinski's equality. *J. Chem. Phys.*, **199**:3559–3566, 2003.

[98] H. Risken. *The Fokker-Planck Equation.* Springer-Verlag, Berlin, 1996.

List of Tables

List of Figures

Acknowledgments

I would like to thank all friends and colleagues for their generous help during my study in Germany.

First of all, I would like to thank my thesis adviser Dr. Arthur Baumgaertner for his great support of my work, and many interesting discussion and suggestions. Then I would like to thank Dr. Jung-Hsing Lin for his introduction to the molecular dynamics simulation and many helpful informations and suggestions on research work and life in Germany.

I am truly grateful to friends who generously gave their hands, especially in the first period of my staying in Germany. Many thanks to Dr. Silke Biermann for her great help, especially during the period after my little bike accident. Thanks to Mr. and Mrs. Stump for their kindly help. Thanks to Dr. Karl-Heinz Herrmann for organizing many interesting meetings and trips. Thanks to Dr. Catalina Lopez and Dr. Jesus Maytorena for their friendship and support, especially in my hard time. Thanks to Dr. Ralf Sambeth for various helps and informations. Thanks Dr. Tanja Schilling, Dr. Christof Best, Dr. Thorsten Auth, Dr. Deepak Patucha and many others for giving helps and sharing a good time with me.

Many thanks to Dr. S. V. M. Satyanarayana for proof reading of the manuscript and suggestions to my thesis, and sharing his immense wisdom of life with me. Thanks to Bidisha Nandy for proof reading and her generous help in my daily life. Thanks Matthias Haan for proof reading. Thanks Dr. Sergei Grudinin for helpful discussion and informations.

The simulation work is done on the supercomputer of ZAM in Forschungszentrum Jülich. I would like to thank Mr. Willi Homberg of ZAM for his technical support and always answering my various awkward questions with great patience.

Finally, special thanks to my dear family. I can achieve nothing without their love and support.